

Université du Québec

INRS-EMT

Solar-Driven Photoelectrochemical Hydrogen Generation
based on Colloidal Core/Shell Quantum Dots

By

Kanghong Wang

Committee

External examiner

Prof. Fabio Cicoira
Polytechnique

Prof. Jean Michel Nunzi
Queen's University

Internal examiner

Prof. Daniel Guay
INRS-EMT

Supervisor

Prof. Federico Rosei
INRS-EMT

Co-supervisor

Prof. Xuhui Sun
Soochow University

Abstract

Colloidal quantum dots (QDs) are considered as one of the promising candidates for next-generation solar-to-fuel energy conversion strategies due to many unique optical and optoelectronic properties. Comparing to directly transferring to electricity, there is an alternative to convert solar energy into hydrogen (H_2) fuels. H_2 is one of the green energy resources with high power density and the by-product is only water. Thus, colloidal QDs have been investigated a lot for photoelectrochemical (PEC) H_2 generation. However, this strategy still suffers from low solar-to-hydrogen (STH) efficiency as well as poor stability performance which restrict their wider application. In my thesis, I used colloidal QDs as the solar harvester, sensitizing TiO_2 for PEC H_2 evolution. The focus of my work is to design proper structure of core/shell QDs to enhance the absorption from solar spectrum as well as facilitating the carrier separation/transfer, leading to improved efficiency from solar energy to H_2 .

In my work, I first investigated the core size effect in CdSe/CdS core/shell QDs for PEC H_2 generation. Generally, I synthesized four types of CdSe QDs with different size, varying from 2.8 nm to 4.8 nm in diameter by controlling the reaction time (2-10 min) under the same temperature (260 °C) via hot-injection approach. Afterwards, successive ionic layer adsorption and reaction (SILAR) method was further applied to coat similar thickness of CdS shell by controlling six monolayers, forming four types of CdSe/CdS core/shell QDs. Then transmission electron spectroscopy (TEM) and X-ray diffraction (XRD) pattern reveal that all four CdSe/CdS core/shell QDs were all ascribed to the same crystal structure with different size. In which the CdSe is turning to wurtzite (WZ) crystal structure while CdS is zinc blende (ZB) crystal structure. Also, the TEM images showed that the overall size of QDs is becoming larger with longer reaction time. The ultraviolet-visible (UV-vis) absorption (Abs) and photoluminescence (PL) spectra revealed that the position of the first-excitonic peaks vary from 585 nm to 635 nm while the peaks in PL spectrum vary from 595 nm to 648 nm. Finally, when four types of core/shell QDs were applied for PEC H_2 generation, the saturated photocurrent density (J_{ph}) varied from 8.8 mA/cm² to 17.4 mA/cm² under one sun illumination (AM 1.5 G, 100 mW/cm²). The PEC results indicated that the core size has significant influence on the band alignment as

well as the absorption range of core/shell QDs. In detail, the optimized PEC performance is based on the QDs with core size of 3.5 nm which balanced the absorption range of QDs as well as optimized carrier transfer efficiency.

In my second work, I investigated the composition effect of the CdS shell based on CdSe/CdS core/shell QDs. Generally, I synthesized three types of core/shell QDs. The first one is CdSe/CdS core/shell QDs with six monolayers of pure CdS shell. Then I engineered the shell composition into CdSe_xS_{1-x} alloyed shells. The two alloyed QDs are in the form of CdSe/(CdSe_{0.5}S_{0.5})₄/(CdS)₂ and CdSe/(CdSe_xS_{1-x})₅/CdS which denoted as CdSe/Alloyed#1 QDs and CdSe/Alloyed#2 QDs, respectively. The difference between the two alloyed QDs is the ratio of Se/S in each layer. When I applied the three types of core/shell QDs for PEC H₂ generation, the J_{ph} can reach 6.2 mA/cm² for CdSe/CdS QDs. For alloyed QDs, the J_{ph} can achieve as high as 15.1 mA/cm² and 17.5 mA/cm² for CdSe/Alloyed#1 QDs and CdSe/Alloyed#2 QDs, respectively. The dramatic improvement of PEC performance is mainly because the alloyed layers can not only enhance the absorption but also increase the carrier transfer efficiency by providing intermediate gradient layers. Thus, the unfavorable recombination can be largely reduced.

Though the PEC performance is quite promising, the stability performance is not qualified for long-term application. Based on this issue, in my third work, I concentrated on addressing the issue of poor stability performance of QDs based photoanode. One important reason for poor stability performance is the surface traps which will become the recombination center for carriers. One of the strategies is to coat a wide-bandgap semiconductor to passivate the surface. Based on this, I developed three types of QDs, CdSe/CdS core/shell QDs, CdSe/CdS/ZnS core/multiple shell QDs and CdSe/CdSe_xS_{1-x}/CdS/Cd_yZn_{1-y}S/ZnS alloyed QDs. When I applied three types of QDs for PEC H₂ generation, the saturated photocurrent density can reach 12.6 mA/cm² for CdSe/CdS core/shell QDs while 14.2 mA/cm² for CdSe/CdS/ZnS core/multiple shell QDs. For alloyed QDs, the saturated photocurrent density achieved unprecedented 20.5 mA/cm² under one sun illumination (AM 1.5 G, 100 mW/cm²). The PEC results indicated that the ZnS shell can act as the protection and passivation shell for QDs, reducing the

recombination events on the surface of QDs. Moreover, the alloyed intermediate layers can play the role of reducing the energy barrier between the shells, increasing the charge transfer efficiency accordingly. Then, I used three QDs for the stability measurement for two hours under one sun power. For CdSe/CdS core/shell QDs based photoanode, only 55 % of the initial current value was maintained for 2 hours. With the coating of ZnS shell, the CdSe/CdS/ZnS core/multiple shell QDs based photoanode can maintain 84 % of the initial current value after 2 hours while the alloyed QDs based photoanode showed the best stability performance, 93.4 % of the initial current value after 2-hour continuous illumination. This promising stability performance of alloyed QDs based photoanode also can be attributed to the effect of ZnS shell coating as well as the alloyed layers. Afterwards, I also investigated the impact of the shell thickness of the ZnS. Among one to three monolayers of ZnS shell, two monolayers of ZnS shell is proved to be the optimized shell thickness for PEC H₂ generation. In other words, one monolayer of ZnS is too thin to protect the QDs as well as passivate the surface of QDs while three monolayers of ZnS is too thick which will reduce the charge transfer efficiency.

Key words: PEC cell, quantum dots, core size effect, optical properties, alloyed shells, gradient band alignment, carrier transfer efficiency, charge recombination, theoretical calculation, core/multiple shell quantum dots, stability performance.

Acknowledgements

First, I would like to thank Prof. Federico Rosei and Prof. Xuhui Sun for providing me such advanced facilities and environment to conduct my research. They gave me plenty of advice and suggestion during my entire PhD career. I am grateful for their kindness and support. Prof. Rosei is a rigorous scientist who always pointed out my mistakes and slack during my research. He also helped me a lot with my writing. I learned a lot from him. Prof. Sun also helped me a lot when I came back to China. He supported the lab facilities for my research without considering the huge budget. I am really grateful for his generosity.

Secondly, I want to thank Prof. Haiguang Zhao who brought me to the research world of quantum dots. He also gave me lots of advice and directions during my PhD program. When I first saw him, he told me that we should concentrate on the science problems rather than just chase publications.

There is no doubt that it's an honor for me to be a part of "NFL group" of Prof. Rosei. I would like to acknowledge the collaborators who work with me closely in INRS-EMT, Canada. These people include: Dr. Xin Tong, Dr. Hui Zhang, Dr. Yufeng Zhou, Dr. Daniele Benetti, Dr. Lei Jin, Dr. Chao Wang, Dr. Basu Kaustubh, Dr. Fabiola Navarro-Pardo, Dr. Rusoma Akilimali, Dr. Mahyar Mohammadnezhad, Mr. Jiabin Liu, Mr. Faying Li, Mr. Li Shi, Ms. Na Xu, Ms. Xin Liu and many others. They worked closely with me when I was in INRS-EMT, Canada. Without them, I cannot learn so much during the research. Moreover, I would like to thank Prof. François Vidal, Prof. Dongling Ma, Prof. Ana Tavares, Prof. Shuhui Sun, Prof. Andreas Ruediger for all the help and support in INRS. I would like to thank all the staff and technicians in INRS-EMT center, especially Mrs. H el ene Sabourin, Mrs. Michelle Marcotte, Mrs. Tatiana Brahmi for their professionalism and their kindness.

When I came to China, continuing my study, many colleagues in FUNSOM, Soochow university helped me a lot. I am really grateful to these people: Dr. Duo Zhang, Dr. Zhen Wen, Dr. Hao Zhang, Dr. Mingfa Peng, Dr. Kun Feng, etc.

I also would like to thank my colleagues who work on the similar directions with me, Mr. Yi Tao, Mr. Zikun Tang. They always discussed with me and cheered me up. I also want to thank all the members in “Green group” of Prof. Xuhui Sun. We get along with each other in harmony.

I would like to thank to my family, my wife Yanting Lu who is my strong backup and always comforted me when I was down. My little daughter Yuxi Wang who came to the world during my PhD study is really a priceless gift to me and brighten the path in the future. I would like to thank my parents who not only gave my life, but also respect and support every decision that I made. And I am really grateful to my father-in-law and mother-in-law. They helped me a lot taking care of my daughter and family. Without them, I cannot finish the PhD program.

Finally, I would like to thank to all the staff, faculty members, administration in INRS-EMT and FUNSOM. They gave me a lot of support and advice. I am really appreciated their kindness.

Contents

Abstract	i
Acknowledgements	iv
List of Figures	ix
List of Tables	xvi
Chapter 1 Introduction and Background	1
1.1 Colloidal quantum dots and their properties	1
1.2 Core/shell quantum dots.....	3
1.3 Why choose CdSe/CdS core/shell QDs	6
1.4 Core/multiple shell QDs.....	9
1.5 Synthesis of quantum dots.....	9
1.6 Quantum dots for PEC hydrogen generation	11
1.7 Thesis objectives and contributions of this work	12
1.8 Thesis organization	13
Chapter 2 Experimental	15
2.1 Materials.....	15
2.2 Reaction setup	15
2.3 Synthesis.....	16
2.3.1 <i>Synthesis of CdSe QDs</i>	16
2.3.2 <i>Synthesis of CdSe/CdS core/shell QDs</i>	17
2.3.2 <i>Synthesis of CdSe/CdSe_xS_{1-x}/CdS alloyed QDs</i>	19
2.3.3 <i>Synthesis of CdSe/CdS/ZnS core/multiple shell QDs</i>	19
2.3.4 <i>Synthesis of CdSe/CdSe_xS_{1-x}/CdS/Cd_yZn_{1-y}S/ZnS core/multiple shell QDs</i>	20
2.4 Characterizations of QDs	21
2.4.1 <i>structure characterizations</i>	21

2.4.2 Property characterization	22
2.5 Fabrication of the photoanode	22
2.6 PEC and stability measurement	24
Chapter 3 CdSe/CdS QDs for PEC H₂ generation.....	25
3.1 Characterization of QDs	25
3.1.1 Structure of QDs	26
3.1.2 Optical properties of QDs	30
3.2 Carrier dynamic of QDs	34
3.3 Theoretical calculation of QDs	36
3.4 PEC and stability performance	40
3.5 Summary	47
Chapter 4 CdSe/CdSe_xS_{1-x}/CdS alloyed QDs for PEC H₂	
generation	49
4.1 Characterization of QDs	49
4.1.1 Structure of QDs	50
4.1.2 Optical properties of QDs	55
4.2 Carrier dynamics	56
4.3 Theoretical calculation	58
4.4 PEC and stability performance	60
Chapter 5 CdSe/CdS/ZnS core/multiple shell QDs for PEC H₂	
generation	70
5.1 Characterization of QDs	70
5.1.1 Structure of QDs	70
5.1.2 Optical properties of QDs	74
5.2 Carrier dynamics	76
5.3 Theoretical calculation	78
5.4 PEC and stability performance	79
5.5 The thickness impact of ZnS shell	86

5.6 Summary	92
Chapter 6 Conclusions and perspectives	94
6.1 Conclusions	94
6.2 Perspectives	95
Bibliography	98
APPENDIX A ABBREVIATIONS	112
APPENDIX B RÉSUMÉ	113
Production d'hydrogène photoélectrochimique à partir de points quantiques à noyau/coquille colloïdal	114
<i>Introduction</i>	114
<i>Objectifs de la thèse</i>	115
<i>Résultats et discussions</i>	117

List of Figures

Figure 1.1 (a) Schematic representation of the quantum confinement effects: the bandgap of the semiconductor nanocrystal increases with decreasing size, while discrete energy levels arise at the band-edges. The energy separation between the band-edge levels also increases with decreasing size; (b) Photograph of five colloidal dispersions of CdSe QDs with different sizes, under excitation with a UV lamp in the dark. The color of the photoluminescence changes from red to blue as the QD diameter is reduced from 6 to 2 nm.

Figure 1.2 Schematic diagram of the energy level alignment and carrier localization in Type I, Quasi-Type II and Type II.

Figure 1.3 Schematic diagram of CdSe/CdS core/shell QDs with the thickness increasing to CdS shell and corresponding band edge.

Figure 1.4 Schematic diagram of CdSe/CdS core/shell QDs and CdSe/CdSe_xS_{1-x}/CdS alloy QDs.

Figure 1.5 (a) Spectrum of solar radiation at the top of the atmosphere and at sea level from 230 nm to 2.6 μm wavelengths, adapted from literature; (b) Schematic representation for the emission range from variously representative QDs.

Figure 2.1 Schematic illustration of the air-free reaction setup for synthesizing CdSe QDs. The image demonstrates the hot-injection approach by separating the cation precursors and anion precursors in a three-necked bottle.

Figure 2.2 Schematic diagram of successive ion layer adsorption and reaction method for synthesizing the CdSe/CdS core/shell QDs with the deposition on CdSe QDs' surface.

Figure 3.1 TEM images of (a) CdSe (2.8 nm)/CdS QDs, (b) CdSe (3.1 nm)/CdS QDs, (c) CdSe (3.5 nm)/CdS QDs, (d) CdSe (4.8 nm)/CdS QDs (the insets show the HR-TEM images of corresponding QDs). (e) Size distribution of four types of CdSe/CdS core/shell QDs. The images indicate the increasing size of as-synthesized QDs.

Figure 3.2 SAED pattern of (a) CdSe (2.8 nm)/CdS QDs, (b) CdSe (3.1 nm)/CdS QDs, (c)

CdSe (3.5 nm)/CdS QDs, (d) CdSe (4.8 nm)/CdS QDs, respectively.

Figure 3.3 XRD pattern for CdSe (2.8 nm)/CdS QDs, CdSe (3.1 nm)/CdS QDs, CdSe (3.5 nm)/CdS QDs and CdSe (4.8 nm)/CdS QDs. JCPDS card of WZ CdSe and ZB CdS are used for identification.

Figure 3.4 Cross-sectional SEM image and EDS mapping of CdSe (3.5 nm)/CdS QDs/TiO₂ (in the selected area surrounded by the white line): the elemental distributions of (b) Ti, (c) O, (d) Cd, (e) Se and (f) S. And the white arrow indicates the thickness is 22 μm of the film.

Figure 3.5 UV-vis absorption spectra of (a) CdSe (2.8 nm) QDs, CdSe (3.1 nm) QDs, CdSe (3.5 nm) QDs and CdSe (4.8 nm) QDs; (b) CdSe (2.8 nm)/CdS QDs, CdSe (3.1 nm)/CdS QDs, CdSe (3.5 nm)/CdS QDs and CdSe (4.8 nm)/CdS QDs.

Figure 3.6 PL spectrum of four CdSe core QDs (CdSe (2.8 nm) QDs, CdSe (3.1 nm) QDs, CdSe (3.5 nm) QDs and CdSe (4.8 nm) QDs and four CdSe/CdS core/shell QDs (CdSe (2.8 nm)/CdS QDs, CdSe (3.1 nm)/CdS QDs, CdSe (3.5 nm)/CdS QDs and CdSe (4.8 nm)/CdS QDs).

Figure 3.7 Images of four types of CdSe QDs (CdSe (2.8 nm) QDs, CdSe (3.1 nm) QDs, CdSe (3.5 nm) QDs and CdSe (4.8 nm) QDs) with different size (a) under sunlight (b) under UV light; Images of four types of CdSe QDs with different size (CdSe (2.8 nm)/CdS QDs, CdSe (3.1 nm)/CdS QDs, CdSe (3.5 nm)/CdS QDs and CdSe (4.8 nm)/CdS QDs) under (c) under sunlight (d) under UV light.

Figure 3.8 PL decay spectra of (a) CdSe (2.8 nm)/CdS core/shell QDs (b) CdSe (3.1 nm)/CdS core/shell QDs (c) CdSe (3.5 nm)/CdS core/shell QDs and (d) CdSe (4.8 nm)/CdS core/shell QDs after deposited into TiO₂ films, ZrO₂ films and ZrO₂ films in the presence of an electrolyte with the excitation light of 444 nm.

Figure 3.9 UPS spectra of (a) CdSe (2.8 nm) QDs (b) CdSe (3.1 nm) QDs (c) CdSe (3.5 nm) QDs (d) CdSe (4.8 nm) QDs and high, low binding energy cutoff.

Figure 3.10 Schematic diagram of four CdSe core QDs (CdSe (2.8 nm) QDs (b) CdSe (3.1 nm)

QDs (c) CdSe (3.5 nm) QDs (d) CdSe (4.8 nm) QDs) and their band position (conduction/valence band) calculated following the UPS results.

Figure 3.11 (a) Spatial probability distribution value $\rho(r)$ of electrons and holes as a function of QD radius (nm) for four CdSe/CdS core/shell QDs (CdSe (2.8 nm)/CdS QDs, CdSe (3.1 nm)/CdS QDs, CdSe (3.5 nm)/CdS QDs and CdSe (4.8 nm)/CdS QDs) (dashed lines show the radius position and the shadow areas indicate the electrons in the shell regions); (b) the overlapping area and electron leakage area as the function of core radius.

Figure 3.12 Schematic diagram of PEC cell based on CdSe/CdS QDs. The images show the structure of the photoanode which includes the glass, FTO, blocking layer, QDs and TiO₂ mesoporous films and the cathode is used Pt sheet while electrolyte is used SO₃²⁻/S²⁻.

Figure 3.13 HR-TEM image of CdSe (3.5 nm)/CdS QDs onto mesoporous TiO₂ film where the white circle indicates the position of QDs.

Figure 3.14 Photocurrent density-potential dependence of TiO₂ sensitized with four types of CdSe core QDs (CdSe (2.8 nm) QDs (b) CdSe (3.1 nm) QDs (c) CdSe (3.5 nm) QDs (d) CdSe (4.8 nm) QDs) in the dark (black dashed curves), and under continuous (chromatic curves) illumination (AM 1.5 G, 100 mW cm⁻²).

Figure 3.15 Photocurrent density-potential dependence of TiO₂ sensitized with four types of CdSe/CdS core/shell QDs (CdSe (2.8 nm)/CdS QDs, CdSe (3.1 nm)/CdS QDs, CdSe (3.5 nm)/CdS QDs and CdSe (4.8 nm)/CdS QDs) in the dark (black dashed curves), and under continuous (chromatic curve) illumination (AM 1.5 G, 100 mW cm⁻²).

Figure 3.16 (a) Photocurrent density-potential dependence of TiO₂ sensitized with alloyed CdSe/CdSeS/CdS QDs in the dark (black curve), under continuous (magenta curve) and chopped (blue curve) illumination; (b) Photo photocurrent density versus time of alloyed QDs with the control of light on/off which indicates the photoresponse of as-prepared photoanode.

Figure 3.17 IPCE spectra of four types of CdSe/CdS core/shell QDs (CdSe (2.8 nm)/CdS QDs, CdSe (3.1 nm)/CdS QDs, CdSe (3.5 nm)/CdS QDs and CdSe (4.8 nm)/CdS QDs) under one sun power.

Figure 3.18 Stability measurements (photocurrent density as a function of time) of the four types of CdSe/CdS QDs (CdSe (2.8 nm)/CdS QDs, CdSe (3.1 nm)/CdS QDs, CdSe (3.5 nm)/CdS QDs and CdSe (4.8 nm)/CdS QDs) and alloyed CdSe/CdSeS/CdS QDs based photoanode at 0.6 V versus RHE under AM 1.5 G illumination (100 mW cm^{-2}) with 2 ZnS coating.

Figure 3.19 (a) Photocurrent density and (b) stability retention of four CdSe/CdS core/shell QDs (CdSe (2.8 nm)/CdS QDs, CdSe (3.1 nm)/CdS QDs, CdSe (3.5 nm)/CdS QDs and CdSe (4.8 nm)/CdS QDs) and alloyed CdSe/CdSeS/CdS QDs.

Figure 4.1 TEM images and QDs structure of (a) CdSe/6CdS; (b) CdSe/Alloy#1; (c) CdSe/Alloy#2 and the insets show the structure of as-synthesized QDs.

Figure 4.2 Size distribution of CdSe/6CdS, CdSe/Alloy#1 and CdSe/Alloy#2 QDs.

Figure 4.3 HR-TEM image of CdSe/Alloyed#2 QDs and the fringe indicates the (111) crystal plane of ZB crystal structure of CdSe.

Figure 4.4 Selected area electron diffraction pattern: (a) CdSe/Alloy#1 QDs, (b) CdSe/Alloy#2 QDs.

Figure 4.5 XRD pattern of CdSe, CdSe/6CdS, CdSe/Alloy#1 and CdSe/Alloy#2 QDs where the JCPDS card of ZB CdSe, WZ CdSe and WZ CdS are used for identification.

Figure 4.6 High-resolution XPS spectra of Cd 3d, Se 3d and S 2p in as-prepared CdSe/Alloy#2 QDs. The black dots are as-measured lines and the red lines represent the fitting lines.

Figure 4.8 PL spectra of CdSe/6CdS, CdSe/Alloy#1 and CdSe/Alloy#2 QDs after deposited into TiO₂ films, ZrO₂ film and ZrO₂ film in the presence of electrolyte.

Figure 4.8 PL spectra of CdSe/6CdS, CdSe/Alloy#1 and CdSe/Alloy#2 QDs after deposited into TiO₂ films, ZrO₂ film and ZrO₂ film in the presence of electrolyte.

Figure 4.9 Spatial probability distribution value $\rho(r)$ of the electron and hole as a function of QD radius (nm) for CdSe/6CdS, CdSe/Alloy#1 and CdSe/Alloy#2 QDs (dashed lines show the positions of the peaks).

Figure 4.10 Schematic diagram of band structure and carrier transition of CdSe/Alloy#2 QDs based photoanode. Approximate energy levels of TiO₂ and QDs, together with related characteristic redox potentials. The arrows show the electron and hole transfer processes.

Figure 4.11 (a) Cross-sectional SEM image of CdSe/CdS QD-sensitized photoanode. EDS mapping analysis of all the elements including (b) Ti, (c) O, (d) Se (e) Cd and (f) S. (g) EDS line mapping of the highlighted path in the SEM image and (h) EDS spectrum. The yellow line indicates 21.5 μm of the film thickness.

Figure 4.12 Photocurrent density-potential dependence of TiO₂ sensitized by (a) CdSe/6CdS QDs; (b) CdSe/Alloy#1 QDs; (c) CdSe/Alloy#2 QDs in the dark (black curve), under continuous (red curve) and chopped (blue curve) illumination (AM 1.5 G, 100 mW/cm²).

Figure 4.13 Photocurrent density versus bias potential (versus RHE) for TiO₂/CdSe/Alloy#2 with 3 and 4 cycles of ZnS photoanodes in the dark and under continuous illumination (AM 1.5 G, 100 mW/cm²).

Figure 4.14 Stability spectra of the photoanode based on CdSe/Alloy#2 QDs with 2 cycles of ZnS coating for 2 hours under 0.6 V vs RHE with continuous one sun power.

Figure 4.15 Stability measurements (photocurrent density as a function of time) of CdSe/Alloy#2 QDs based photoanode at 0.6 V versus RHE under AM 1.5 G illumination (100 mW/cm²) (a) with different treatment (Annealing, different cycles of ZnS coating and SiO₂ coating) and (b) normalized stability spectra of the sample CdSe/Alloy#2 with different treatment (annealing, different cycles of ZnS coating and SiO₂ coating) (c) with annealing-3ZnS-SiO₂ treatment.

Figure 4.16 PL spectra of CdSe/6CdS, CdSe/Alloy#1 and CdSe/Alloy#2 QDs as function of different cycles of ZnS.

Figure 5.1 TEM images of (a) CdSe/6CdS QDs, (b) CCZ-1 QDs and (c) CCZ-2 QDs where the right corner insets showed the HR-TEM images of corresponding QDs.

Figure 5.2 SAED pattern of CCZ-1 and CCZ-2 QDs.

Figure 5.3 XRD pattern of CdSe, CdSe/CdS, CCZ-1 and CCZ-2 QDs. The JCPDS card of WZ

CdSe, ZB CdS and ZB ZnS are used for identification.

Figure 5.4 High-resolution XPS spectra of Cd 3d, Se 3d, S 2p and Zn 2p in as-prepared CCZ-1 QDs.

Figure 5.5 The UV-vis absorbance spectrum of CdSe, CdSe/6CdS, CCZ-1 and CCZ-2 QDs (the inset shows the enlarged image of the peaks with the multiple of 15).

Figure 5.6 PL spectra of CdSe, CdSe/6CdS, CCZ-1 and CCZ-2 QDs.

Figure 5.7 PL decay spectra of CdSe/6CdS, CCZ-1 and CCZ-2 QDs after deposited into TiO₂ films, ZrO₂ films and ZrO₂ films in the presence of an electrolyte.

Figure 5.8 Spatial probability distribution value $\rho(r)$ of electrons and holes as a function of QD radius (nm) for CdSe/6CdS, CCZ-1 and CCZ-2 QDs (dashed lines show the positions of the peaks).

Figure 5.9 Schematic diagram of the band structure and carrier transition of (a) the CCZ-1 (b) CCZ-2 QDs based photoanode. Approximate energy levels of TiO₂ and QDs, together with related characteristic redox potentials.

Figure 5.10 TEM image of CCZ-2 QDs in the mesoporous TiO₂ film (white circles indicate the position of QDs).

Figure 5.11 (a) Cross-sectional SEM image of CdSe/CdSe_{0.5}S_{0.5}/CdS/Cd_{0.5}Zn_{0.5}S/ZnS QD-sensitized photoanode and relevant EDS 2D mapping of all the elements including b) Ti, c) O, d) Cd, e) Zn, f) Se, g) S. And the white line indicates the thickness is 20 μm of the film.

Figure 5.12 Photocurrent density-potential dependence of TiO₂ sensitized with CdSe/6CdS QDs, CCZ-1 QDs and CCZ-2 QDs in the dark (black curve), and under continuous (chromatic curve) illumination (AM 1.5 G, 100 mW cm⁻²).

Figure 5.13 Stability measurements (photocurrent density as a function of time) of the CdSe/6CdS QDs, CCZ-1 QDs and CCZ-2 QDs based photoanode at 0.6 V versus RHE under AM 1.5 G illumination (100 mW cm⁻²) with 2 ZnS coating.

Figure 5.14 Theoretical and experimental H₂ evolution of CCZ-2 QDs/TiO₂ photoanodes during 120 min under one sun illumination (AM 1.5 G, 100 mW/cm²) with a bias of 0.6 V vs RHE.

Figure 5.15 TEM images of CdSe/4CdS/ZnS, CdSe/4CdS/2ZnS and CdSe/4CdS/3ZnS QDs with different thickness of ZnS shells.

Figure 5.16 Absorption spectra of CdSe/4CdS/ZnS, CdSe/4CdS/2ZnS and CdSe/4CdS/3ZnS QDs.

Figure 5.17 PL decay spectra of CdSe/4CdS/ZnS QDs, CdSe/4CdS/2ZnS QDs and CdSe/4CdS/3ZnS QDs in the toluene. The dots are measured data and red lines represent fitting curves.

Figure 5.18 PL spectra of CdSe/4CdS/ZnS QDs, CdSe/4CdS/2ZnS QDs and CdSe/4CdS/3ZnS QDs after deposited into TiO₂ films, ZrO₂ films and ZrO₂ films in the presence of an electrolyte. The dots are measured data and red lines represent fitting curves.

Figure 5.19 Photocurrent density-potential dependence of TiO₂ sensitized with (a) CdSe/4CdS/ZnS QDs, CdSe/4CdS/2ZnS QDs; and CdSe/4CdS/3ZnS QDs in the dark (black dashed curves), and under continuous illumination (AM 1.5 G, 100 mW cm⁻²).

List of Tables

Table 3.1 Size and optoelectronic parameters of as-prepared QDs.

Table 3.2 Lifetime with different substrates and charge transfer rate.

Table 3.3 Potential (respect to vacuum) of CB, VB and Fermi level for different QDs following the UPS.

Table 3.4 Calculated electron-hole (e-h) overlapping area variations from the theoretical measurements for 4 CdSe/6CdS core/shell QDs as the function of CdSe core size.

Table 4.1 Ratio of Se/S in shell as function of SILAR cycles.

Table 4.2 Diameter and shell thickness of three types of QDs.

Table 4.3 Optical parameters of three types of QDs in toluene.

Table 4.4 Lifetime with different substrates and charge transfer rate.

Table 4.5 The radius of core, thickness of shell and e-h spatial overlapping values for CdSe/6CdS, CdSe/Alloy#1 and CdSe/Alloy#2 QDs.

Table 4.6 Lifetime in ZrO₂ with and without electrolyte and corresponding hole transfer rate for CdSe/6CdS, CdSe/Alloy#1 and CdSe/Alloy#2 QDs with different cycles of ZnS coating.

Table 5.1 Size parameters of CdSe/6CdS, CCZ-1 and CCZ-2 QDs.

Table 5.2 Optoelectronic parameters of CdSe/6CdS, CCZ-1 and CCZ-2 QDs.

Table 5.3 Lifetime with different substrates and charge transfer rate.

Table 5.4 Lifetime in toluene of CdSe/4CdS/ZnS, CdSe/4CdS/2ZnS and CdSe/4CdS/3ZnS QDs.

Table 5.5 Lifetime with different substrates and charge transfer rate.

Table 5.6 Previous work of colloidal QDs based photoanode for PEC H₂ generation.

Chapter 1 Introduction and Background

1.1 Colloidal quantum dots and their properties

Colloidal quantum dots (QDs) are usually defined as semiconductor nanocrystals (NCs). The size of QDs is usually less than 20 nm in diameter.^{1,2} Typically, they are composed of an inorganic core, made of a few hundred to a few thousand atoms, surrounded by an organic outer layer of surfactant molecules (ligands).^{3,4} Semiconductor QDs exhibit dramatic quantization effects, defined by an increasing bandgap accompanied by quantization of the energy levels in discrete values, similar to atomic energy levels. In most semiconductors, once the size is reduced to a few nanometers, quantum confinement occurs, leading to size-dependent optoelectronic properties of QDs. Such size effects allow us to design and synthesize QDs with controllable size, shape, and chemical composition to precisely tune the optical transitions and the energy of discrete electronic energy states.⁵⁻¹¹ For example, as shown in Figure 1.1, the CdSe nanocrystals are controlled from 6 nm to 2 nm in diameter which determines the different discrete energy levels at the band-edges. This effect is commonly referred to as quantum confinement, and makes it possible to tune the optical spectra (absorption and photoluminescence, PL) of semiconductor NCs through a wide spectral window by simply changing their size, while keeping their composition constant [the PL effect of different size is shown in Figure 1.1(b)].

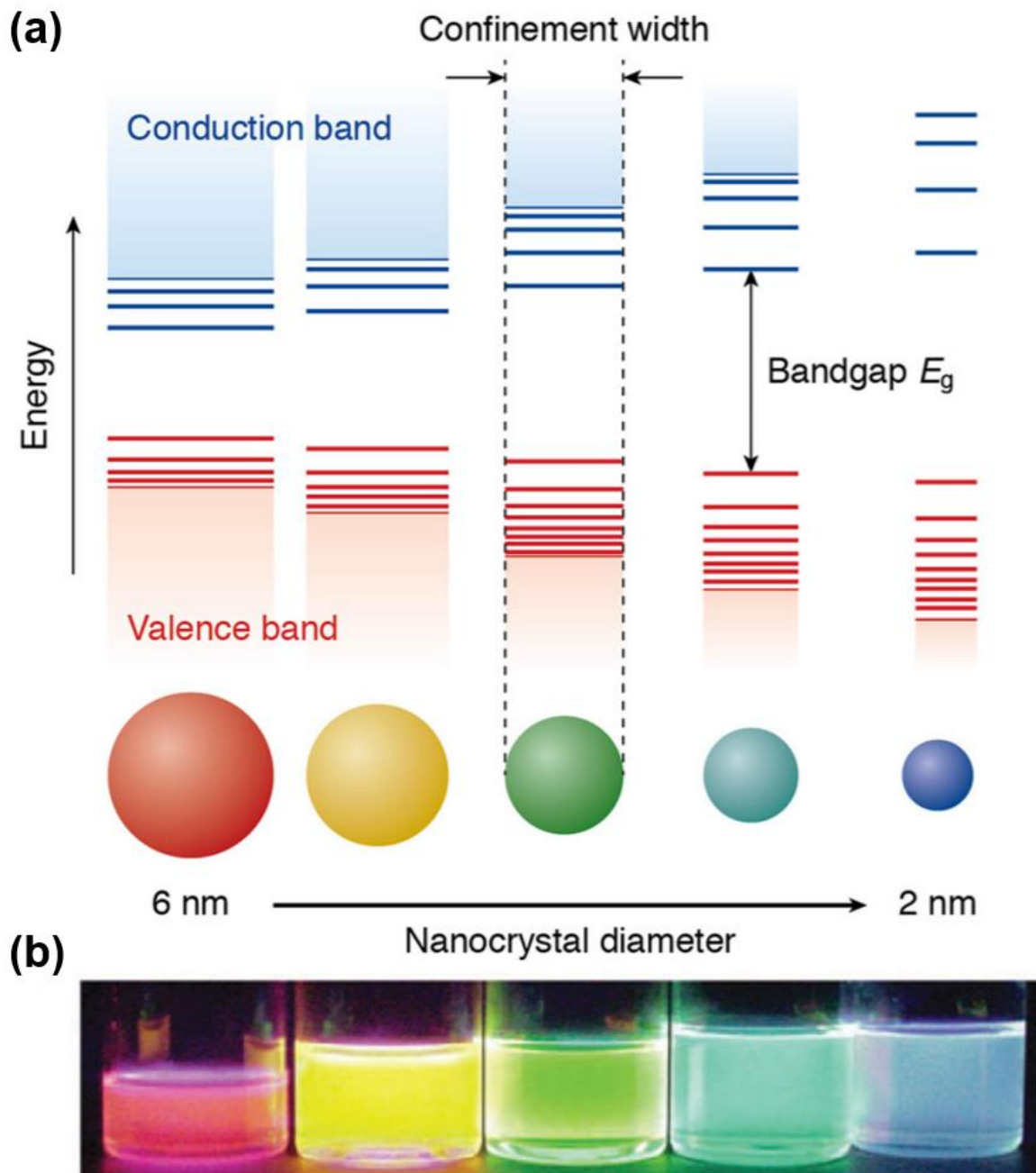


Figure 1.1 (a) Schematic representation of the quantum confinement effects: the bandgap of the semiconductor nanocrystal increases with decreasing size, while discrete energy levels arise at the band-edges. The energy separation between the band-edge levels also increases with decreasing size; (b) Photograph of five colloidal dispersions of CdSe QDs with different sizes, under excitation with a UV lamp in the dark. The color of the photoluminescence changes from red to blue as the QD diameter is reduced from 6 to 2 nm. The image is adapted from literature¹².

1.2 Core/shell quantum dots

Since the size of QDs is small (less than 20 nm), leading to large surface-to-volume ratio. Though the ligands on the surface can stabilize the QDs by passivating the dangling bonds. The interaction of QDs and ligands are weak. Therefore, the properties of QDs are sensitive to the environmental change of surface and ligands, such as moisture, temperature and illumination. Recently study reveals that growing a shell on the surface of the core QDs can improve the photostability of QDs, and quantum yield (QY).¹³⁻²¹ Thus, core/shell structure is becoming a more attractive semiconductor material for optoelectronic devices compared to bare QDs, such as solar cell and photoelectrochemical (PEC) cell.²²⁻²⁵ In particular, the core/shell QD consists of a core QD of one semiconductor material and a shell of another semiconductor material on the out-layer of the core. By the difference of the band alignment between the core and shell, the core/shell QDs can be classified into Type I, Type II and Quasi-Type II. In Type I structured core/shell QDs, the bandgap of the core is smaller than that of the shell, and both band edges of the core are located in the band gap of the shell. Therefore, both electrons and holes are confined in the core regions, leading to fewer interactions of core localized e-h pairs with surface traps than that of bare QDs and thus enhanced QY and photo- and thermal- stability over that of pure QDs.^{22,26} In the Type II core/shell structure, either the conduction band (CB) edge or the valence band (VB) edge of the shell is located in the bandgap of the core. The band alignment causes spatial separation of the electrons and holes into different regions of the core/shell structure.^{27,28} A special case is called Quasi-Type II. In this case, only one type of carrier is delocalized over the entire core-shell structure, whereas the other type of carrier is confined in the core.^{21,29,30} The schematic diagram is shown in Figure 1.2.

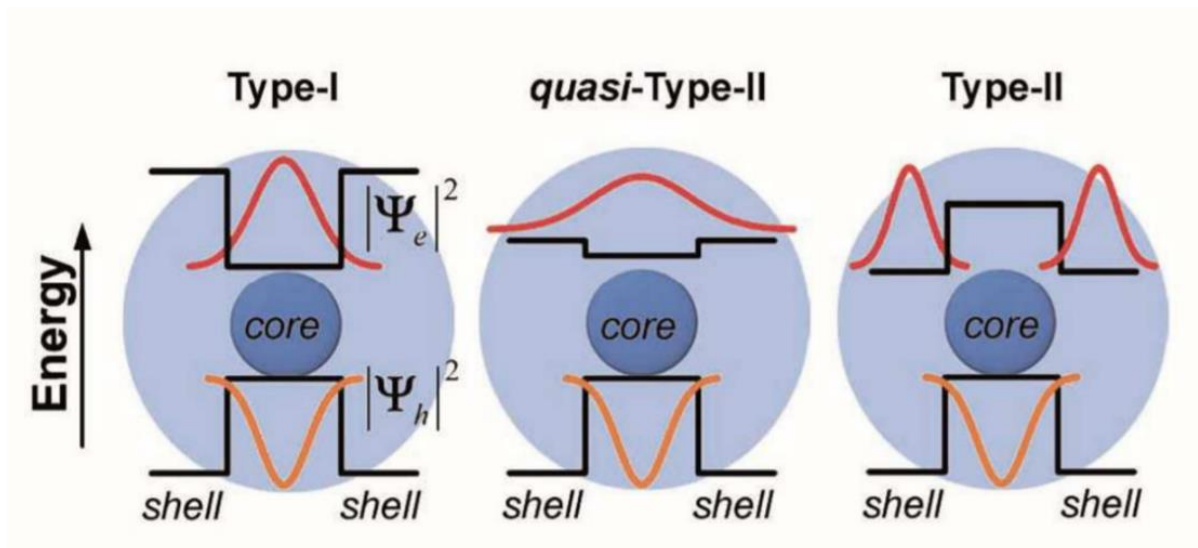


Figure 1.2 Schematic diagram of the energy level alignment and carrier localization in Type I, Quasi-Type II and Type II. The image is adapted from literature³¹.

There are some typical types of core/shell QDs, such as “Giant” QDs which consist of a small core and thick shell,³²⁻³⁹ and alloyed QDs which consist of more than one type of anion or cation.⁴⁰⁻⁴² Such types of core/shell QDs offer more possibility to tune the band alignment or carrier dynamics for improved optical and electrical properties of QDs compared to pure-shell QDs. For example, “Giant” core/shell QDs (in which the shell is very thick, from 1.5 nm up to 20 nm, and the core exhibits quantum confinement behavior) have been widely studied because of their superior chemical and photostability over both pure QDs and thin-shell QDs (as shown in Figure 1.3). A thicker shell can efficiently protect the core material, insulating it from QD surface chemistry and the surrounding chemical environment. More importantly, for suitably tailored compositions and electronic band structures, the lifetime of excitons generated in the core can be significantly longer than pure and thin-shell QDs as a result of efficient leakage of the electrons in the shell regions, forming a Quasi-Type II band alignment.

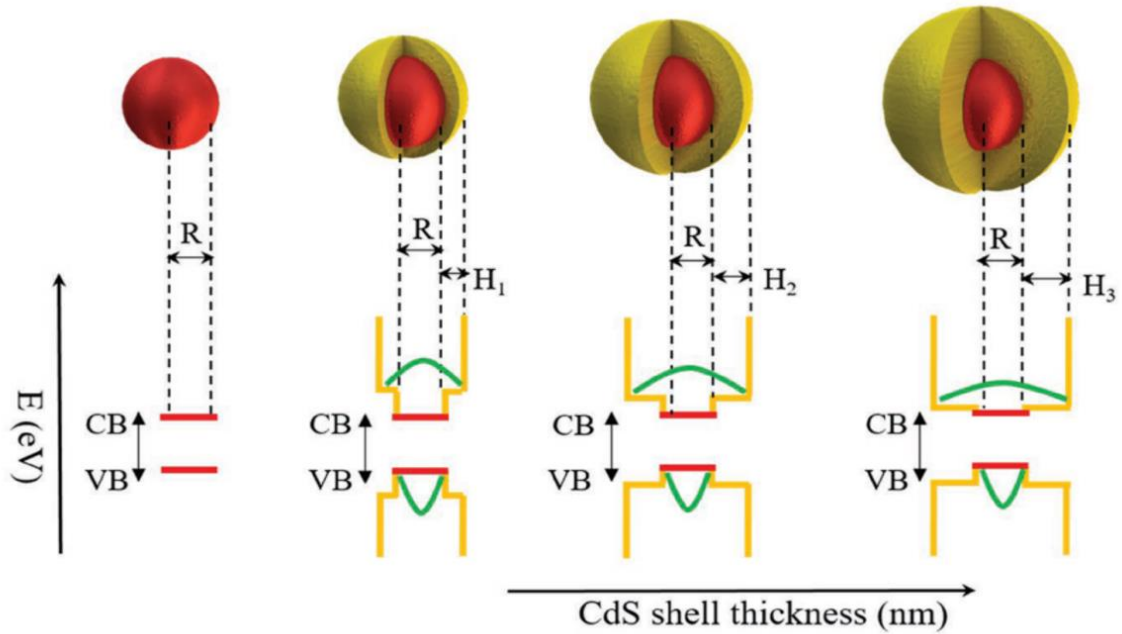


Figure 1.3 Schematic diagram of CdSe/CdS core/shell QDs with the thickness increasing to CdS shell and corresponding band edge. The image is adapted from literature.³⁶

There are another QDs type so-called alloyed QDs which the core and/or shell composition consist of more than one anion/cation. As shown in Figure 1.4, the CdS shell in CdSe/CdS core/shell QDs was replaced with $\text{CdSe}_x\text{S}_{1-x}$ alloyed shells. As a result, such alloyed core/shell QDs can broaden the absorption range by tailing the composition of the shell and more importantly, more favorable band alignment can be built, leading to more efficient carriers' separation/transfer and less possibility of recombination.

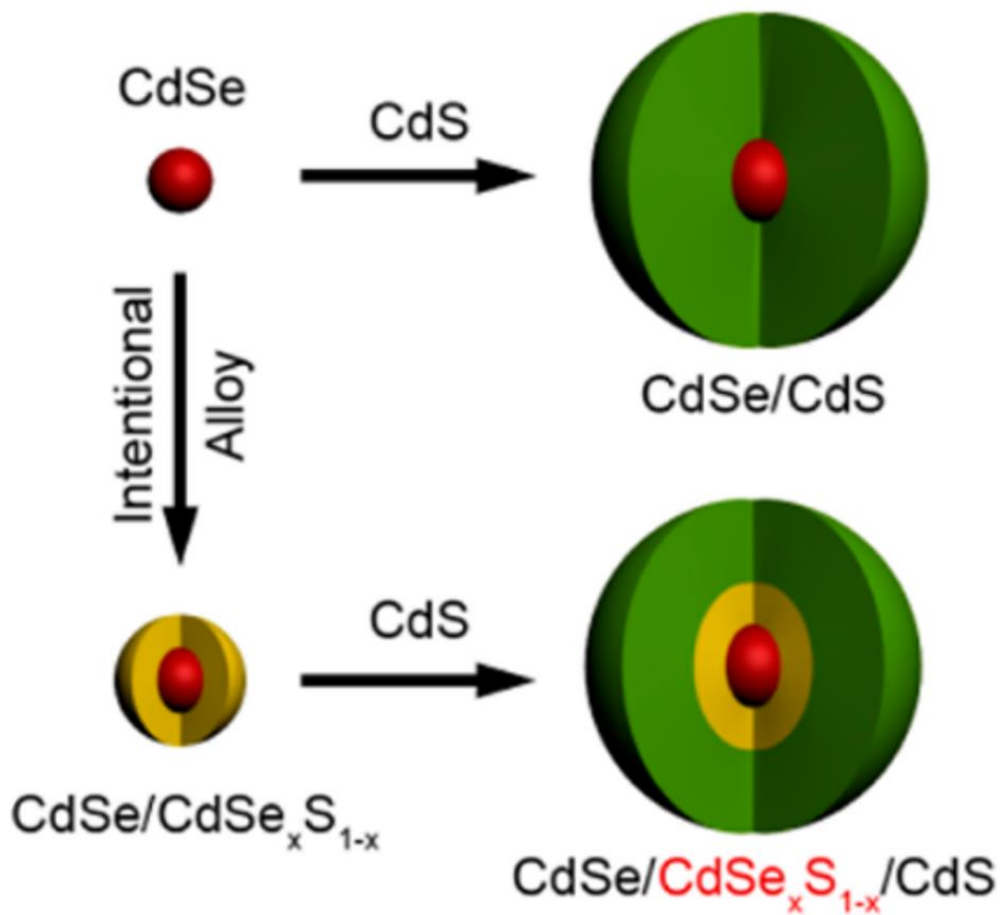
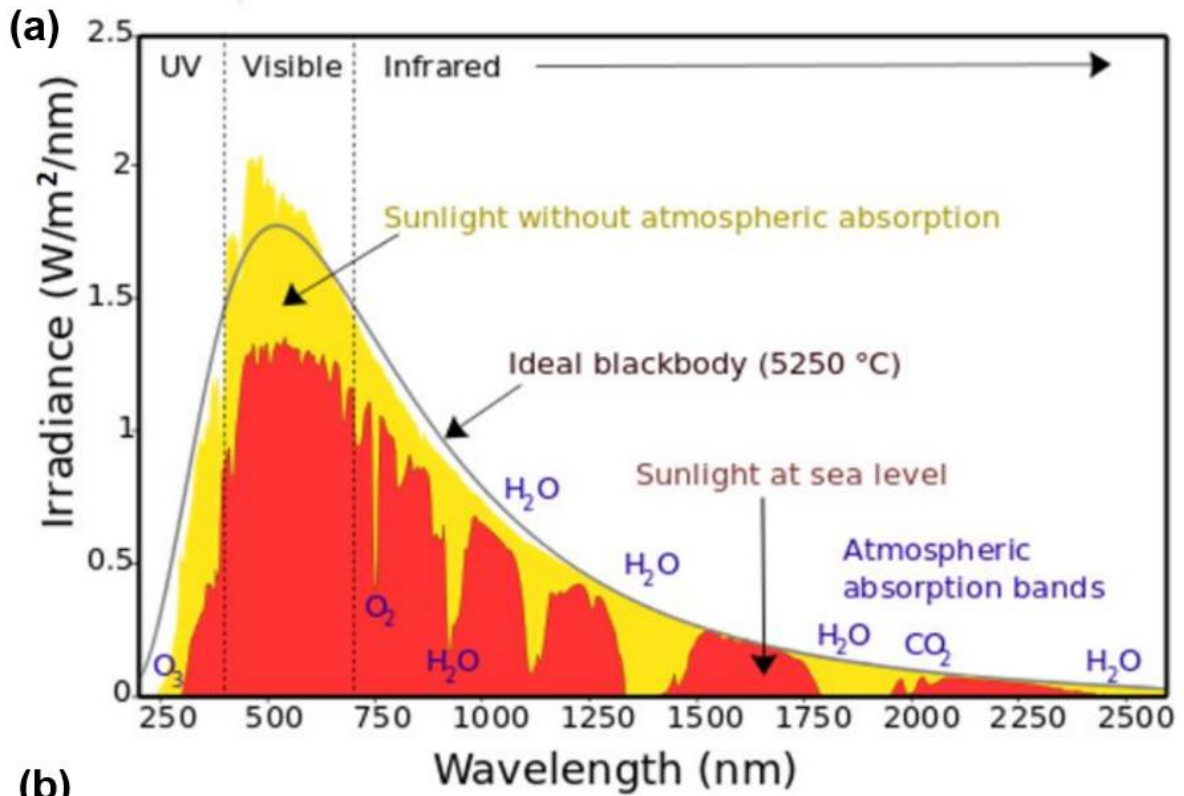


Figure 1.4 Schematic diagram of CdSe/CdS core/shell QDs and CdSe/CdSe_xS_{1-x}/CdS alloy QDs. The image is adapted from literature.⁴²

1.3 Why choose CdSe/CdS core/shell QDs

As shown in Figure 1.5 (b), there are lots of choices of QDs or core/shell QDs as the light harvesters, which can cover different ranges of entire solar spectrum. However, according to Figure 1.5 (a), visible light (~380-700 nm) occupies high intensity of solar irradiation. Thus, to efficiently use the solar irradiation, CdSe/CdS architecture could be one of the promising candidates as the light harvester. Moreover, due to the band offset of CdSe/CdS core/shell system, the band alignment of CdSe/CdS core/shell can be adjusted for improved carrier transfer efficiency. Finally, few lattice mismatch (~3.9 %) between CdSe and CdS two semiconductors also plays an important role for high solar to electricity or solar to fuels conversion efficiency.¹³ Due to these favorable properties, CdSe/CdS core/shell architecture is

still one of the most efficient architectures for optoelectronic devices. For example, Adhikari et al.⁴³ reported CdSe/CdS core/shell QDs with the same core radius of 1.65 nm and different shell thickness of 0 nm, 2.18 nm and 4.3 nm, sensitizing TiO₂ for PEC H₂ evolution, which exhibited the highest saturated photocurrent density of 8.9 mA/cm² under one sun illumination (AM 1.5 G, 100 mW/cm⁻²) based on the shell thickness of 4.3 nm. Selopal et al.³⁶ reported CdSe/CdS core/shell QDs with the core radius of 1.65 nm and shell thickness of 0 nm, 0.66 nm, 1.96 nm and 4.51 nm, sensitizing TiO₂ for QDs sensitized solar cells, which exhibited the photoconversion efficiency (PCE) of 3.01 % based on the QDs with the shell thickness of 1.96 nm. Up to date, there are many works reporting the shell thickness optimization based on CdSe/CdS core/shell QDs for optoelectronic devices. However, there are few works focusing on the core size of CdSe QDs as well as the core/shell band alignment between the core and shell. Thus, in my first work, I tried to investigate the core size effect of CdSe based on CdSe/CdS core/shell QDs for the PEC H₂ evolution.



(b)

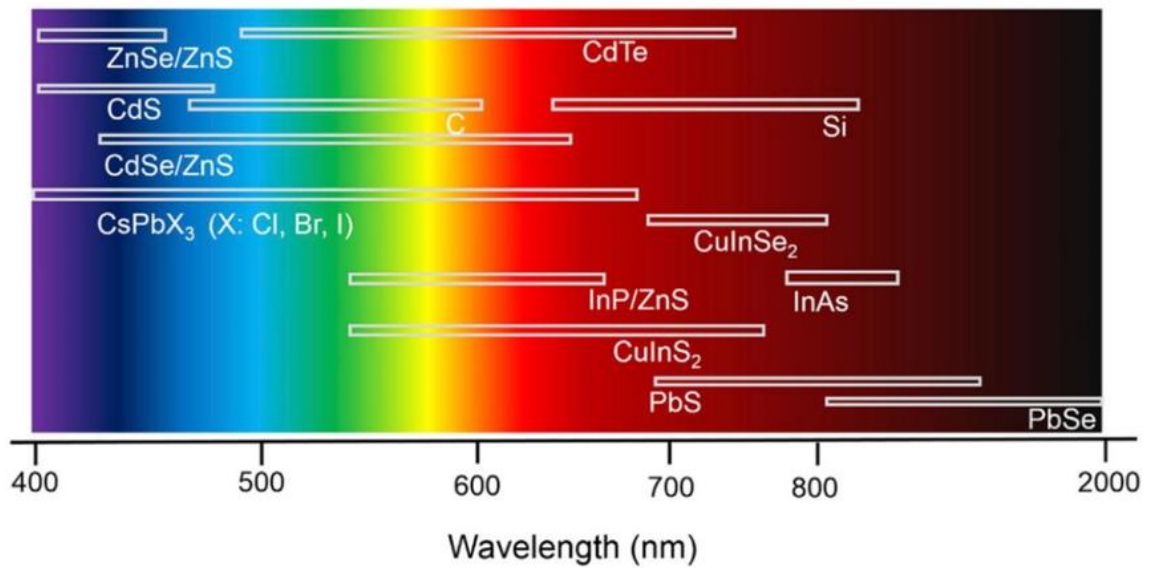


Figure 1.5 (a) Spectrum of solar radiation at the top of the atmosphere and at sea level from 230 nm to 2.6 μm wavelengths, adapted from literature; (b) Schematic representation for the emission range from variously representative QDs, adapted from literature.¹⁴

1.4 Core/multiple shell QDs

As discussed above, core/shell QDs architecture is a promising strategy to improve the QY and stability of QDs. However, due to the limited selection of shell materials, it is still difficult to respond simultaneously to the requirements of appropriate electronic (bandgap, band alignment) and structural (lattice mismatch) parameters for most binary core/shell systems. For example, two most popular core/shell architectures, CdSe/CdS and CdSe/ZnS.^{20,44,45} The CdS shell is a good candidate as the shell material for CdSe core due to less mismatch with CdSe as well as efficient carrier separation and transfer brought by favorable band alignment. However, the surface of CdSe core cannot be efficiently passivated by CdS shell. While ZnS is an ideal surface passivation material with wide bandgap, but absorption range of ZnS shell is limited with inefficient carrier transfer rate from CdSe core to ZnS shell. Moreover, the lattice mismatch between CdSe and ZnS is over 10 %, much larger than CdSe/CdS (3.9 %) system. Based on these reasons, core/multiple shell QDs were developed to reduce the lattice mismatch by providing intermediate “lattice adapter”. For example, CdSe/CdS/ZnS,⁴⁶⁻⁴⁸ CdSe/ZnSe/ZnS,^{46,49} such architectures can not only reduce the lattice mismatch, but also improve the carrier transfer efficiency by providing cascade band alignment. Moreover, ZnSe and ZnS are good candidates as the shell materials to passivate the surface of core QDs.⁵⁰⁻⁵² In the chapter 5 of the thesis, core/multiple shell QDs and its corresponding alloyed QDs were designed and synthesized for the application of PEC cells.

1.5 Synthesis of quantum dots

There are lots of methods to synthesize QDs, such as wet-chemical synthesis, plasma synthesis, etc. In this thesis, all the synthesis of QDs is via wet-chemical approach which the properties of QDs can be precisely controlled. Generally, the synthesis of core/shell and core/multiple shell QDs is divided into two parts. Firstly, the CdSe core QDs were synthesized through hot-injection approach which belongs to wet chemical synthesis category.⁵³⁻⁵⁵ Such methodology is especially powerful for the convenient and reproducible synthesis of highly monodisperse colloidal QDs, because it allows the size, structure, and chemical composition of the resulting

NCs to be tuned. Also, high-quality QDs with different sizes and size distribution, high photoluminescence quantum yield (PLQY), and good photo- and thermal- stability have been synthesized almost exclusively via a high-temperature organometallic route by the hot-injection method.

Typically, for synthesis of CdSe QDs, cadmium oxide (CdO), oleic acid (OA) and oleylamine (OLA) were loaded in a three-necked flask. At about 240-260 °C, the reddish CdO powder was dissolved and generated a colorless homogeneous solution. After the formation of the Cd(OA)₂-ODE complex, an injection of selenium dissolved in octadecene (ODE) at 250-300 °C generated CdSe NCs. Tunable particle sizes of CdSe QDs in the range of 2-8 nm can be synthesized by changing the growth temperature and reaction time. The as-produced CdSe QDs exhibit a typical emission in the wavelength range 450-650 nm.

Secondly, to form core/shell QDs, other methods are applied to grow another semiconductor materials on the surface of core QDs. Several approaches have been reported, including injection of a mixture of cationic and anionic precursors at the growth temperature or alternative injections of cationic and anionic precursors [also named successive ionic layer adsorption and reaction (SILAR) approach].⁵⁶ To prevent homogeneous nucleation of the shell material and uncontrolled ripening of the core NCs, the temperature for shell growth (T_2) is generally lower than that used for the core NC synthesis. For example, for the synthesis of CdSe/CdS core/shell QDs, core QDs of CdSe were first synthesized via a hot-injection approach at 300-320 °C. After purification, CdSe QDs were dispersed in ODE and OLA. The mixture was then heated to 240 °C in N₂ for shell growth. Equimolar amounts of the Cd/S precursor mixture solution were slowly injected into the core mixture. The shell thickness can be controlled by adjusting the SILAR cycles and precursor volumes. Also, the shell composition can be changed through the replacement of the precursors. SILAR is a good methodology for shell growth of NCs due to the precise control of the shell thickness and composition and it can also prevent undesirable ripening.^{57,58}

For calculation of core size and precursors volume for shell growth, the Beer-Lambert's law was used to estimate the diameter of the core from the absorption spectrum of QDs.^{13,59,60} The

equation is shown below:

$$A = \epsilon CL \quad (1.1)$$

Where A is the absorbance at the peak position of the first-excitonic absorption peak while ϵ is the extinction coefficient. C is the molar concentration of QDs and L is the light path length, respectively. In my thesis, A is measured by UV-visible spectroscopy. L is determined by the path length of light in the cuvette (1 cm). ϵ can be determined by the following equation for CdSe core:

$$\epsilon = 5857(D)^{2.65} \quad (1.2)$$

Where D is the diameter of CdSe core estimated from absorption spectra of CdSe QDs. Thus, the concentration of QDs can be easily determined using the Beer-Lambert's law. By pumping out certain volume of QDs suspension, the amount of QDs can be determined. Subsequently, the precursor amount for the shell is calculated according to the core diameter, crystal structure of shell material and core QDs concentration based on the spherical model. By controlling each monolayer thickness of the shell, certain thickness of the shell can be precisely controlled by the monolayers grown. Once the shell is thick enough, the size distribution will collapse due to unfavorable ripening and cation exchange events.

1.6 Quantum dots for PEC hydrogen generation

PEC hydrogen generation is an efficient approach to obtain H₂ fuels in a relatively low-cost, efficient and green way.⁶¹⁻⁶⁴ When compared to electrolytic water splitting, part of electrical energy can be saved by using solar energy. With the comparison of photochemical water splitting, the solar-to-hydrogen conversion efficiency is much higher. Thus, PEC H₂ generation is an intermediate way to obtain H₂. Since Fujishima and Honda first discovered a PEC cell based on TiO₂, numerous works have been investigated on different semiconductor materials as the PEC electrodes.

Colloidal QDs are quite attractive to play as the light harvester for many optoelectronic devices,

such as solar cell^{36,65-69}, solar concentrators⁷⁰⁻⁷⁵ and solar-driven PEC H₂ generation cell^{31,32,34,37,43}. It can address the issue of limited light absorption range of metal oxide semiconductors, such as TiO₂⁷⁶⁻⁷⁸, SnO₂⁷⁹⁻⁸¹, ZnO⁸²⁻⁸⁴. Recent decades, QDs were applied as the sensitizers of metal oxide for PEC H₂ generation, forming QDs/metal oxide heterostructures. Moreover, the QDs/metal oxide heterostructures can also provide the possibility to tune the band alignment between two semiconductors.⁸⁵

In this thesis, I used TiO₂ as the QDs matrix which is the most used metal oxide semiconductor for PEC H₂ generation following pioneer works. Typically, to obtain the QDs/TiO₂ heterostructures, electrophoretic deposition (EPD) method was used to combine QDs with mesoporous TiO₂ films. Moreover, to eliminate the impact during the EPD process, all the parameters of EPD in this thesis were kept the same, following the optimized parameters in the literatures.^{86,87} The time of EPD process was kept for 2 hours and the voltage was set at 200 V.

For the PEC and stability measurements, the details are described in Experiment part.

1.7 Thesis objectives and contributions of this work

There are many literatures reporting solar-driven PEC H₂ generation cells based on colloidal QDs, such as CdSe/CdS^{32,88}, CdS/CdSe^{89,90}, PbS/CdS^{34,91,92}, CuInSeS/ZnS^{37,93,94}. Up-to-date, the CdSe/CdS core/shell architecture is still one of the most efficient architectures for optoelectronic devices, thanks to its favorable band alignment for efficient carrier transfer as well as absorption range well matching with the visible range of the solar spectrum. Moreover, few lattice mismatch (~3.9 %) between CdSe and CdS two semiconductors also play an important role for high solar to electricity or solar to fuels conversion efficiency. However, all these mentioned previous works were all concentrating on engineering the shell thickness for the optimization of the core/shell band alignment and accordingly final conversion efficiency based on CdSe/CdS core/shell QDs. There are few works concentrating on the core size of QDs and accordingly core/shell band alignment between the core and shell. Thus, motivating by this, in the first work, I synthesized four types of CdSe/CdS core/shell QDs with different CdSe core size (2.8-4.8 nm) and maintained similar shell thickness (~2 nm). Then I investigated the band

structure of as-synthesized QDs and the PEC performance based on these QDs.

In my second work, I gave more focus on the shell composition of CdS shells and their application for PEC performance. There were some works reporting the optimization of the shell composition via band engineering approach for improvement of the optoelectronic properties of QDs. However, there are few works reporting alloyed core/shell QDs for PEC H₂ generation. Moreover, based on equal ratio of Se and S in alloyed shells, I further engineered the shell composition into the gradient shells for the PEC H₂ generation which is the first-time reported.

In the third work, I investigated the properties of CdSe/CdS/ZnS core/multiple shell QD and its application for PEC H₂ generation. Due to the poor stability performance of the photoanode based on CdSe/CdS QDs. I used ZnS shells with wide bandgap to further passivate the surface of QDs. Subsequently, I added CdSe_xS_{1-x} and Cd_yZn_{1-y}S double alloyed shells to build a more favorable band alignment for more efficient carrier transfer compared to pure-shell QDs. In this work, I also investigated the properties of QDs with different ZnS shell thickness and the accordingly PEC performance.

In my thesis, I tried to use band engineering approach to adjust the band alignment between the core and shell. Typically, I optimized the core size of CdSe, shell thickness of the CdS and ZnS, the composition of the shell (also called alloyed shell) to build a more favorable band alignment for improvement of PEC and stability performance of the photoanodes.

1.8 Thesis organization

The thesis is divided into 6 parts and organized as follows:

Chapter 1 introduces the topics, outline and motivation of this work.

Chapter 2 describes the synthesis method and process of the CdSe, CdSe/CdS, CdSe/CdSe_xS_{1-x}/CdS, CdSe/CdS/ZnS QDs. Characterization details are also shown in Chapter 2.

Chapter 3 discusses the synthesis of four types of core/shell CdSe/CdS QDs with different core

size and same shell thickness. Subsequently, four QDs are applied for the PEC H₂ generation. Their optical and carrier dynamic properties are investigated based on the PEC performance.

Chapter 4 presents the synthesis of two types of CdSe/CdSe_xS_{1-x}/CdS alloyed core/shell QDs. By comparing the different shell composition, the PEC performance and their optical and electrochemical properties are discussed in this chapter.

K. Wang, X. Tong, Y. Zhou, H. Zhang, F. Navarro-Pardo, G. S. Selopal, G. Liu, J. Tang, Y. Wang, S. Sun, D. Ma, Z. M. Wang, F. Vidal, H. Zhao, X. Sun and F. Rosei, Efficient solar-driven hydrogen generation using colloidal heterostructured quantum dots. Journal of Materials Chemistry A, 2019, 7, 14079-14088.

Chapter 5 describes the synthesis of CdSe/CdS/ZnS, CdSe/CdSe_xS_{1-x}/CdS/Cd_yZn_{1-y}S/ZnS core/multiple shell QDs and their PEC and stability performance. The stability performance is optimized through the ZnS shell coating and the carrier dynamics are discussed in this chapter.

K. Wang, Y. Tao, Z. Tang, D. Benetti, F. Vidal, H. Zhao, F. Rosei and X. Sun, Heterostructured core/gradient multi-shell quantum dots for high performance and durable photoelectrochemical hydrogen generation. Nano Energy, 2022, 100, 107524.

Chapter 6 briefly summarizes important contributions of this work and states future challenges in this field.

Most of the work in this thesis was done by myself, Kanghong Wang, however, some parts were carried out through collaboration. More specifically, theoretical calculations of electron/hole wavefunctions were performed by Prof. François Vidal, INRS-EMT center. In the theoretical calculation part, Kanghong Wang I only participated in developing the model and discussing the results. I did not conduct the simulations. Following the main body of thesis is an appendix providing a summary of this thesis in French as per INRS requirements.

Chapter 2 Experimental

In this chapter, I introduced the synthesis and characterizations of the CdSe QDs via hot-injection approach. Subsequently, the synthesis and characterizations of CdSe/CdS core/shell QDs are discussed through SILAR method. Then I replaced the CdS pure shell with CdSe_xS_{1-x} alloyed shell, forming CdSe/CdSe_xS_{1-x}/CdS core/shell QDs. Furthermore, I synthesized the CdSe/CdS/ZnS, CdSe/CdSe_xS_{1-x}/CdS/Cd_yZn_{1-y}S/ZnS core/multiple shell QDs. All the QDs were applied with mesoporous TiO₂ for the solar-driven PEC H₂ generation and the PEC performance and stability performance are investigated.

2.1 Materials

Cadmium oxide (CdO) (99 %), OA, OLA, sulfur powder (S) (99.99 %), ODE, selenium shot (Se) (99.999 %), trioctyl phosphine oxide (TOPO), trioctyl phosphine (TOP) (90 %), zinc acetate dihydrate (98 %), sodium sulfide nonahydrate (99.9 %), sodium sulfide (Na₂S), sodium sulfite (Na₂SO₃), zinc oxide (ZnO) (90 %), toluene, methanol, acetone, ethanol and isopropanol (IPA) were obtained from Sigma-Aldrich Inc and Macklin Inc. Ti-nanoxide BL/SC was purchased from Solaronix. Titania paste (code 18NR-AO) consisting of a blend of active anatase particles (20 nm in diameter) and larger anatase scattering particles (up to 450 nm in diameter) was supplied by Dyesol (Queanbeyan, Australia). Fluorine doped tin oxide (FTO) coated glass substrates with a sheet resistance of 10 U per square were purchased from Pilkington glasses. All chemicals were used as received.

2.2 Reaction setup

QDs are very sensitive to oxygen and moisture. Thus, the entire reaction which includes the nucleation and growth process is under the protection of nitrogen (N₂) flow. With the presence of oxygen (or water), the QDs will be oxidized, leading to poor photostability. Therefore, I set up the reaction in an air-free system, as schematically shown in Figure 2.1. The oxygen can be removed by vacuum pumping and nitrogen purging, and nitrogen flux can further protect the entire chemical reaction from the air. In the following, all the QDs were synthesized by using

this reaction setup. And as shown in the image, the cation precursor (Cd) is placed in the cell while the anion precursor (Se) is injected from the feeding spot through syringe. The middle tunnel is the condensing unit connecting to a vacuum pump while the left tunnel is placed a thermometer for controlling the cell temperature all over the process.

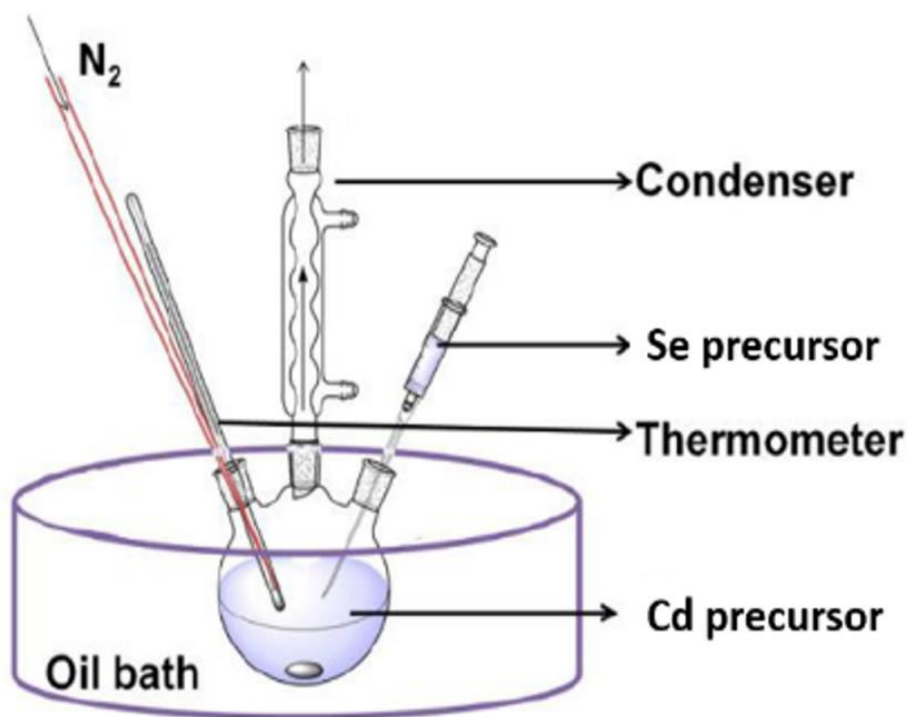


Figure 2.1 Schematic illustration of the air-free reaction setup for synthesizing CdSe QDs. The image demonstrates the hot-injection approach by separating the cation precursors and anion precursors in a three-necked bottle.

2.3 Synthesis

2.3.1 Synthesis of CdSe QDs

Typically, the CdSe QDs are synthesized by hot-injection approach following the literatures which separates the anion and cation precursors. The reaction is allowed under high temperature which is up to 300 °C. The procedures are described as follows:

1. Firstly, TOPO (1 g) and Cd-oleate (0.38 mmol, 1 mL) in 8 mL of ODE were purged

with N₂ at room temperature for 30 min. The reaction system was evacuated for 1 hour at room temperature and another 30 min at 100 °C.

2. Then the temperature was raised to 300 °C. The solution will turn to transparent and the prepared mixture of TOP-Se (4 mmol, 4 mL), 3 mL of OLA, and 1 mL of ODE at room temperature was quickly injected into the Cd-oleate suspension under vigorous stirring.
3. The reaction cell was kept under 260 °C for different time for forming CdSe QDs with different sizes and then quenched with cold water to stop the reaction.
4. Finally, ethanol (~20 mL) was added to the suspension. After centrifuge, the supernatant was removed for several times and finally the QDs were dispersed and stored in toluene.

To precisely control the CdSe QDs size, I kept the same reaction temperature (300 °C) and growth temperature (260 °C), but adjusting the growth time (from 2 min to 10 min). The synthesis process can produce the CdSe QDs with excitonic absorption wavelength covering from 530 nm to 610 nm by varying the reaction time. The CdSe core size varies from 2.8 nm to 4.8 nm in diameter.

2.3.2 Synthesis of CdSe/CdS core/shell QDs

Recent years, many study have revealed that overcoating a shell on the surface of core QDs can improve the QY of QDs as well as their photostability. The method of coating shell material is called SILAR. Herein, Figure 2.2 shows the synthesis of CdSe/CdS core/shell QDs through SILAR method. Generally, the overall size will increase with more SILAR cycles while the core keeping the same size. There is another method called cation exchange while the overall size is same with replacement of the core materials. Herein, I used SILAR method to grow shell materials on the core surface in my thesis due to the precise control of shell thickness and composition.

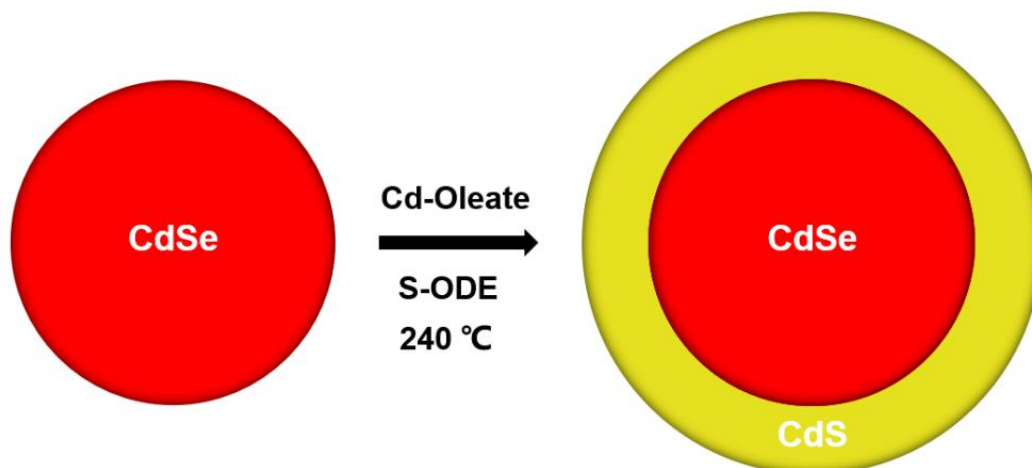


Figure 2.2 Schematic diagram of successive ion layer adsorption and reaction method for synthesizing the CdSe/CdS core/shell QDs with the deposition on CdSe QDs' surface.

The SILAR procedure was carried out under N_2 atmosphere. All solvents used in the procedure are anhydrous and oxygen free. The procedure is as follows:

1. Typically, in a 50 mL round-bottom flask, OLA (5 mL), ODE (5 mL) and CdSe QDs ($\sim 2 \times 10^{-7}$ mol in toluene) were degassed at 110 °C for 30 min. The reaction flask was re-stored with N_2 and the temperature was further raised to 240 °C with stirring.
2. The $Cd(OA)_2$ dispersed in ODE (0.2 M) was added dropwise slowly and the mixture was allowed to react for 2.5 hours, followed by dropwise addition of 0.2 M S-ODE with the same volume. Then the shell was further annealed for 10 min. All subsequent shells were annealed at 240 °C for 10 min following the injection of S-ODE and 2.5 hours following dropwise addition of $Cd(OA)_2$. Six times of anion/cation precursors were added, forming 6 monolayers of CdS shell.
3. Alcohol was added in the suspension and the supernatant was removed after centrifuging for several times. The final QDs were re-dispersed in toluene.

The shell thickness can be precisely controlled by designing the SILAR cycles and the injected precursor volume. After 6 cycles of SILAR, relatively similar shell thickness (~ 2 nm) of CdS was grown on the CdSe core with different core sizes. The excitonic absorption wavelength of the CdSe/CdS core/shell QDs varies from 585 nm to 635 nm.

2.3.2 Synthesis of CdSe/CdSe_xS_{1-x}/CdS alloyed QDs

To synthesize CdSe/CdSe_xS_{1-x}/CdS alloyed QDs, the pure CdS shell was replaced with alloyed shell. The procedure of alloyed shell growth is similar to the growth of CdS pure shell, the details are shown as follows:

1. Firstly, in a 50 mL round-bottom flask, OLA (5 mL), ODE (5 mL) and CdSe QDs ($\sim 2 \times 10^{-7}$ mol in toluene) were degassed at 110 °C for 30 min. The reaction flask was re-stored with N₂ and the temperature was further raised to 240 °C with stirring.
2. The Cd(OA)₂ dispersed in ODE (0.2 M) was added dropwise slowly and the mixture was allowed to react for 2.5 hours, followed by dropwise addition of 0.2 M Se/S-ODE with the same volume (Se/S ratio is depending on the designing structure of the alloyed shell). Then the shell was further annealed for 10 min. All subsequent shells were annealed at 240 °C for 10 min following the injection of S-ODE and 2.5 hours following dropwise addition of Cd(OA)₂. Six times of anion/cation precursors were added, forming 6 monolayers of CdSe_xS_{1-x} alloyed shell. For the growth of alloyed QDs with gradient band structures, the feeding ratio of Se/S is changing in each monolayer. To be more specific, the ratio of Se/S is 9/1, 8/2, 7/3, 5/5, 3/7, 0/10 in each SILAR cycles.
3. Finally, alcohol was added and then the suspension was centrifuged and supernatant was removed. QDs were re-dispersed in toluene.

The process of growing the alloyed shell is similar to the pure CdS shell. By adjusting the cation precursors (Se/S), the structure of the shell can be tuned into CdSe_xS_{1-x} with different Se/S ratio (x varies from 0 to 1). Here, I designed two alloyed QDs with different shell composition, CdSe/CdSe_{0.5}S_{0.5}/CdS and CdSe/CdSe_xS_{1-x}/CdS while x changes with each single layer.

2.3.3 Synthesis of CdSe/CdS/ZnS core/multiple shell QDs

Recently, many studies revealed that core/multiple shell QDs can be a promising candidate for the optoelectronic device due to their superior optical properties. The QY can be improved with multiple-shell coating, leading to less radiative recombination. Furthermore, the band alignment

can be tuned by proper material selection, leading to better carrier separation and transfer efficiency. The coating of multiple shells can also through SILAR method. The procedure is described as follows:

1. The CdS shell coating is same with the synthesizing CdSe/CdS core/shell QDs. Typically, in a 50 mL round-bottom flask, OLA (5 mL), ODE (5 mL) and CdSe QDs ($\sim 2 \times 10^{-7}$ mol in toluene) were degassed at 110 °C for 30 min. The reaction flask was re-stored with N₂ and the temperature was further raised to 240 °C with stirring.
2. The Cd(OA)₂ dispersed in ODE (0.2 M) was added dropwise slowly and the mixture was allowed to react for 2.5 hours, followed by dropwise addition of 0.2 M S-ODE with the same volume. Then the shell was further annealed for 10 min. All subsequent shells were annealed at 240 °C for 10 min following the injection of sulfur and 2.5 hours following dropwise addition of Cd(OA)₂. Four SILAR cycles were used to form 4 monolayers of CdS shell.
3. For the growth of ZnS shell through SILAR, minor modification was conducted. After the growth of CdS shell, the temperature of the reaction cell was dropped down to 220 °C. Then the prepared Zn(OA)₂ dispersed in ODE (0.2 M) was added dropwise slowly and the mixture was allowed to react for 10 min, followed by dropwise addition of 0.2 M S-ODE with the same volume. Then the shell was further annealed for 10 min. In short, with the interval of 10 min, anion/cation precursors were injected into the cell, annealing another 10 min. The reaction cell was kept under 220 °C all the time.
4. Alcohol was added and then the suspension was centrifuged and supernatant was removed. QDs were re-dispersed in toluene.

2.3.4 Synthesis of CdSe/CdSe_xS_{1-x}/CdS/Cd_yZn_{1-y}S/ZnS core/multiple shell QDs

The CdSe/CdSe_xS_{1-x}/CdS/Cd_yZn_{1-y}S/ZnS core/multiple shell QDs were synthesized according to the synthesis process of CdSe/CdS/ZnS core/multiple shell QDs with minor modification. When I grew CdSe_xS_{1-x} alloyed shells, the Se/S-ODE was injected as the replacement of S-ODE at 240 °C. When I grew Cd_yZn_{1-y}S alloyed shells, the precursors were injected with Cd/Zn(OA)₂ at 240 °C. After the shell growth, the QDs were purified several times and re-

dispersed in toluene.

2.4 Characterizations of QDs

2.4.1 Structure characterizations

Transmission electron spectroscopy (TEM), high-resolution TEM (HRTEM) and selected area electron diffraction (SAED) of the QDs and QD-sensitized TiO₂ film were performed by using a JEOL 2100F TEM. A JEOL JSM7401F field emission scanning electron microscope (FE-SEM) equipped with an energy-dispersive X-ray spectrometer (EDS) was used for obtaining the elemental composition within the QD-sensitized TiO₂ film. Samples of TEM measurements were deposited onto copper TEM grids coated with thin (5-50 nm thickness) carbon films. One drop of QDs dispersed in toluene was placed on the grid. The grid was allowed to dry in air.

Small angle X-ray diffraction (XRD) of extensively purified QDs was carried out with a Philips X'pert diffractometer using a Cu K α radiation source ($\lambda = 0.15418$ nm). Nanocrystals were placed on glass for measurements. Diffraction patterns were collected in the 2θ range 20°-80°, by using the step of 0.1° and counting time of 10 seconds.

X-ray photoelectron spectroscopy (XPS) was performed using a VG Escalab 220i-XL equipped with a hemispherical analyzer, applying a twin anode X-ray source. The C 1s peak (BE = 284.8 eV) was used as an internal reference to rule out charging effects. The spectra were treated using Casa XPS software.

The size of QDs was measured by TEM with good precision. About 100 QDs were analyzed for each sample; the size distribution was analyzed with a Gaussian distribution.

The band gap energy was calculated from the absorption peak following the equation:

$$E = hc/\lambda \quad (2.1)$$

Where E is band gap energy, h is Planck constant and λ is the first exciton absorption peak

position.

2.4.2 Property characterization

The UV-vis absorption spectra were recorded with a Cary 5000 UV-vis-NIR spectrophotometer (Varian) with a scan rate of 600 nm min⁻¹. Fluorescence spectra were recorded with a Fluorolog-3 system (Horiba Jobin Yvon). The PL lifetime of the QDs was measured in the time-correlated single-photon counting (TCSPC) mode with a 450 nm laser. The decay signals were found to be best fitted to a three-exponential function, according to the following equation:

$$\langle \tau \rangle = \frac{a_1\tau_1^2 + a_2\tau_2^2 + a_3\tau_3^2}{a_1\tau_1 + a_2\tau_2 + a_3\tau_3} \quad (2.2)$$

Where τ_1 , τ_2 and τ_3 are lifetime of the first, second and third process, respectively. a_1 , a_2 and a_3 are ratio constant according to each lifetime.

The theoretical simulation (wave functions of the carriers in QDs) was calculated by solving the stationary Schrödinger equation with a model of spherical geometry. Here are the bulk values for the effective masses of electrons [$m(\text{electron})^\#$] and holes [$m(\text{hole})^\#$]. For CdSe, $m(\text{electron})^\# = 0.13 m(\text{electron})$ and $m(\text{hole})^\# = 0.45 m(\text{hole})$. For CdS, $m(\text{electron})^\# = 0.21 m(\text{electron})$ and $m(\text{hole})^\# = 0.68 m(\text{hole})$. While for ZnS, $m(\text{electron})^\# = 0.28 m(\text{electron})$ and $m(\text{hole})^\# = 0.49 m(\text{hole})$ where $m(\text{electron})$ ($m(\text{hole})$) is the electron ($m(\text{hole})$) mass in vacuum. The potentials for holes and electrons as a function of position were approximated as the highest occupied molecular orbital (HOMO) levels and the lowest unoccupied molecular orbital (LUMO), respectively. These levels are -3.71 and -5.81 eV for CdSe, -3.3 and -5.8 eV for CdS and -2.5 eV and -6.1 eV for ZnS, respectively. The potentials in the outer range of the QDs were set as -9.8 eV and 0 V for holes and electrons, respectively.

2.5 Fabrication of the photoanode

Firstly, FTO glass substrates were cleaned with Triton, and then with a mixture of methanol, acetone, and IPA (1:1:2), thoroughly rinsed with deionized (DI) water and dried in a N₂ flow. A thin and compact TiO₂ layer was spin coated on FTO glass substrates at 6000 r.p.m. for 30 s by

using the solution Ti-Nanoxide BL/SC (Solaronix), followed by annealing in air at 500 °C for 30 min and then cooling to room temperature. Subsequently a commercial TiO₂ paste, a blend of small anatase particles (20 nm in diameter) and larger anatase particles (up to 450 nm in diameter) paste (18NR-AO), was deposited on top of the compact TiO₂ layer by tape casting and dried in air for 20 min. The photoanodes were then heated on a hotplate at 120 °C for 6 min. After the photoanode cooling down to room temperature, a second layer of 18NR-AO paste was then deposited on the top, following the same procedure. All the thicknesses of the photoanodes were measured by using a profilometer and also measured by SEM cross-section images.

Subsequently, the as-prepared TiO₂ films on FTO substrates were vertically immersed in a QD dispersion in such a way that the deposited films faced to each other. The distance between them was adjusted to be around 1 cm and a direct current (DC) bias of 200 V was applied for 120 min. To wash off unabsorbed QDs after the EPD process, the samples were rinsed several times with toluene and dried with N₂ flow at room temperature.

Prior to ZnS capping, ligand exchange was applied by using two SILAR cycles of methanolic solution cetyl-trimethyl ammonium bromide (CTAB) and toluene for 1 min dipping. The CTAB treated anode was further washed by methanol to remove the chemical residuals on the surface and then dried with N₂ flow. Finally, one-minute dipping in toluene and dried with N₂ flow for each SILAR cycle.

The ZnS capping layer was grown using the SILAR process as follows. In a typical SILAR deposition cycle, Zn²⁺ ions were deposited from a methanolic 0.1 M solution of Zn(OA)₂. The sulfide precursor was 0.1 M solution of Na₂S in a mixture of methanol/water (1/1 v/v). A single SILAR cycle consisted of 1 min dip-coating of the TiO₂ working electrode in the cation precursors (Zn²⁺) and subsequently in the anion solutions (S²⁻). After each bath, the photoanode was thoroughly rinsed by immersing it in the corresponding solvent (methanol or mixed solution), respectively, to remove the chemical residuals on the surface and then dried with a N₂ gun. Two SILAR cycles were applied to form the capping ZnS layers.

2.6 PEC and stability measurement

The PEC performance of the photoelectrodes was evaluated in a typical three-electrode configuration, consisting of a QD-TiO₂ thick film working electrode, a Pt counter electrode, and a saturated Ag/AgCl reference electrode. A Cu wire was used to connect FTO with the outer circuit. Insulating epoxy resin was used to cover the sample's surface except for the active area (~0.12 cm²), to avoid any direct contact between the electrolyte and the conducting back-contact and/or the connecting wire. Subsequently the sample was fully immersed in the electrolyte containing 0.25 M Na₂S and 0.35 M Na₂SO₃ (pH~13) as sacrificial hole scavenger. All potentials, measured with respect to the reference electrode of Ag/AgCl during the PEC measurements, were converted to the reversible hydrogen electrode (RHE) scale according to the following equation:

$$V_{\text{RHE}} = V_{\text{Ag/AgCl}} + 0.197 + \text{pH} \times (0.059) \quad (2.3)$$

The photo response was measured by using a 150 W Xenon lamp as light source with an AM 1.5 G filter. The sample was placed at a distance of 20 cm from the lamp. Prior to each measurement, the light intensity was monitored using a thermopile and adjusted to 100 mW/cm². All the current versus potential measurements were carried out at a 20 mV/s sweep rate. All the PEC results are measured several times until the average values are achieved.

The wavelength-dependent incident photon-to-photocurrent efficiency (IPCE) was calculated according to the following equation:

$$IPCE(\%) = \frac{1240 J}{\lambda \times I} \times 100\% \quad (2.4)$$

Where J represents the photocurrent density (mA/cm²), λ is the wavelength of incident light (nm), and I is the intensity of the incident light (mW/cm²).

Chapter 3 CdSe/CdS QDs for PEC H₂ generation

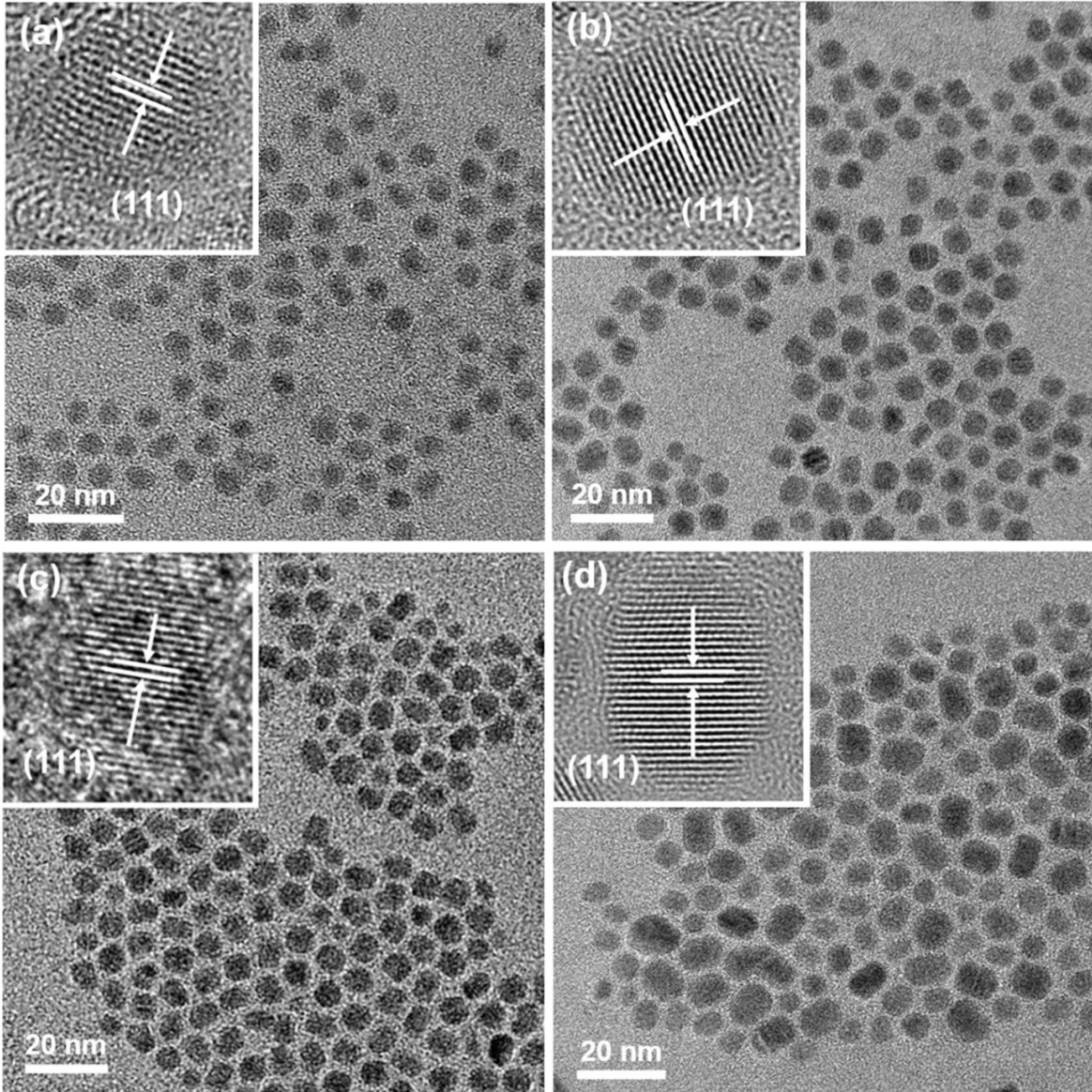
As discussed above, CdSe/CdS is still one of the most efficient core/shell architectures for optoelectronic devices. However, pioneer works investigated a lot on the CdS shell thickness for optimized performance based on such structures. Few works explored the effect of core size of CdSe. As known, the absorption range as well as the band gap/edges of the CdSe NCs will be dramatically affected with the size difference. Moreover, the carrier transfer efficiency from core to the shell will also be impacted due to the band alignment between core and shell with different core size.^{95,96} In this chapter, I will discuss the synthesis of four CdSe/CdS core/shell QDs with different core size (2.8-4.8 nm) and similar shell thickness (~2 nm). The core/shell QDs are denoted as CdSe (2.8 nm)/CdS QDs, CdSe (3.1 nm)/CdS QDs, CdSe (3.5 nm)/CdS QDs and CdSe (4.8 nm)/CdS QDs, respectively. Furthermore, four QDs were applied to sensitize mesoporous TiO₂ for PEC H₂ generation. Finally, the carrier dynamic behavior will be investigated in core/shell architectures with different core size. By increasing the CdSe core size, the absorption range will be broadened while the carrier transfer efficiency will be affected due to narrower bandgap of CdSe. This work is aiming to discover the relation between PEC performance with different parameters, such as absorption range and carrier transfer efficiency.

3.1 Characterization of QDs

The CdSe/CdS QDs were synthesized through hot-injection approach and SILAR method.^{15,33} The core size is kept by controlling the growth time from 2 min to 10 min. Afterwards, the reaction was quenched by cold water to stop the reaction instantly. The CdS shell was grown on the surface of CdSe core via SILAR method. The equivalent volume of Cd and S precursors were slowly injected into the cell in sequence. The reaction time was kept under 240 °C while the growth time was kept for 2.5 hours for Cd(OA)₂ and 10 min for S-ODE. Same steps were conducted for 6 times, growing same monolayers of the CdS shell. After several times of purification, the QDs were dispersed in toluene for characterizations.

3.1.1 Structure of QDs

The morphological characterization was first shown in TEM images. In Figure 3.1, the TEM images showed that QDs were distributed uniformly for four types of CdSe/CdS core/shell QDs while the overall size increases with larger core size of QDs. In Figure 3.1(e), the size distribution of four core/shell QDs were shown while the values are shown in Table 3.1. According to the figure and table, the size is 2.8 ± 0.2 , 3.1 ± 0.2 , 3.5 ± 0.3 and 4.8 ± 0.3 nm in diameter for four CdSe core QDs which is consistent with growth time. And after the CdS shell growth, the size increased up to 6.6 ± 0.6 , 7.1 ± 0.7 , 7.5 ± 0.7 and 8.9 ± 1.2 nm in diameter which the corresponding shell thickness is 2 ± 0.1 nm. Such results confirmed that the as-synthesized CdSe/CdS core/shell QDs were only tuned with core size but with similar shell thickness. The insets in the Figure 3.1 (a)-(d) displayed that the QDs all have the high crystallization in the HR-TEM images and (111) planes are shown in four insets which correspond to zinc blende (ZB) crystal structure of CdS.³²



(e)

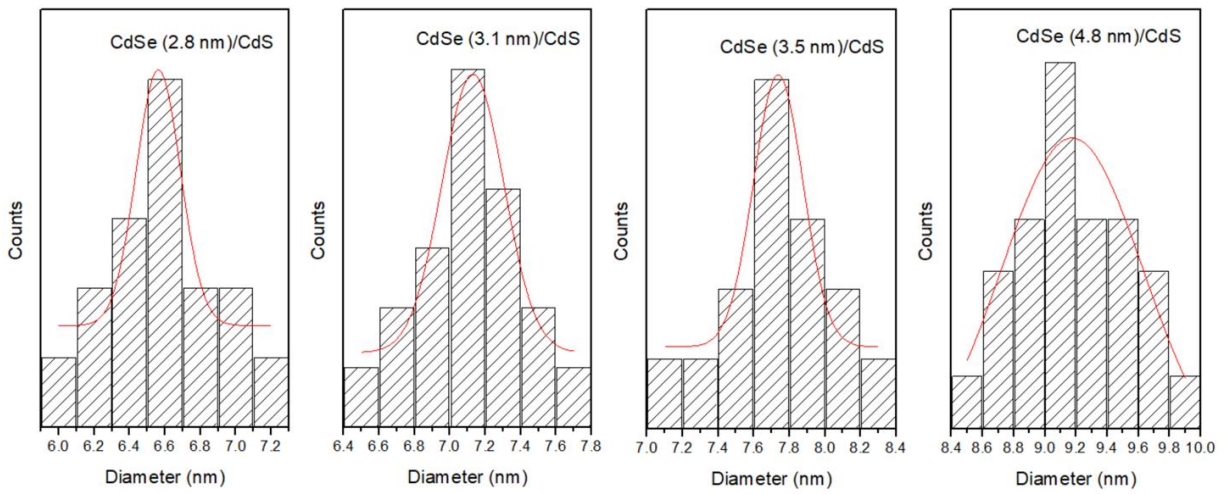


Figure 3.1 TEM images of (a) CdSe (2.8 nm)/CdS QDs, (b) CdSe (3.1 nm)/CdS QDs, (c) CdSe (3.5 nm)/CdS QDs, (d) CdSe (4.8 nm)/CdS QDs (the insets show the HR-TEM images of corresponding QDs). (e) Size distribution of four types of CdSe/CdS core/shell QDs. The images indicate the increasing size of as-synthesized QDs.

Figure 3.2 showed the SAED pattern of four types of CdSe/CdS QDs which indicates that the lattice distance is corresponding to (111), (220), (103) and (311) planes of ZB CdS which has a good agreement with the HR-TEM results.

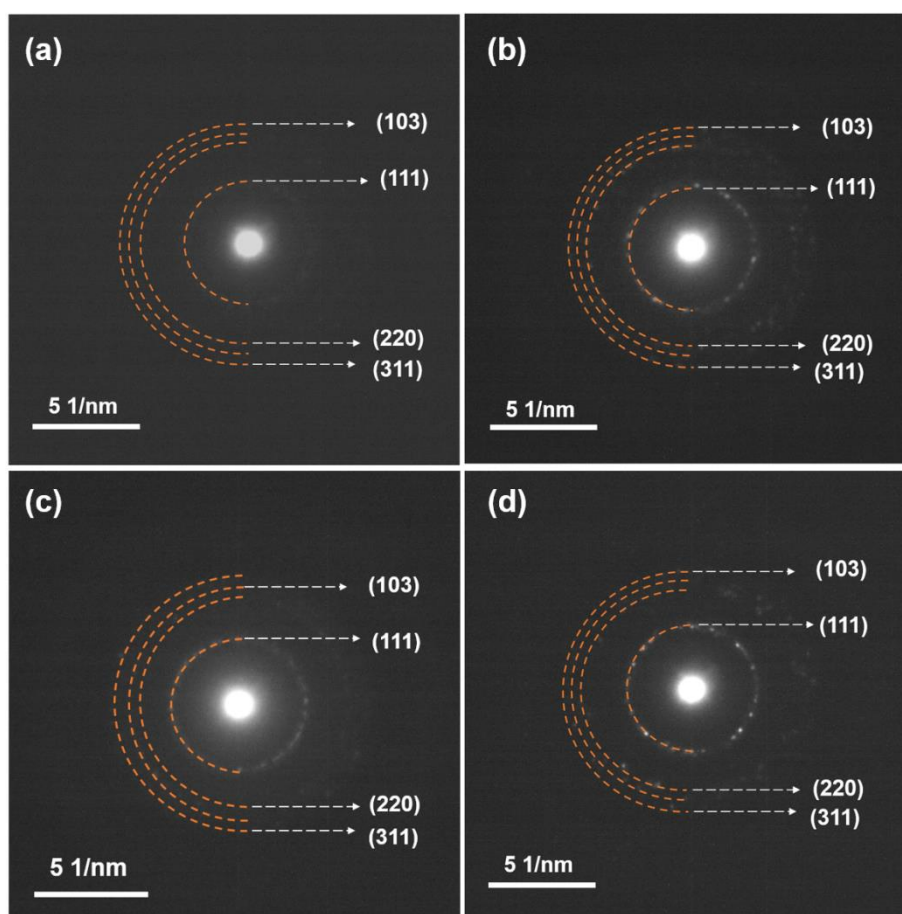


Figure 3.2 SAED pattern of (a) CdSe (2.8 nm)/CdS QDs, (b) CdSe (3.1 nm)/CdS QDs, (c) CdSe (3.5 nm)/CdS QDs, (d) CdSe (4.8 nm)/CdS QDs, respectively.

To further verify the structure of QDs, XRD pattern was carried out and shown in Figure 3.2. The XRD pattern reveals that the CdSe core has the wurtzite (WZ) crystal structure while the CdS shell has the ZB crystal structure for all four CdSe/CdS core/shell QDs which are consistent with the former results. According to the HR-TEM, SAED and XRD results, the

crystal structure of four types of CdSe/CdS core/shell QDs can be determined as the same structures. In other words, the different reaction time (2 min to 10 min) of four types of CdSe core QDs do not change the crystal structure of QDs.

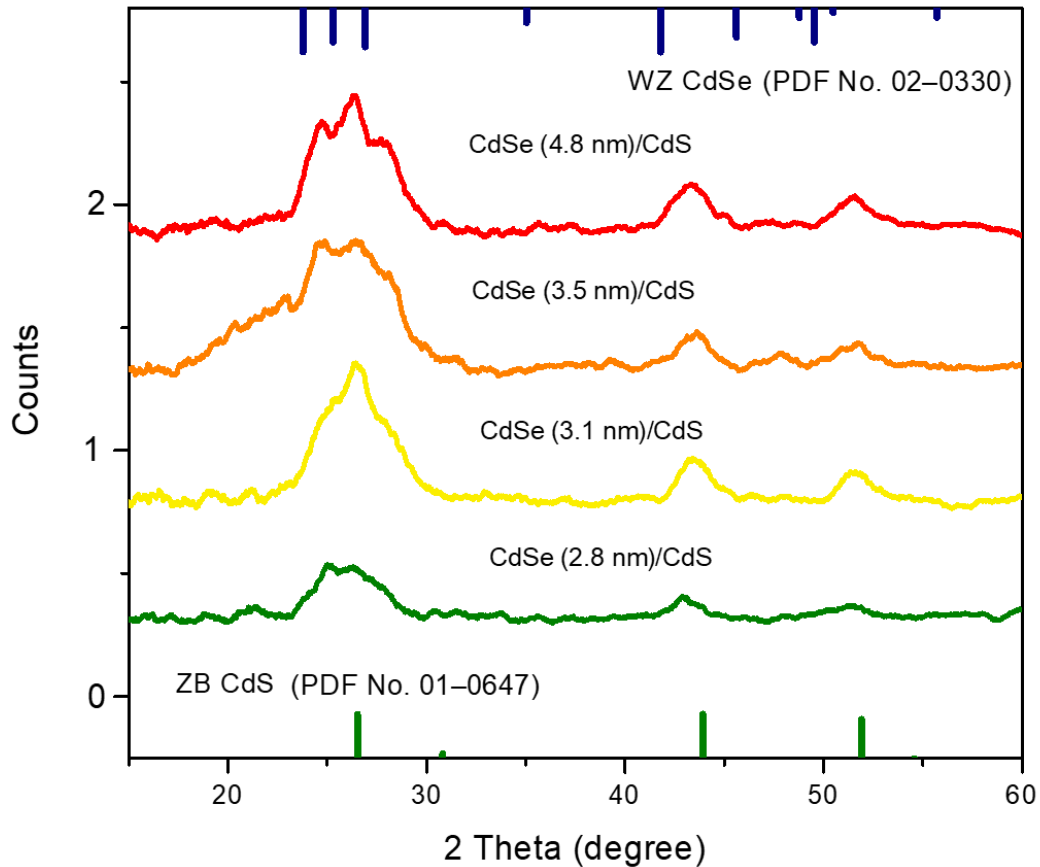


Figure 3.3 XRD pattern for CdSe (2.8 nm)/CdS QDs, CdSe (3.1 nm)/CdS QDs, CdSe (3.5 nm)/CdS QDs and CdSe (4.8 nm)/CdS QDs. JCPDS card (PDF No. 02-0330, PDF No. 01-0647) of WZ CdSe and ZB CdS are used for identification.

Then the four types of CdSe/CdS core/shell QDs were deposited into mesoporous TiO₂ film through EPD process. The cross-sectional SEM and EDS were further conducted, supporting the uniform dispersion of the four CdSe/CdS QDs inside the mesoporous TiO₂ films. Moreover, according to the Figure 3.4, the signal of element Ti, Cd, O, Se, S are captured which are consistent with CdSe/CdS core/shell QDs and mesoporous TiO₂ film based on QDs/TiO₂ photoanode. After the rough estimation, the thickness of the film is around 22 μm .

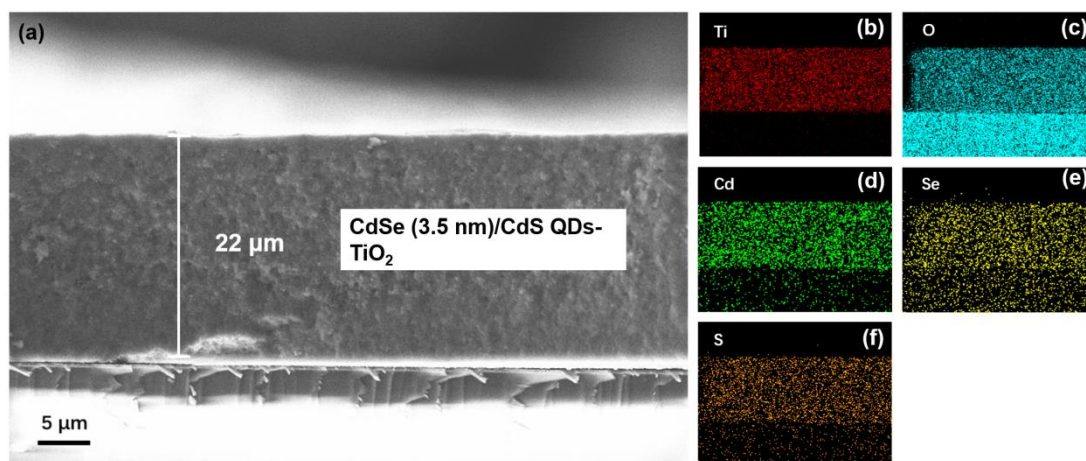


Figure 3.4 Cross-sectional SEM image and EDS mapping of CdSe (3.5 nm)/CdS QDs/TiO₂ (in the selected area surrounded by the white line): the elemental distributions of (b) Ti, (c) O, (d) Cd, (e) Se and (f) S. And the white arrow indicates the thickness is 22 μm of the film.

3.1.2 Optical properties of QDs

The optical properties of as-prepared QDs were further investigated by UV-vis absorption spectra and PL spectra. Firstly, the size of CdSe core QDs are decided by the empirical mathematical functions from the first-excitonic peak of UV-vis absorption spectra (details in Experiment section). Figure 3.5 (a) showed that the first-exciton absorption peak is located at 537 nm, 550 nm, 571 nm and 605 nm, respectively for four CdSe core QDs. After 6 cycles of CdS monolayers via SILAR method, the first-exciton absorption peak shown in Figure 3.5 (b) all red-shifted to 585 nm, 605 nm, 608 nm and 635 nm, respectively which indicated the successful epitaxy growth of CdS on the surface of CdSe.¹⁶

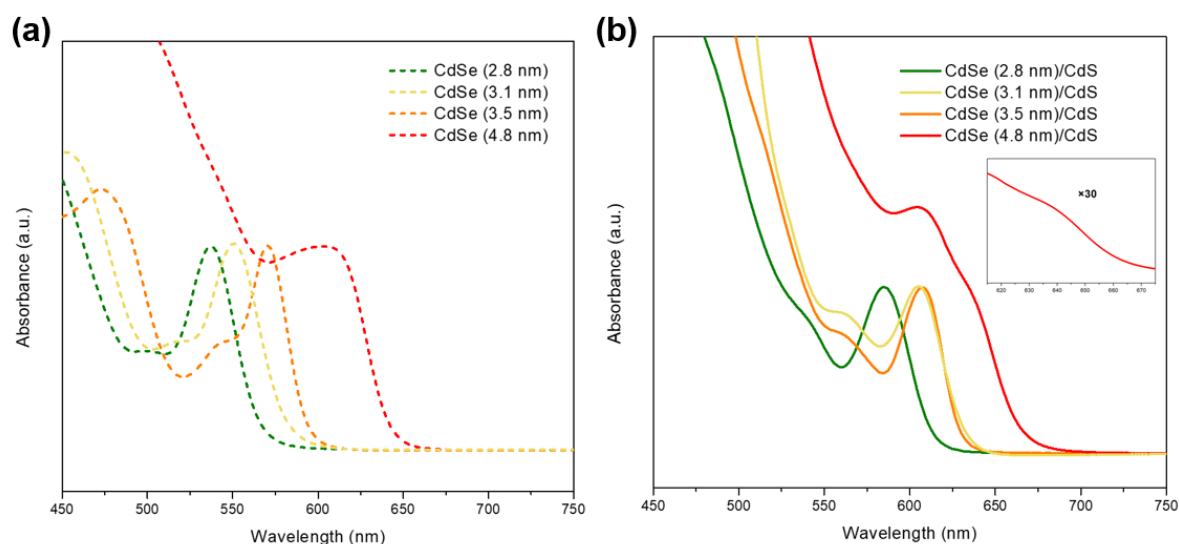


Figure 3.5 UV-vis absorption spectra of (a) CdSe (2.8 nm) QDs, CdSe (3.1 nm) QDs, CdSe (3.5 nm) QDs and CdSe (4.8 nm) QDs; (b) CdSe (2.8 nm)/CdS QDs, CdSe (3.1 nm)/CdS QDs, CdSe (3.5 nm)/CdS QDs and CdSe (4.8 nm)/CdS QDs.

According to Figure 3.6, the PL spectra showed the same phenomena. The PL peak of four CdSe core QDs are located at 552 nm, 566 nm, 580 nm and 621 nm, respectively while the PL peak of four core/shell QDs shifted to 595 nm, 615 nm, 618 nm and 648 nm, respectively. Such phenomena indicate the successful growth of CdS on the surface of CdSe core for four types of QDs due to the electron leakage to the shell regions. Moreover, the peaks position of four CdSe core and four CdSe/CdS QDs reflects the overall size of QDs.

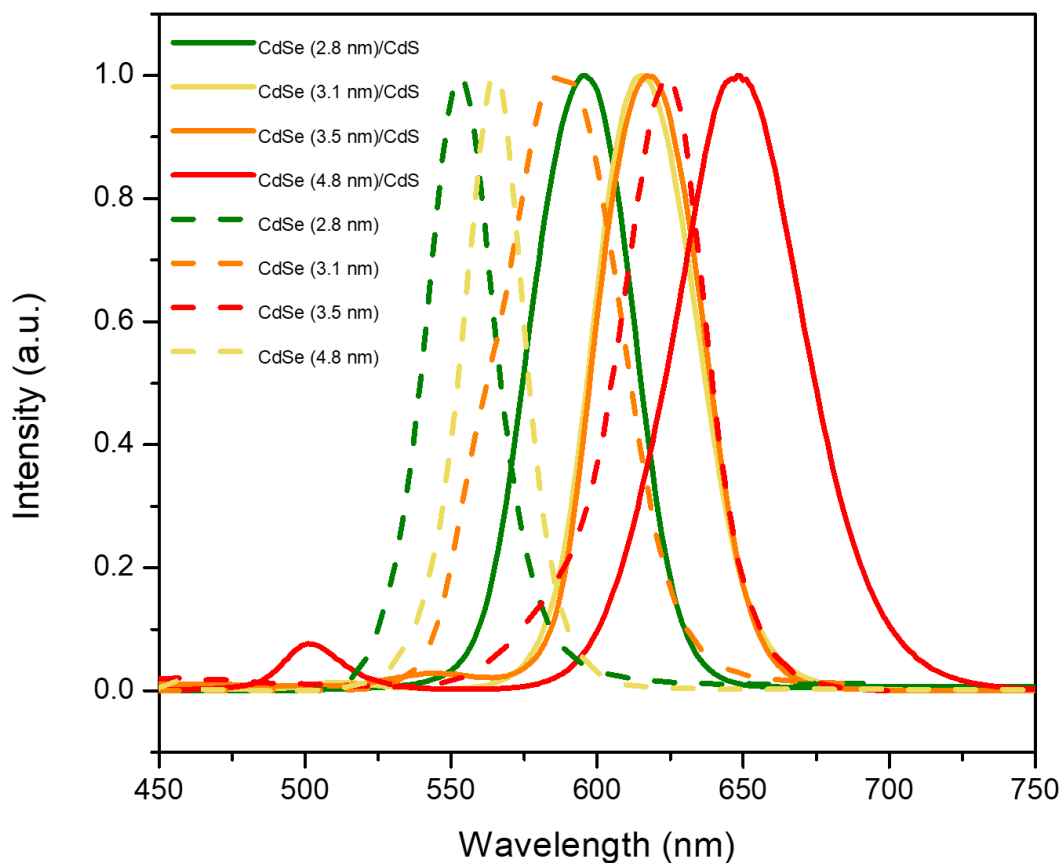


Figure 3.6 PL spectrum of four CdSe core QDs (CdSe (2.8 nm) QDs, CdSe (3.1 nm) QDs, CdSe (3.5 nm) QDs and CdSe (4.8 nm) QDs) and four CdSe/CdS core/shell QDs (CdSe (2.8 nm)/CdS QDs, CdSe (3.1 nm)/CdS QDs, CdSe (3.5 nm)/CdS QDs and CdSe (4.8 nm)/CdS QDs).

Table 3.1 Size and optoelectronic parameters of as-prepared QDs.

QDs	Diameter (nm)	Abs peak (nm)	PL peak (nm)
CdSe (2.8 nm)	2.8 ± 0.2	537	552
CdSe (3.1 nm)	3.1 ± 0.2	550	566
CdSe (3.5 nm)	3.5 ± 0.3	571	580
CdSe (4.8 nm)	4.8 ± 0.3	605	621

CdSe (2.8 nm)/CdS	6.6 ± 0.6	585	595
CdSe (3.1 nm)/CdS	7.1 ± 0.7	605	615
CdSe (3.5 nm)/CdS	7.7 ± 0.7	608	618
CdSe (4.8 nm)/CdS	8.9 ± 1.2	635	648

In Figure 3.7, it showed the CdSe core QDs with different size under sunlight and under UV light. It is interesting to find that the CdSe core QDs are tuning to different color (green, yellow, orange and red) under UV illumination. Also, the four types of CdSe/CdS core/shell QDs are all tuning to red which indicated the successful growth of CdS shell. As results, the PL spectra red-shifted to the longer wavelength.

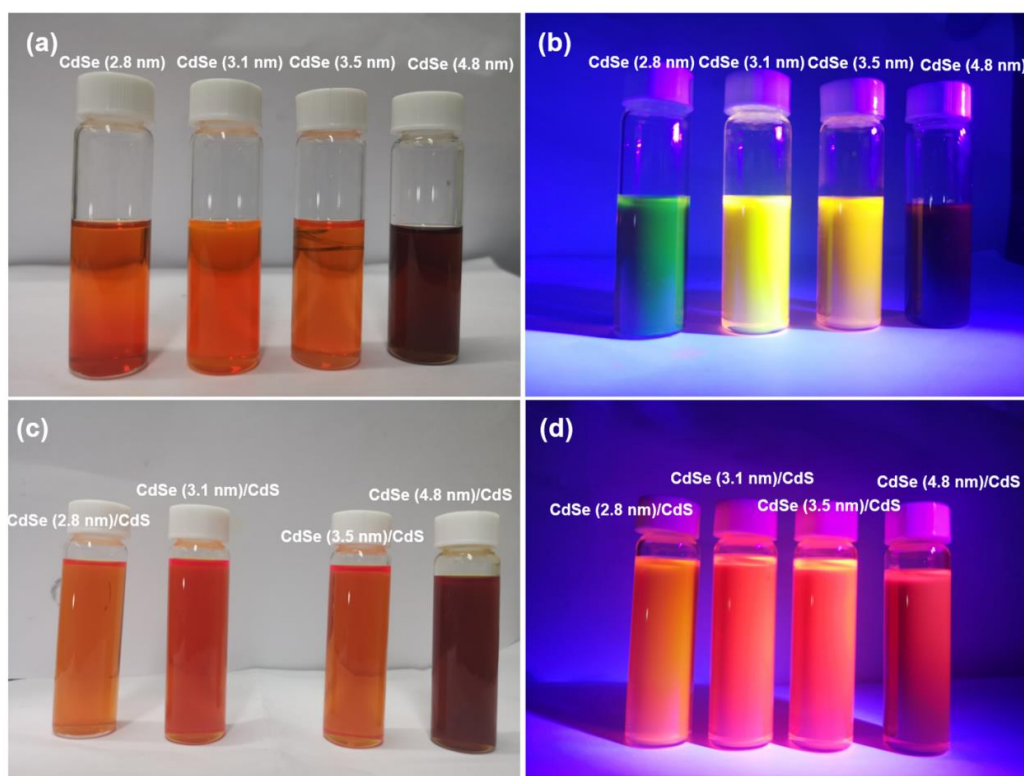


Figure 3.7 Images of four types of CdSe QDs (CdSe (2.8 nm) QDs, CdSe (3.1 nm) QDs, CdSe (3.5 nm) QDs and CdSe (4.8 nm) QDs) with different size (a) under sunlight (b) under UV light; Images of four types of CdSe QDs with different size (CdSe (2.8 nm)/CdS QDs, CdSe (3.1 nm)/CdS QDs, CdSe (3.5 nm)/CdS QDs and CdSe (4.8 nm)/CdS QDs) under (c) under sunlight (d) under UV light.

3.2 Carrier dynamic of QDs

To investigate the carrier dynamics behavior of four types of core/shell QDs, PL decay measurement was carried out with the transient fluorescence spectroscopy based on QDs with different substrates. As shown in Figure 3.8, the PL decay spectra indicated the average lifetime of QDs with TiO₂ (black curve), ZrO₂ (blue curve) and ZrO₂ in electrolyte (green curve). The average lifetime τ can be calculated through the following equation:

$$\langle \tau \rangle = \frac{a_1\tau_1^2 + a_2\tau_2^2 + a_3\tau_3^2}{a_1\tau_1 + a_2\tau_2 + a_3\tau_3} \quad (3.1)$$

The ZrO₂ was used as the benchmark where the electron injection from QDs to ZrO₂ does not occur due to the unfavorable band alignment. Thus, the PL degradation can all be attributed to the carrier recombination. Electron and hole transfer rate can be calculated according to the following equation:^{45,97,98}

$$K(et)/K(ht) = \frac{1}{\langle \tau \rangle_{QDs-TiO_2/ZrO_2} (electrolyte)} - \frac{1}{\langle \tau \rangle_{QDs-ZrO_2}} \quad (3.2)$$

Where K_{et} and K_{ht} are referring to the electron transfer rate and hole transfer rate, respectively. And $\langle \tau \rangle_{QDs-TiO_2}$ and $\langle \tau \rangle_{QDs-ZrO_2}$ are the average lifetime of QDs on the substrates of TiO₂ and ZrO₂ while the $\langle \tau \rangle_{QDs-ZrO_2} (electrolyte)$ represents the average lifetime of QDs-ZrO₂ immersed in the electrolyte. In such system, the energy transfer between QDs was ignored. All the lifetime values are shown in Table 3.2. The CdSe (2.8 nm)/CdS QDs with the smallest core size (2.8 nm in diameter) exhibited the fastest electron transfer rate of $3.8 \times 10^{-7} \text{ s}^{-1}$ where it is consistent with the former results that the band alignment of core and shell for this QDs are most favorable for carrier transfer. CdSe (3.1 nm)/CdS QDs and CdSe (3.5 nm)/CdS QDs showed similar electron transfer rate of $0.5 \times 10^{-7} \text{ s}^{-1}$ and $0.8 \times 10^{-7} \text{ s}^{-1}$, respectively. For CdSe (4.8 nm)/CdS QDs with the largest core size, the electron transfer rate cannot be calculated according to the equation because the band gap of the CdSe core is becoming narrower, leading to more enhanced confinement from the CdS shell which indicated that the electrons have less probability to transfer to the shell regions. To sum, with the increasing of the CdSe core size, the band gap of CdSe core is becoming narrower, leading to a lower electron transfer efficiency

from core to the shell.

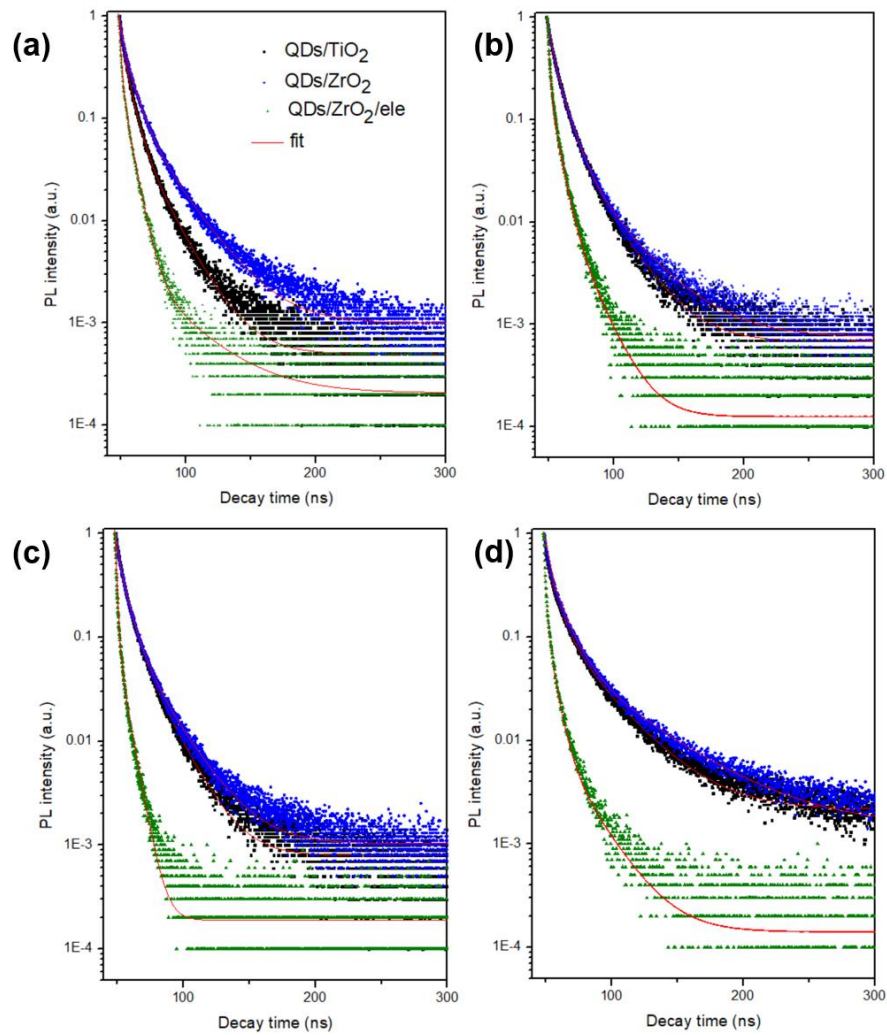


Figure 3.8 PL decay spectra of (a) CdSe (2.8 nm)/CdS core/shell QDs (b) CdSe (3.1 nm)/CdS core/shell QDs (c) CdSe (3.5 nm)/CdS core/shell QDs and (d) CdSe (4.8 nm)/CdS core/shell QDs after deposited into TiO₂ films, ZrO₂ films and ZrO₂ films in the presence of an electrolyte with the excitation light of 444 nm.

Table 3.2 Lifetime with different substrates and charge transfer rate.

QDs	QDs with TiO ₂ (ns)	QDs with ZrO ₂ (ns)	QDs with electrolyte (ns)	K_{et} (10 ⁷ s ⁻¹)	K_{ht} (10 ⁷ s ⁻¹)
CdSe (2.8nm)/CdS	8.6	12.8	6.7	3.8	7.1
CdSe (3.1nm)/CdS	10.9	11.5	3.2	0.5	22.5
CdSe (3.5nm)/CdS	9.9	10.8	4.3	0.8	14.1
CdSe (4.8nm)/CdS	15.2	14.4	3.9	-0.4	18.9

3.3 Theoretical calculation of QDs

Ultraviolet photoelectron spectroscopy (UPS) with He I radiation (21.21 eV) was used to estimate the Fermi level and maximum valance band energy level of four CdSe core QDs. The minimum conduction band energy level was calculated through the UPS results and the absorption spectra.⁵² Figure 3.9 showed the UPS analysis of CdSe (2.8 nm), CdSe (3.1 nm), CdSe (3.5 nm) QDs and CdSe (4.8 nm) CdSe core QDs. From the UPS data, the Fermi level (E_F) four core QDs is located at -2.81 eV for CdSe (2.8 nm) QDs, -3.41 eV for CdSe (3.1 nm) QDs, -4.11 eV for CdSe (3.5 nm) QDs and -4.51 eV for CdSe (4.8 nm) QDs, respectively respect of vacuum level according to the high energy cut-off (E_h). While the low energy cut-off (E_l) of 2.1 eV indicates the maximum valence band at -5.11, -5.66, -6.21 and -6.31 eV for four QDs. According to these data and the estimation of the band gap from the Tauc plot, the minimum CB is located at -2.8, -3.4, -4.04 and -4.26 eV for four QDs, respectively. All the levels were shown in Figure 3.10 and Table 3.3 following the UPS results.

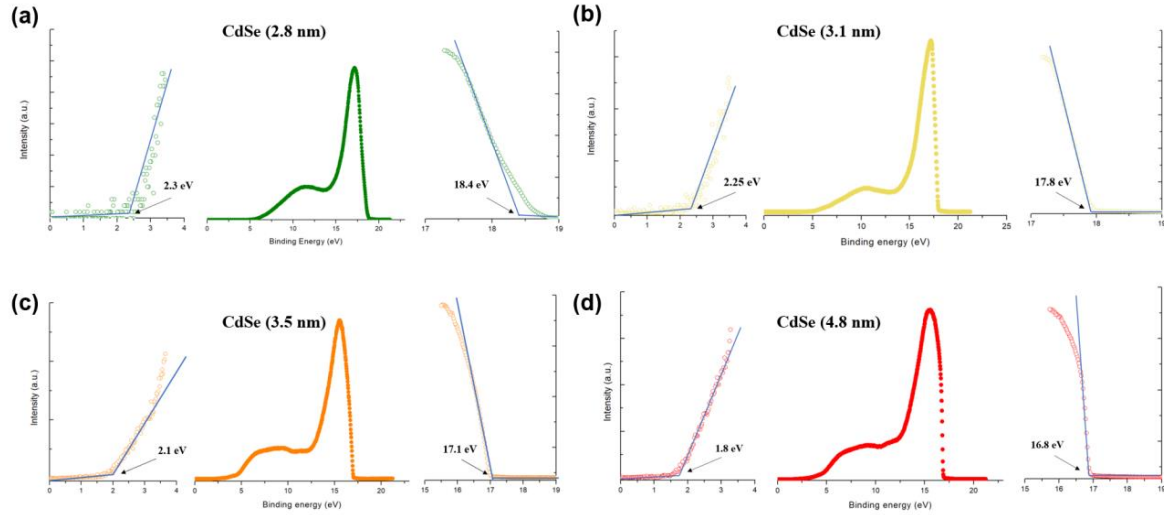


Figure 3.9 UPS spectra of (a) CdSe (2.8 nm) QDs (b) CdSe (3.1 nm) QDs (c) CdSe (3.5 nm) QDs (d) CdSe (4.8 nm) QDs and high, low binding energy cutoff.

Figure 3.10 also exhibited the CdSe/CdS core/shell structure and the corresponding band position of four core/shell QDs. The levels of CdSe core are determined by the former UPS results while the levels of CdS is using CdS bulk materials' levels, following by the previous literatures. According to the Figure 3.10, it is obvious that the band gap of CdSe QDs is becoming narrower with larger core size. Thus, the core/shell band alignment is changed from Type II to Quasi-Type II which is consistent with the former PL lifetime results.

Table 3.3 Potential (respect to vacuum) of CB, VB and Fermi level for different QDs following the UPS.

QDs	E_h (eV)	E_l (eV)	E_F (eV)	E_{VB} (eV)	E_{CB} (eV)	Band gap (eV)
CdSe(2.8nm)/CdS	18.40	2.30	-2.81	-5.11	-2.80	2.31
CdSe(3.1nm)/CdS	17.80	2.24	-3.41	-5.66	-3.40	2.26
CdSe(3.5nm)/CdS	17.10	2.10	-4.11	-6.21	-4.04	2.17
CdSe(4.8nm)/CdS	16.70	1.80	4.51	-6.31	-4.26	2.05

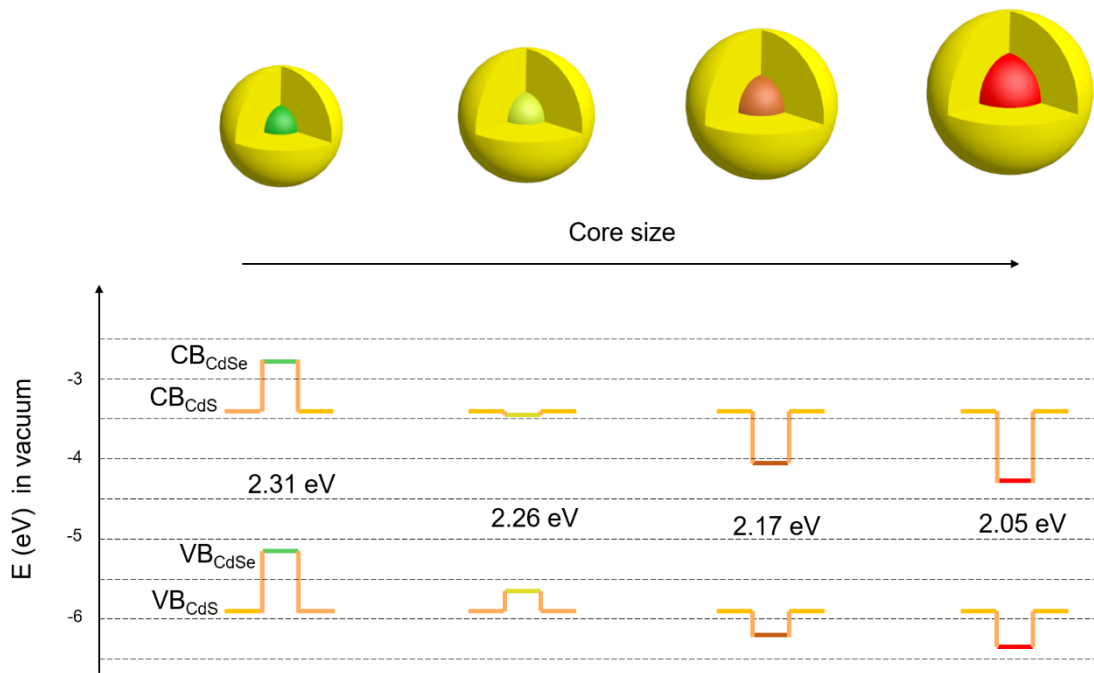


Figure 3.10 Schematic diagram of four CdSe core QDs [CdSe (2.8 nm) QDs (b) CdSe (3.1 nm) QDs (c) CdSe (3.5 nm) QDs (d) CdSe (4.8 nm) QDs] and their band position (conduction/valence band) calculated following the UPS results.

To further verify the carrier dissociation behavior of four types of CdSe/CdS core/shell QDs, the theoretical electron-hole wave functions was calculated. Typically, the electron [$\psi_e(r)$] and hole [$\psi_h(r)$] wave functions for the four types of core/shell QDs were calculated by solving the stationary Schrödinger equation in spherical geometry. Figure 3.11 (a) showed the $\psi_h(r)$ and $\psi_e(r)$ as the function of core radius and the dashed lines indicates the position of the core radius for each core/shell QDs and the areas with shadow (areas on the right of the dashed lines) showed the probability of the electron leaking from core to the shell regions. This theoretical result indicated that four types of CdSe/CdS core/shell are all belonging to Quasi-Type II core/shell architecture. Figure 3.11 (b) showed the electron/hole overlapping area of four types of QDs and the electron leakage area as the function of core size. The value of overlapping area increases with the larger size of the core which is consistent with the previous results that the electrons have more probability to confine in the core with the increasing core size.

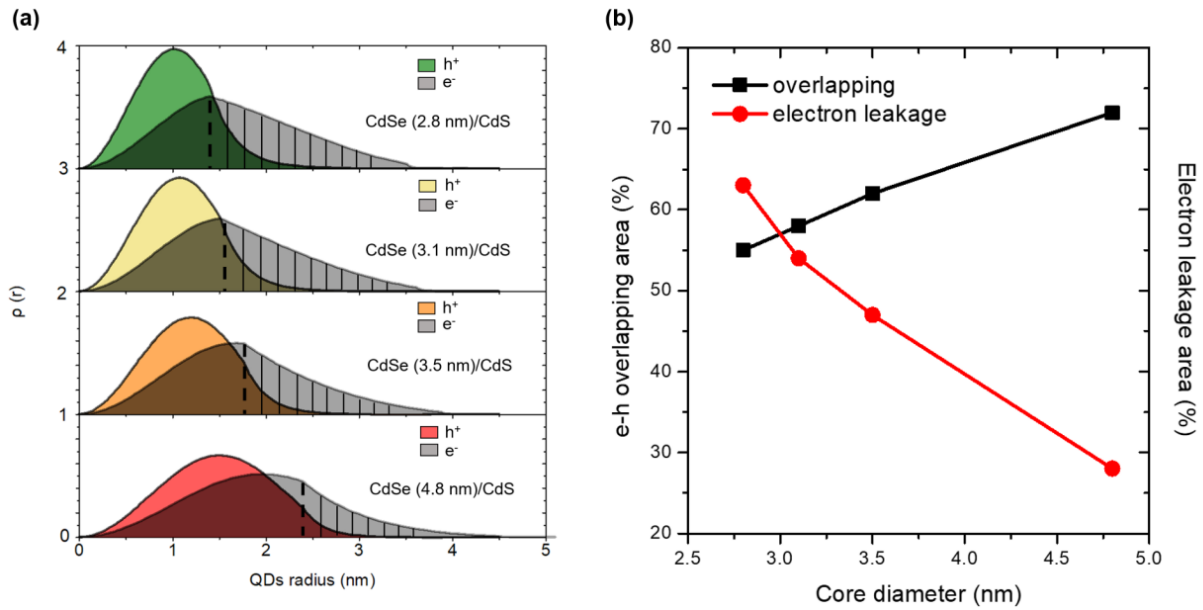


Figure 3.11 (a) Spatial probability distribution value $\rho(r)$ of electrons and holes as a function of QD radius (nm) for four CdSe/CdS core/shell QDs [CdSe (2.8 nm)/CdS QDs, CdSe (3.1 nm)/CdS QDs, CdSe (3.5 nm)/CdS QDs and CdSe (4.8 nm)/CdS QDs] (dashed lines show the radius position and the shadow areas indicate the electrons in the shell regions); (b) the overlapping area and electron leakage area as the function of core radius.

Table 3.4 Calculated electron-hole (e-h) overlapping area variations from the theoretical measurements for 4 CdSe/6CdS core/shell QDs as the function of CdSe core size.

QDs	R^* (nm)	H^* (nm)	e-h overlapping area (10^{-10}cm^2 %)	Electron leakage (10^{-10}cm^2 %)
CdSe (2.8 nm)/CdS	1.40	2.0 ± 0.1	55	63
CdSe (3.1 nm)/CdS	1.55	2.0 ± 0.1	58	54
CdSe (3.5 nm)/CdS	1.75	2.0 ± 0.1	62	47
CdSe (4.8 nm)/CdS	2.40	2.0 ± 0.1	72	28

3.4 PEC and stability performance

Generally, according to Figure 3.12, the PEC cell includes three parts, QDs based photoanode as working electrode, counter-electrode (Pt) and electrolyte ($\text{Na}_2\text{S}/\text{Na}_2\text{SO}_3$). Upon solar irradiation, the electron/hole pair will generate and dissociate at the QDs/ TiO_2 interfaces. Subsequently, the electron will be injected into the CB of TiO_2 due to the band bending while the holes will be consumed by the $\text{Na}_2\text{S}/\text{Na}_2\text{SO}_3$ electrolyte (pH \sim 13). Then the electrons will transfer to the FTO and further to counter-electrode to produce H_2 on the surface of Pt sheet.

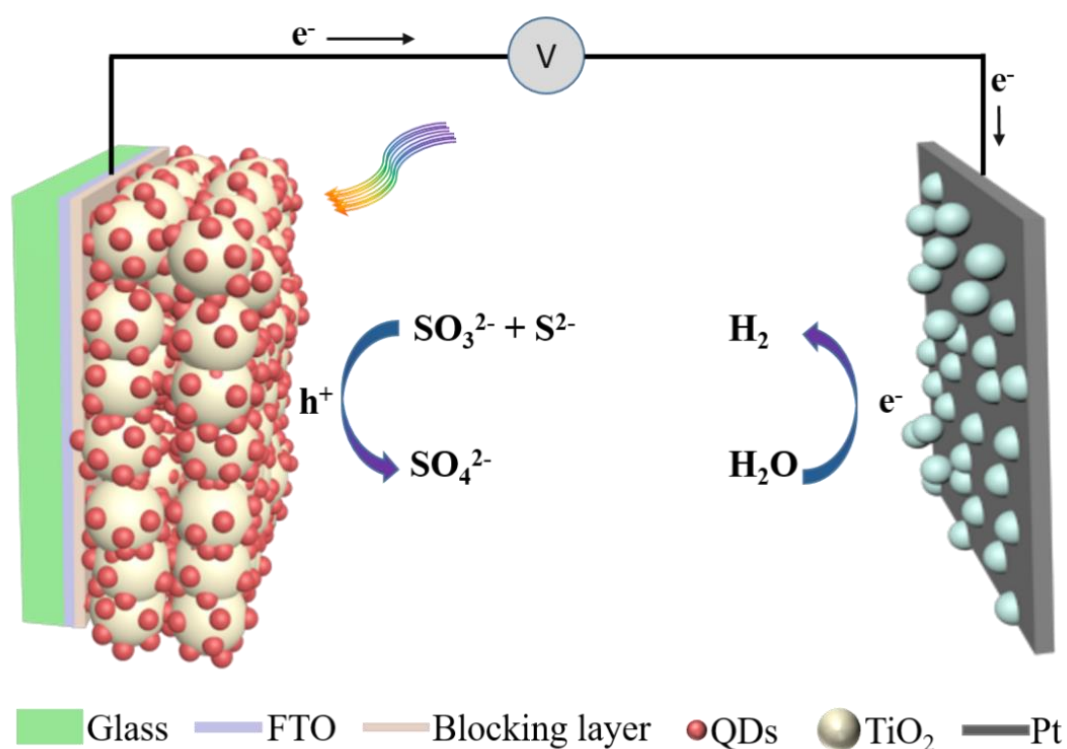


Figure 3.12 Schematic diagram of PEC cell based on CdSe/CdS QDs. The images show the structure of the photoanode which includes the glass, FTO, blocking layer, QDs and TiO_2 mesoporous films and the cathode is used Pt sheet while electrolyte is used $\text{SO}_3^{2-}/\text{S}^{2-}$.

In Figure 3.13, the HR-TEM images show that the CdSe (3.5 nm)/CdS QDs are successfully deposited onto mesoporous films through EPD. After the EPD process, the QDs/ TiO_2 photoanode will be merged into CTAB methanolic solution for 2 cycles of ligand exchange. And another two cycles of ZnS protection layers are further conducted before the PEC and

stability measurement.

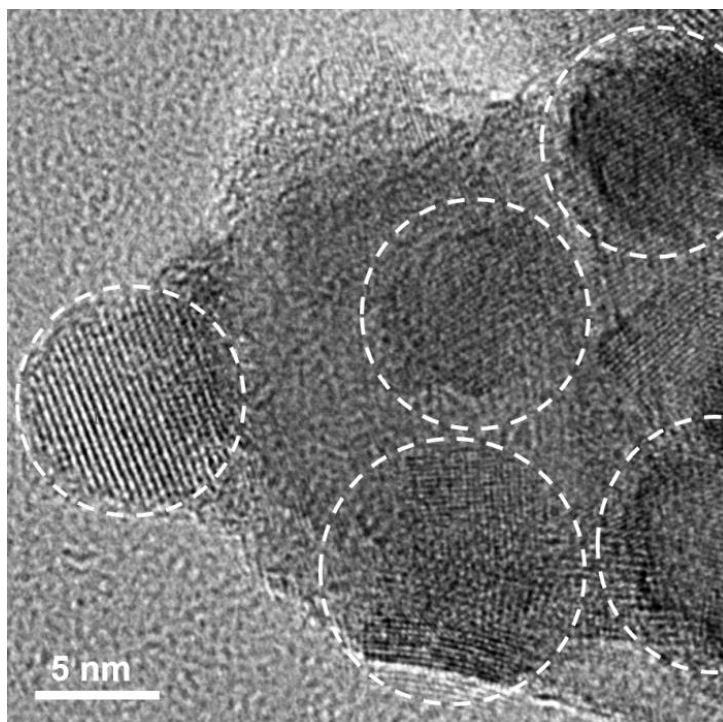


Figure 3.13 HR-TEM image of CdSe (3.5 nm)/CdS QDs onto mesoporous TiO₂ film where the white circle indicates the position of QDs.

To testify the PEC performance, the PEC devices are finally measured under dark and continuous illumination (AM 1.5 G, 100 mW/cm²) by using a typical three electrode configuration with a working electrode (QDs based photoanode), Ag/AgCl (saturated with KCl solution) reference electrode and Pt counter electrode. PEC performance based on CdSe core QDs is shown in Figure 3.14. First, the *J-V* curves of four CdSe core QDs were conducted. The saturated photocurrent density for four CdSe core QDs is 8.8 mA/cm² for CdSe (2.8 nm) QDs, 9.9 mA/cm² for CdSe (3.1 nm) QDs, 10.7 mA/cm² for CdSe (3.5 nm) QDs and 11.3 mA/cm² for CdSe (4.8 nm) QDs, respectively. The PEC performance results of four CdSe QDs indicate that the photocurrent density increases with the increasing CdSe core size which is mainly due to enhanced absorption range brought by the larger QDs. In other word, for CdSe bare QDs, the dominant parameter for PEC performance is the absorption range.

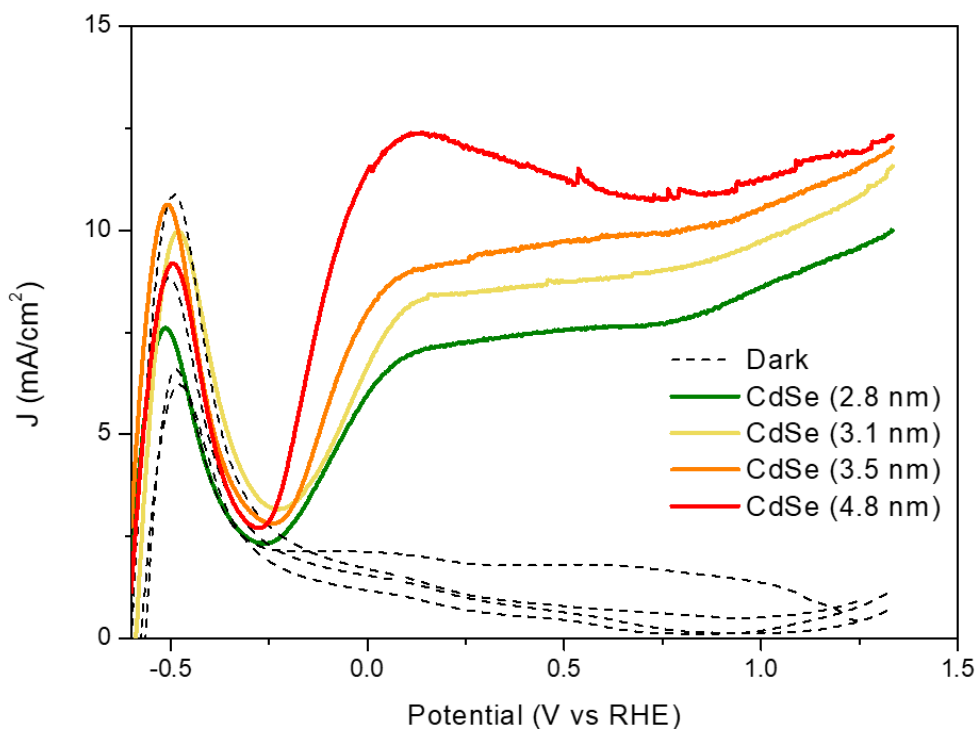


Figure 3.14 Photocurrent density-potential dependence of TiO₂ sensitized with four types of CdSe core QDs (CdSe (2.8 nm) QDs (b) CdSe (3.1 nm) QDs (c) CdSe (3.5 nm) QDs (d) CdSe (4.8 nm) QDs) in the dark (black dashed curves), and under continuous (chromatic curves) illumination (AM 1.5 G, 100 mW cm⁻²).

For four types of CdSe/CdS core/shell QDs which shown in Figure 3.15, the saturated photocurrent density of CdSe (2.8 nm)/CdS QDs based anode can reach 8.8 mA/cm² under one sun illumination (AM 1.5 G, 100 mW/cm²). Whereas the saturated photocurrent density of CdSe (3.1 nm)/CdS QDs based photoanode increased up to 15.8 mA/cm² which almost two times larger than CdSe (2.8 nm)/CdS QDs based photoanode. Moreover, for CdSe (3.5 nm)/CdS QDs based photoanode, the photocurrent density can achieve 17.4 mA/cm² which is almost the highest photocurrent density even compared to alloyed QDs based photoanode. However, CdSe (4.8 nm)/CdS QDs which has the largest core size based photoanode only has 12.9 mA/cm² of the saturated photocurrent density, lower compared to CdSe (3.1 nm)/CdS and CdSe (3.5 nm)/CdS QDs. The PEC results are so interesting that for a relatively small CdSe core, the absorption is the dominant parameter for PEC performance. Even the electron transfer rate is much higher for CdSe (2.8 nm)/CdS QDs compared to CdSe (3.1 nm)/CdS and CdSe (3.5

nm)/CdS QDs, the PEC performance is still much lower due to weaker absorption. However, when the CdSe core is large enough, the absorption is no longer be the dominant factor for PEC performance where the photocurrent density of CdSe (4.8 nm)/CdS QDs based photoanode is much lower than CdSe (3.1 nm)/CdS and CdSe (3.5 nm)/CdS QDs based photoanodes. It's mainly because the carrier transfer efficiency starts to determine the ultimate PEC performance rather than the absorption. Even though the absorption of CdSe (4.8 nm)/CdS QDs is higher than CdSe (3.1 nm)/CdS and CdSe (3.5 nm)/CdS QDs, the electron transfer rate is much lower, leading to more recombination inside of QDs. Thus, the CdSe (3.5 nm)/CdS QDs were proved to be the optimized core size as well as band alignment of CdSe/CdS architecture.

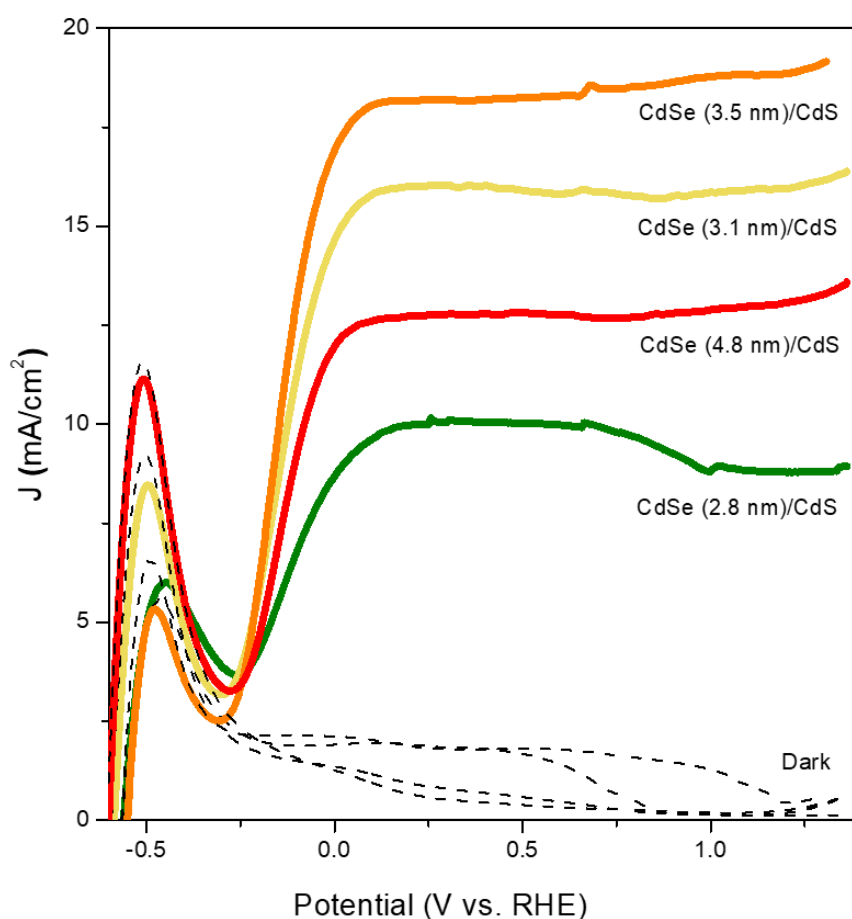


Figure 3.15 Photocurrent density-potential dependence of TiO₂ sensitized with four types of CdSe/CdS core/shell QDs (CdSe (2.8 nm)/CdS QDs, CdSe (3.1 nm)/CdS QDs, CdSe (3.5 nm)/CdS QDs and CdSe (4.8 nm)/CdS QDs) in the dark (black dashed curves), and under continuous (chromatic curve) illumination (AM 1.5 G, 100 mW cm⁻²).

Thus, to further improve the PEC performance based on the optimized core size of CdSe (3.5 nm)/CdS QDs, alloyed layers were applied to replace the pure CdS shells, forming the structure of CdSe (3.5 nm)/(CdSe_xS_{1-x})₅/CdS QDs ($x = 0.5$) QDs. Then the alloyed QDs were also applied with mesoporous TiO₂ films for the *J-V* measurement. According to the Figure 3.16, it turns out the photocurrent density of alloyed QDs based photoanode can achieve as high as unprecedented 22 mA/cm² under one sun illumination (AM 1.5 G, 100 mW/cm⁻²). Moreover, Figure 3.16 (b) showed the photocurrent density of alloyed QDs based photoanode as the function of time with the light on/off. It is obviously observed the photo-response when the anode received incident solar illumination and the highest photocurrent density is consistent with the results shown in Figure 3.16 (a). The highly efficient PEC performance of photoanode based on alloyed QDs is because the alloyed core/shell QDs have the optimized band alignment which balanced the parameters of absorption as well as the carrier transfer efficiency. Moreover, the intermediate alloyed layers serve as the short carrier pathways, leading to a more efficient carrier separation and transfer. As a result, the recombination can be largely suppressed. When compared to the photoanode with highest photocurrent density up-to-date, the core size is optimized via the band engineering approach.

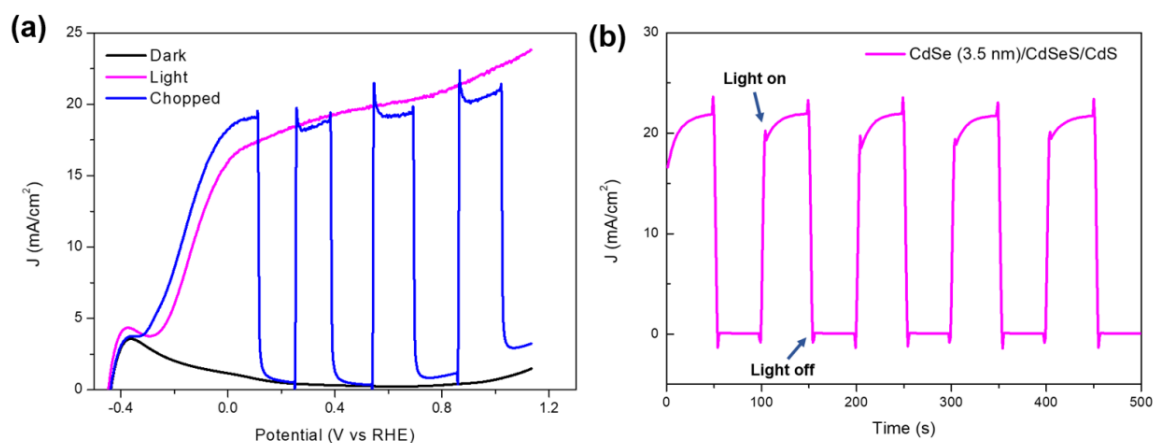


Figure 3.16 (a) Photocurrent density-potential dependence of TiO₂ sensitized with alloyed CdSe/CdSeS/CdS QDs in the dark (black curve), under continuous (magenta curve) and chopped (blue curve) illumination; (b) Photo photocurrent density versus time of alloyed QDs with the control of light on/off which indicates the photoresponse of as-prepared photoanode.

The incident photon-to-electron conversion efficiency (IPCE) spectra of as-prepared QDs have been estimated under different monochromatic wavelengths (Figure 3.17). The IPCE spectra can reveal the photo to current density efficiency under specific wavelength. Moreover, it can also be an evidence of absorption range of QDs. In results, the optimized CdSe (3.5 nm)/CdS QDs-device exhibits overall higher IPCE values from 350 nm to 610 nm compared to the other three QDs-based photoanodes, suggesting more efficient photon-to-electron conversion which is consistent with PEC performance. It is notable that the IPCE of CdSe (4.8 nm)/CdS QDs-based photoanode is higher than other three QDs during the range over 630 nm which is mainly due to broaden absorption range.

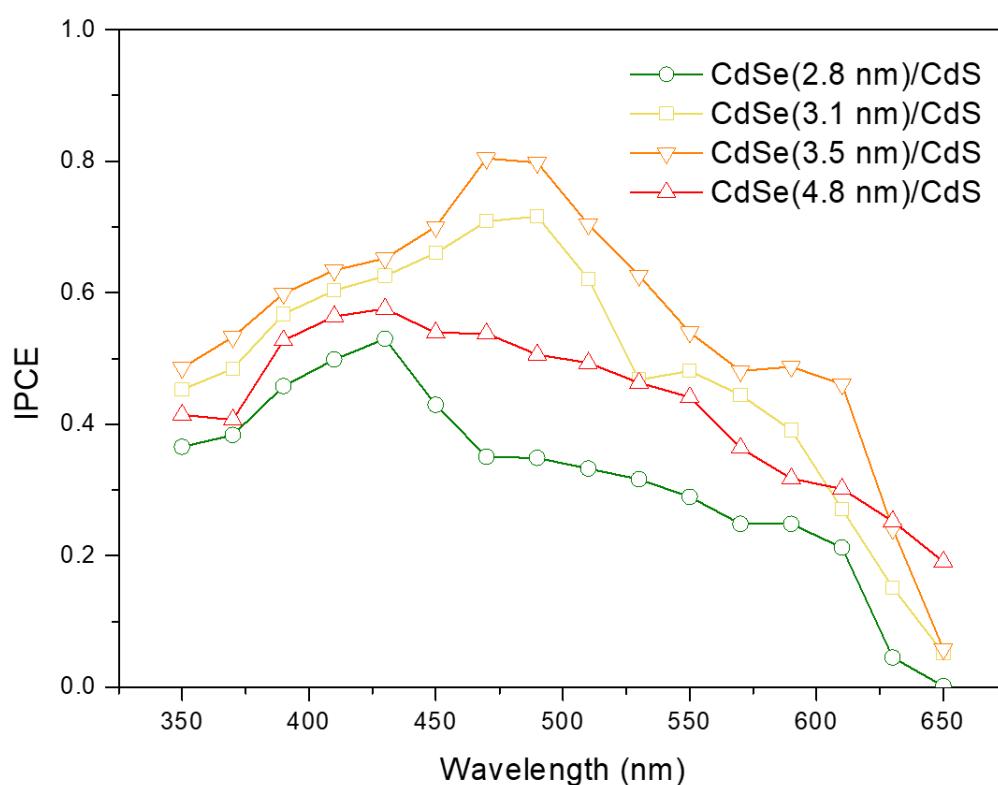


Figure 3.17 IPCE spectra of four types of CdSe/CdS core/shell QDs (CdSe (2.8 nm)/CdS QDs, CdSe (3.1 nm)/CdS QDs, CdSe (3.5 nm)/CdS QDs and CdSe (4.8 nm)/CdS QDs) under one sun power.

The stability performance is another critical factor for PEC devices. The stability measurement was conducted under continuous illumination under the bias of 0.6 V vs RHE. Due to the long

exposure under continuous illumination and strong alkaline electrolyte (pH \sim 13), the QDs based photoanode are necessary to coating a protection layer on the surface. Thus, 2 layers of ZnS passivation layers are applied to grow via SILAR method. In Figure 3.18, four types of CdSe/CdS and CdSe/CdSe_xS_{1-x}/CdS alloyed QDs are measured for 2-h stability performance. The stability results indicated that the alloyed QDs has the worst stability performance which only maintained 41 % of the initial photocurrent value. This is mainly because that fast carrier transfer rate also leads to a stronger recombination kinetics. For four CdSe/CdS QDs with pure shell, the CdSe (2.8 nm)/CdS QDs based photoanode has the best stability performance with the retention of 61 % of the photocurrent density. The CdSe (3.1 nm)/CdS QDs based photoanode exhibited 58 % of the retention after 2-h illumination while CdSe (3.5 nm)/CdS QDs based photoanode can maintain 56 % of the initial photocurrent. For CdSe (4.8 nm)/CdS QDs based photoanode which has the largest core size can only keep 50 % of the initial photocurrent value.

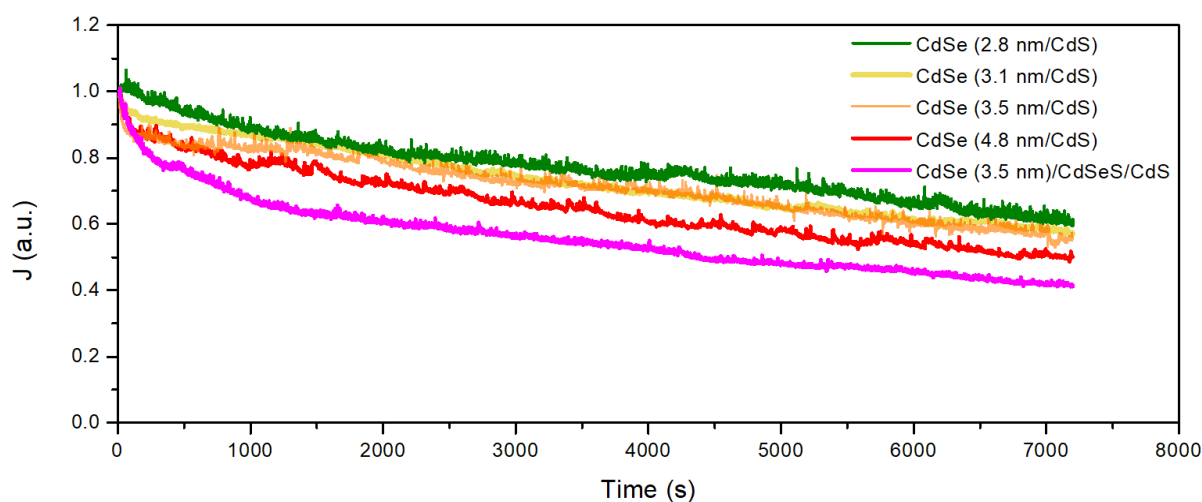


Figure 3.18 Stability measurements (photocurrent density as a function of time) of the four types of CdSe/CdS QDs (CdSe (2.8 nm)/CdS QDs, CdSe (3.1 nm)/CdS QDs, CdSe (3.5 nm)/CdS QDs and CdSe (4.8 nm)/CdS QDs) and alloyed CdSe/CdSeS/CdS QDs based photoanode at 0.6 V versus RHE under AM 1.5 G illumination (100 mW cm^{-2}) with 2 ZnS coating.

Figure 3.19 shows the PEC performance and stability results which indicated that the stability

performance decreased with larger core size which demonstrated that the carrier transfer efficiency is the critical factor for stability performance. With lower photocurrent and carrier transfer efficiency, there are more recombination events inside the QDs while photo-oxidation will also happen when more holes accumulate on the valence band. Such stability performance results will give more perspectives on the design of core/shell QDs architecture in the future.

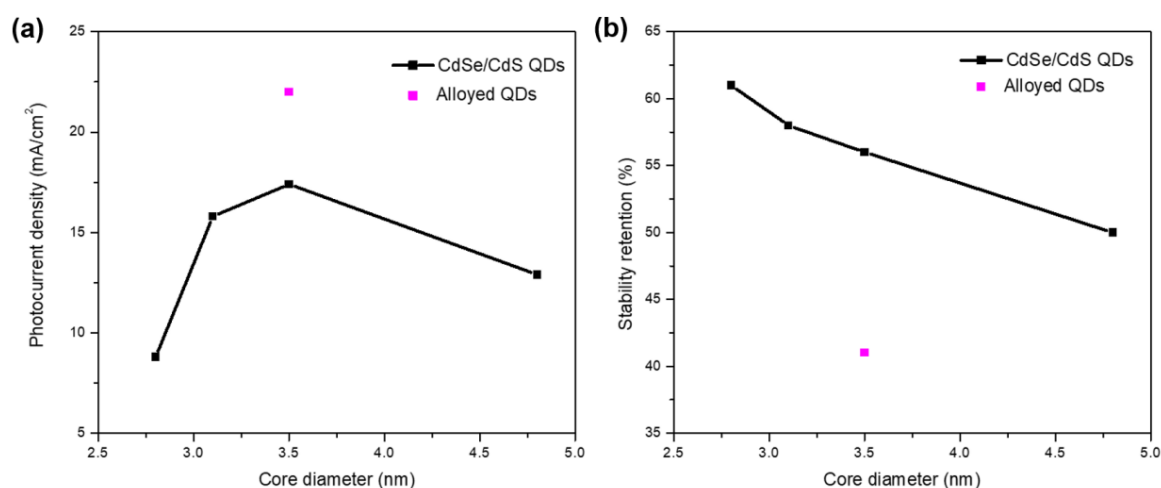


Figure 3.19 (a) Photocurrent density and (b) stability retention of four CdSe/CdS core/shell QDs (CdSe (2.8 nm)/CdS QDs, CdSe (3.1 nm)/CdS QDs, CdSe (3.5 nm)/CdS QDs and CdSe (4.8 nm)/CdS QDs) and alloyed CdSe/CdS/CdS QDs.

3.5 Summary

In this chapter, the CdSe core size effect based on CdSe/CdS core/shell QDs for PEC H₂ generation was discussed thoroughly. Generally, I designed and synthesized four types of CdSe/CdS core/shell QDs with the growth time of NC from 2-10 min under the same temperature. By controlling different core size and similar shell thickness, band alignment between core and shell is changed accordingly. As a result, the carrier dynamic behavior is dramatically affected as well as the absorption range of the QDs. When the four types CdSe core QDs and CdSe/CdS core/shell QDs were applied for the solar-driven H₂ generation tests, the saturated photocurrent density of CdSe core QDs based photoanodes exhibited the increasing value with larger core size which indicates the absorption range is the critical factor for the PEC performance. For CdSe/CdS core/shell QDs, the saturated photocurrent density

first increases from 8.8 mA/cm² for CdSe (2.8 nm)/CdS QDs to 15.8 mA/cm² for CdSe (3.1 nm)/CdS QDs and 17.4 mA/cm² for CdSe (3.5 nm)/CdS QDs, then decreasing to 12.9 mA/cm² for CdSe (4.8 nm)/CdS QDs, respectively. Thus, the CdSe (3.5 nm)/CdS core/shell QDs is approved to be the optimized core size in CdSe/CdS core/shell architecture for PEC performance which is mainly because the QDs have the enhanced absorption range compared to QDs with smaller core while its charge transfer efficiency is higher than QDs with larger core. In other words, when the CdSe core is small, the absorption range is the dominant factor for PEC performance while the photocurrent value will increase with larger core size. When the CdSe core size is larger than 3.5 nm in diameter, the carrier transfer efficiency starts to become the most important parameter for PEC performance which is the reason for the drop of photocurrent value with larger core size.

Chapter 4 CdSe/CdSe_xS_{1-x}/CdS alloyed QDs for PEC H₂ generation

As discussed above, CdSe/CdS core/shell architecture can be a promising candidate as light harvester for optoelectronic devices by controlling the core size and shell thickness. Learned from last chapter, if the CdSe core size increases, the absorption will be enhanced, however, the carrier transfer efficiency will decrease. Same phenomenon for shell thickness, if the CdS shell thickness is quite thick, the absorption range will be improved but with lower carrier transfer efficiency. Thus, even the optimized core size and shell thickness can be found, the saturated photocurrent density is still restricted to limited absorption range (mostly due to CdS) as well as poor carrier separation and transfer.

In this chapter, based on the CdSe/CdS core/shell QDs, the CdS shell composition can be further optimized with CdSe_xS_{1-x} alloyed shells, forming the structure of CdSe/CdSe_xS_{1-x}/CdS QDs. Such architecture can not only broaden the absorption range, but also increase the carrier transfer efficiency. There are some pioneer works reporting alloyed QDs have optimized carrier dynamics through the composition engineering.⁹⁹⁻¹⁰¹ More importantly, the Auger recombination can be suppressed dramatically by adding alloyed layers in the pure shell. Thus, the motivation of this this work is to figure out how alloyed layers will engineer the band alignment between the core and shell and the final impact on the PEC performance.

First, I synthesized CdSe/CdS core/shell QDs with six monolayers of CdS. For CdSe/Alloyed#1 QDs, the first four CdS layers were replaced with CdSe_{0.5}S_{0.5} alloyed layers, forming the structure of CdSe/(CdSe_{0.5}S_{0.5})₄/(CdS)₂. For CdSe/Alloyed#2 QDs, the five CdS layers were replaced with CdSe_xS_{1-x} alloyed layers (x changes with each layer). Then I applied three types of core/shell QDs for PEC H₂ generation. Afterwards, the carrier dynamic behavior was further investigated.

4.1 Characterization of QDs

The CdSe QDs were synthesized through hot-injection approach. Afterwards, the shell was coated on the surface of CdSe via SILAR method. I synthesized three types of core/shell QDs,

denoted as CdSe/6CdS, CdSe/Alloy#1 and CdSe/Alloyed#2 QDs. The shell composition was controlled by adjusting the injection precursors. For example, when I coated CdS pure shell, I separately injected Cd(OA)₂ as the anion precursor and S-ODE as the cation precursor. The thickness was controlled by repeating such process for six times to grow 6 monolayers of CdS. For synthesizing CdSe/CdSe_xS_{1-x}/CdS alloyed QDs, the cation precursor was engineered into Se/S-ODE. In the case of CdSe/Alloyed#1 QDs, the molar ratio of Se/S is 1/1 in the first four monolayers while the ratio is changing with each monolayer for CdSe/Alloyed#2 QDs (9/1, 8/2, 7/3, 5/5, 3/7, 0/10). The ratio of Se/S for three types of QDs are shown in the Table 4.1. The characterizations of three types of QDs were conducted by TEM, XRD, XPS, UV-vis absorption spectra, PL spectra, etc. Then three types of QDs were applied for PEC H₂ generation for comparison. The carrier dynamic behavior was investigated for the mechanism explanation through PL lifetime measurement and theoretical calculation.

Table 4.1 Ratio of Se/S in shell as function of SILAR cycles.

Sample	1	2	3	4	5	6
CdSe/6CdS	0/10	0/10	0/10	0/10	0/10	0/10
CdSe/Alloy#1	5/5	5/5	5/5	5/5	0/10	0/10
CdSe/Alloy#2	9/1	8/2	7/3	5/5	3/7	0/10

4.1.1 Structure of QDs

The morphology and the crystal structure were first characterized by TEM images. According to the Figure 4.1, the TEM images showed that three types of QDs and their structure was shown in the inset of the images.

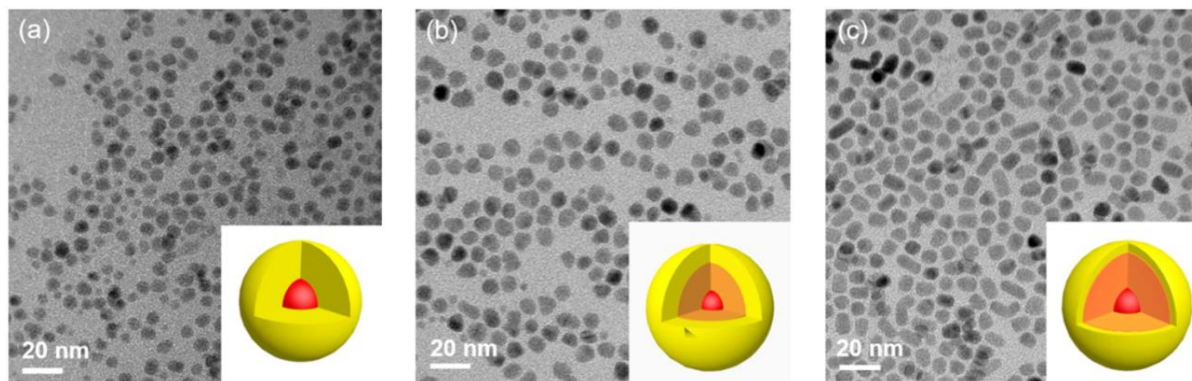


Figure 4.1 TEM images and QDs structure of (a) CdSe/6CdS; (b) CdSe/Alloy#1; (c) CdSe/Alloy#2 and the insets show the structure of as-synthesized QDs.

In the TEM images, it is obvious that the size of QDs is becoming larger. The size distribution of three types of QDs were shown in the Figure 4.2. The average CdSe core diameter and shell thickness were shown in Table 4.2. In the CdSe/CdS QDs, six monolayers of CdS were coated on the CdSe core (3.3 nm in diameter) with shell thickness of 1.96 nm, which is consistent with TEM images. By tuning the feeding ratio of Se and S precursors, CdSe/Alloy#1 and CdSe/Alloy#2 QDs with 2.07 nm and 2.50 nm in shell thickness, respectively, were obtained. The thicker shell for CdSe/Alloy#1 and CdSe/Alloy#2 giant QDs compared to CdSe/6CdS is due to the addition of elemental Se in the shell.²⁹ In brief, the overall diameters of as-synthesized alloyed QDs are 7.7 ± 0.8 nm for CdSe/Alloy#1 QDs and 7.9 ± 0.9 nm for CdSe/Alloy#2 QDs, respectively. And for CdSe/6CdS QDs, the final diameters are 7.2 ± 0.5 nm.

Table 4.2 Diameter and shell thickness of three types of QDs.

QDs	Diameter (nm)	Shell thickness (nm)
CdSe/6CdS	3.3	1.96
CdSe/Alloyed#1	3.3	2.07
CdSe/Alloyed#2	3.3	2.50

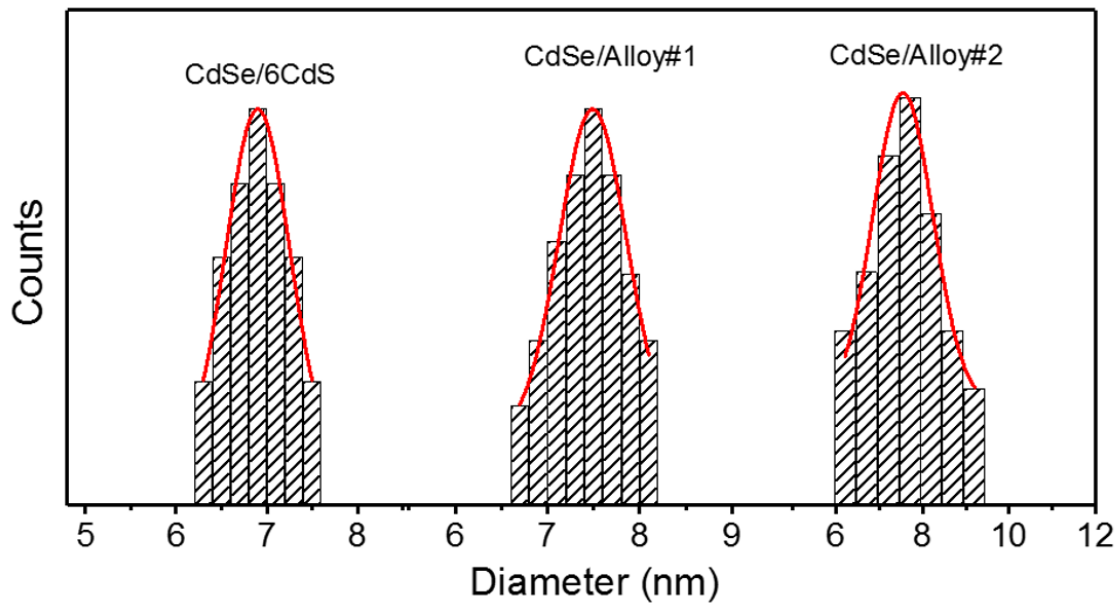


Figure 4.2 Size distribution of CdSe/6CdS, CdSe/Alloy#1 and CdSe/Alloy#2 QDs.

In the Figure 4.3, the HR-TEM image showed that the crystal lattice of CdSe/Alloy#2 QDs which indicates high crystallinity with lattice fringes. The lattice spacing ($d = 3.51 \text{ \AA}$) is corresponding to the (111) plane of the ZB crystal structure of CdSe.

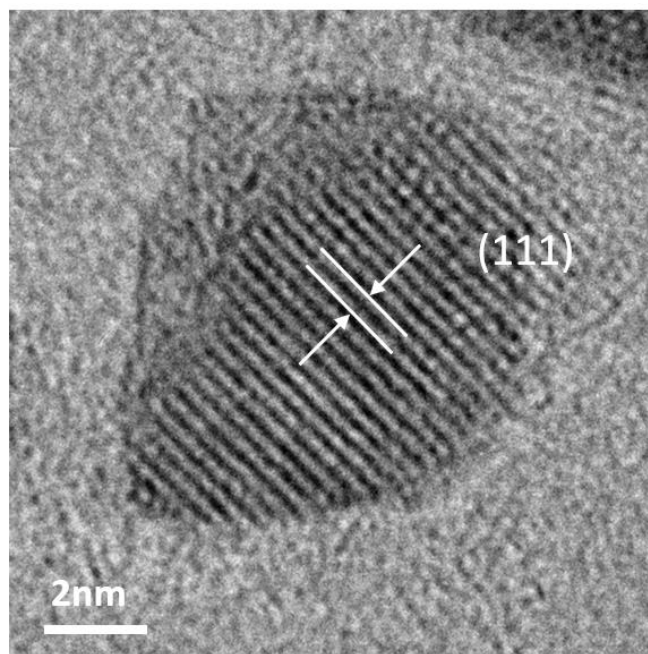


Figure 4.3 HR-TEM image of CdSe/Alloyed#2 QDs and the fringe indicates the (111) crystal plane of ZB crystal structure of CdSe.

SAED pattern was conducted for determining the structure of alloyed QDs. In the SAED pattern (Figure 4.4), the crystal planes (111), (311) and (220) are corresponding to ZB of CdSe and WZ of CdS for CdSe/Alloyed#1 QDs while (111), (102), (311), (220) and (103) planes to ZB of CdSe and WZ of CdS for CdSe/Alloyed#2 QDs.

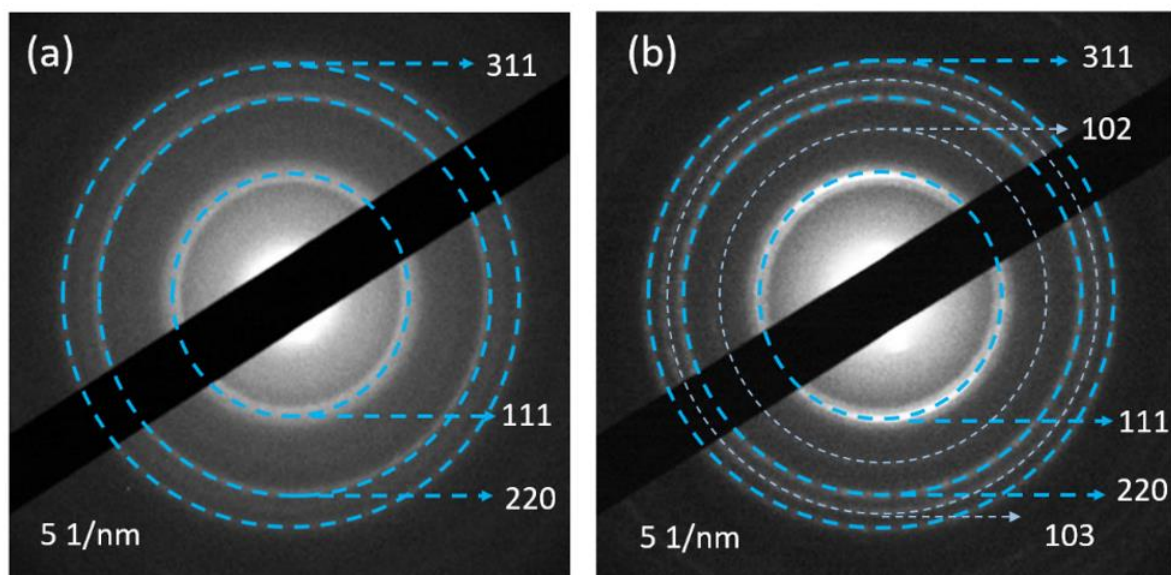


Figure 4.4 Selected area electron diffraction pattern: (a) CdSe/Alloyed#1 QDs, (b) CdSe/Alloyed#2 QDs.

From XRD pattern (Figure 4.5), the crystalline structure of the CdSe core in the CdSe/CdS QDs is ascribed to the ZB structure, while the CdS shell refers to the WZ crystal structure. For two types of the alloyed QDs (CdSe/Alloyed#1 and CdSe/Alloyed#2 QDs), the diffraction patterns showed that the shell is a mixture of ZB and WZ structures of CdSe(S).

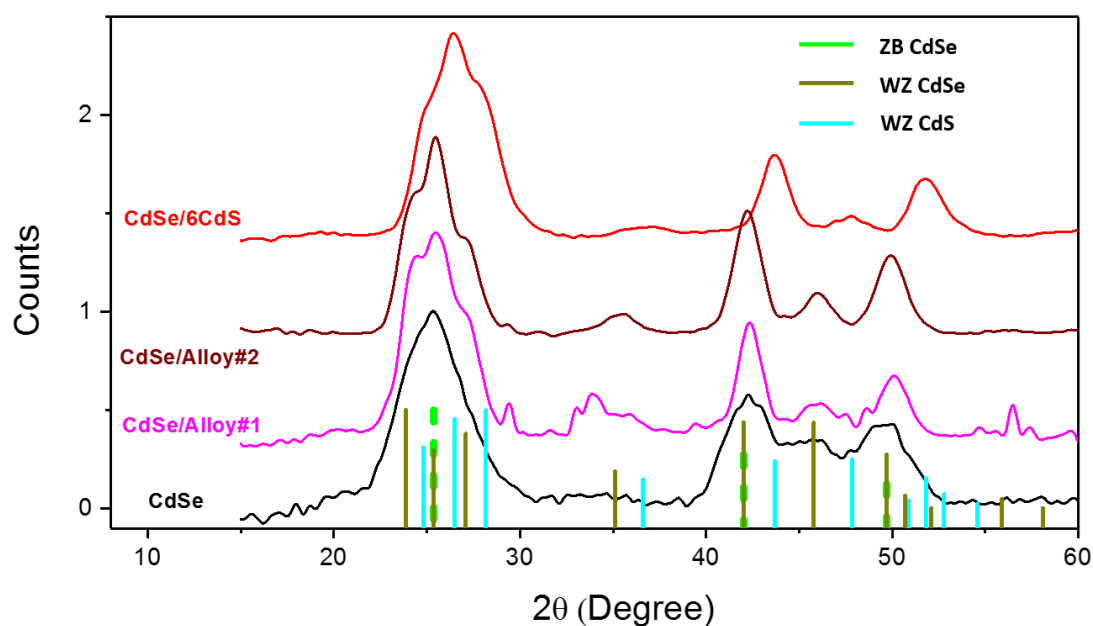


Figure 4.5 XRD pattern of CdSe, CdSe/6CdS, CdSe/Alloy#1 and CdSe/Alloy#2 QDs where the JCPDS card of ZB CdSe, WZ CdSe and WZ CdS are used for identification.

According to Figure 4.6, The high-resolution XPS spectra of small energy regions around the expected peak positions of each element. The binding energies recorded in the XPS analysis were calibrated by referencing the C 1s peak to 284.8 eV. The XPS spectra was carried out to confirm the composition. In XPS spectra (Figure 4.6), the characteristic peaks around 405 eV and 412 eV indicate the Cd $3d_{5/2}$ Cd $3d_{3/2}$, respectively. The peaks located at 54 eV are assigned to Se $3d$ while the peaks between 160-161 eV correspond to S $2p$. In summary, these results demonstrate the existence of element Cd, Se, S in CdSe/Alloy#2 QDs.

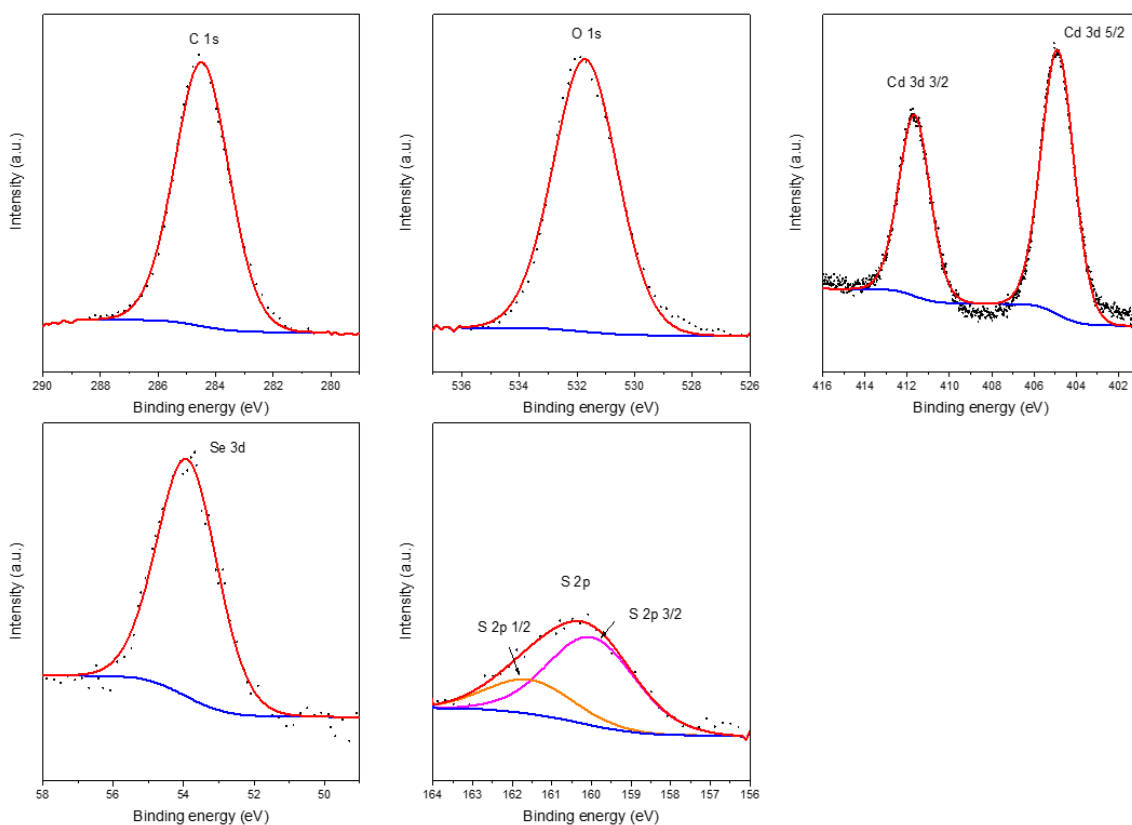


Figure 4.6 High-resolution XPS spectra of Cd 3d, Se 3d and S 2p in as-prepared CdSe/Alloy#2 QDs. The black dots are as-measured lines and the red lines represent the fitting lines.

4.1.2 Optical properties of QDs

Figure 4.7 (a) displayed the first-excitonic absorption peaks for three types of QDs in toluene are observed at ~ 591 nm (CdSe/6CdS QDs), 632 nm (CdSe/Alloy#1 QDs), and 626 nm (CdSe/Alloy#2 QDs), respectively. These results are consistent with the PL spectra presented in Figure 4.7 (b). The peak position of absorption and PL spectra was listed in Table 4.3. With the presence of interfacial alloyed layers, the absorption of QDs was shifted to longer wavelengths due to the narrower band gap of CdSe compared to CdS and the quantum size effect related to the increased size.⁷⁴ At the same time, the PL peak simultaneously was observed to red-shift due to the leakage of electrons from the core to the shell regions. The similar PL peak position in two alloyed QDs implies the same degree of electrons' leakage.

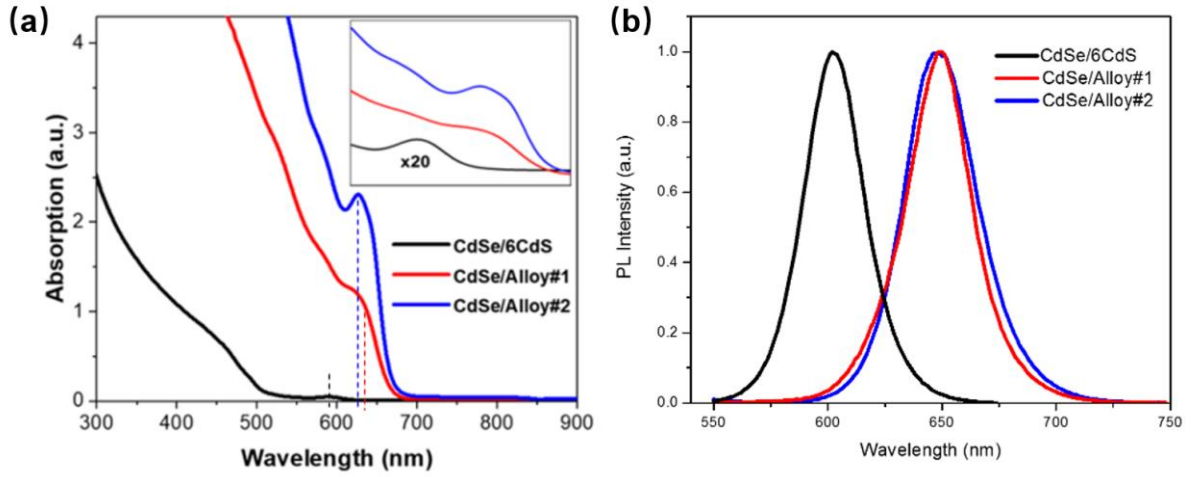


Figure 4.7 (a) UV-vis absorption and (b) PL spectra of CdSe/6CdS, CdSe/Alloy#1 and CdSe/Alloy#2 QDs.

Table 4.3 Optical parameters of three types of QDs in toluene.

Sample	Abs (nm)	PL (nm)
CdSe/6CdS	591	605
CdSe/Alloy#1	632	649
CdSe/Alloy#2	626	650

4.2 Carrier dynamics

To investigate the charge dynamic behavior of three types of QDs, TiO₂ and ZrO₂ mesoporous films were used as substrates on which the QDs are deposited. With the addition of the electrolyte which serves as hole scavenger, the holes' transfer rate can be calculated compared to the one without the electrolyte. Due to the band alignment between ZrO₂ and core/shell QDs, the ZrO₂ is used as benchmark where the charge injection does not occur and PL degradation can only be attributed to charge recombination. The average lifetime $\langle \tau \rangle$ was calculated by using the following equation:⁹⁷

$$\langle \tau \rangle = \frac{a_1\tau_1^2 + a_2\tau_2^2 + a_3\tau_3^2}{a_1\tau_1 + a_2\tau_2 + a_3\tau_3} \quad (4.1)$$

The electron/hole transfer rate was calculated based on the average lifetime of QDs on different substrates by referring to the following equations:^{97,102}

$$K(et) = \frac{1}{\langle\tau\rangle_{QDs/TiO_2}} - \frac{1}{\langle\tau\rangle_{QDs/ZrO_2}} \quad (4.2)$$

$$K(ht) = \frac{1}{\langle\tau\rangle_{QDs/ZrO_2(electrolyte)}} - \frac{1}{\langle\tau\rangle_{QDs/ZrO_2}} \quad (4.3)$$

Where the K_{et} and K_{ht} are the transfer rate for the electrons and holes, respectively. $\langle\tau\rangle_{QDs/TiO_2}$ (or electrolyte) and $\langle\tau\rangle_{QDs/ZrO_2}$ are the average lifetime for QDs on TiO_2 , and immersed in the electrolyte and on ZrO_2 , respectively. The values of lifetimes and carrier transfer rates are listed in Table 4.4.

Table 4.4 Lifetime with different substrates and charge transfer rate.

Sample	Lifetime with TiO_2 (ns)	Lifetime with ZrO_2 (ns)	Lifetime with electrolyte(ns)	Electron transfer rate K_{et} ($10^7/s$)	Hole transfer rate K_{ht} ($10^7/s$)
CdSe/6CdS	15	25	8	2.7	8.5
CdSe/Alloy#1	14	22	7	2.6	9.7
CdSe/Alloy#2	16	23	8	1.9	8.2

Generally, for three types of QDs, the hole transfer rates (K_{ht}) are much larger than the electron transfer rate (K_{et}) due to the large driving force (namely, the energy offset between the highest energy level of valance band of QDs and the energy level of SO_3^{2-}/S^{2-}) from QDs to electrolyte. However, the degree of carriers' dissociation is different in the three QDs, whereas K_{ht} is three times larger than K_{et} in CdSe/6CdS QDs. In the alloyed QDs, the K_{ht} increases to values up to 3.7 times larger than K_{et} for CdSe/Alloy#1 QDs and 4.3 times larger for CdSe/Alloy#2 QDs, respectively. This phenomenon indicates that band alignment was optimized by the alloyed layers which built a favorable band structure for the carriers to separate spatially, leading to fewer charge recombination events.¹⁰³⁻¹⁰⁵

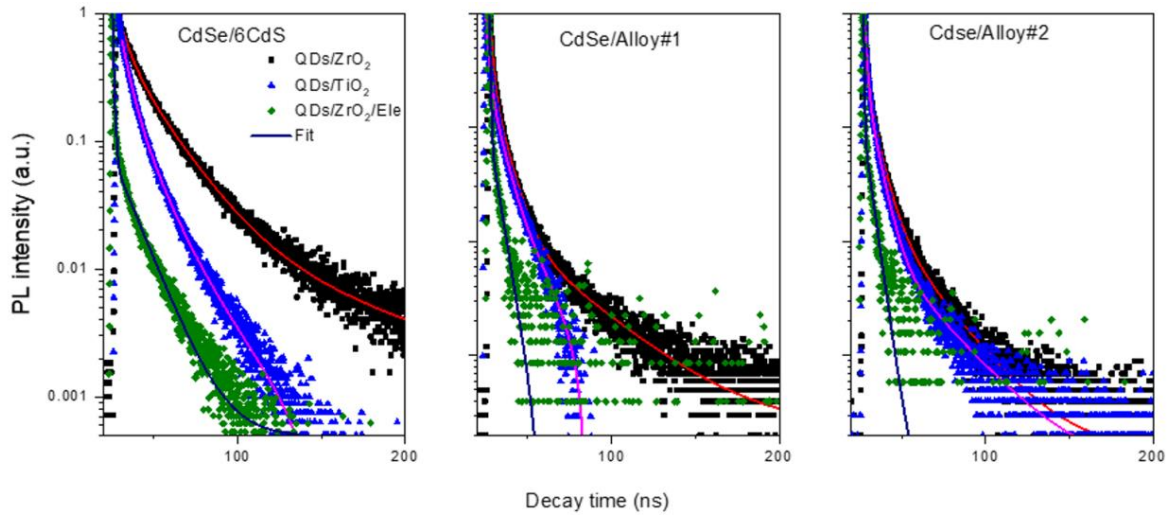


Figure 4.8 PL spectra of CdSe/6CdS, CdSe/Alloy#1 and CdSe/Alloy#2 QDs after deposited into TiO₂ films, ZrO₂ film and ZrO₂ film in the presence of electrolyte.

4.3 Theoretical calculation

To further verify the process of the carriers' dissociation, we calculated the theoretical electron-hole wave functions. The electron/hole [$\psi_e(r)$] and $\psi_h(r)$] wave function for two types of alloyed core/shell QDs and 6 SIALR cycles of CdS shell QDs were calculated by solving the stationary Schrödinger equation in spherical geometry.²⁹ The calculated spatial probability distribution [$\rho(r)$] of $\psi_e(r)$ and $\psi_h(r)$ as a function of QDs radius (nm) is shown in Figure 4.9. With the addition of alloyed layers, both the $\psi_e(r)$ and $\psi_h(r)$ showed an increasing leakage into the shell region as a consequence of favorable band alignment. According to Table 4.5, which showed the e-h spatial overlapping values and Figure 4.9 (according to the positions of dashed lines), the overlapping values for electrons and holes increase due to improved band alignment. As a result, the carrier recombination could be more severe in alloyed QDs. However, due to the different transfer rate of electrons and holes, more carriers could be transferred outside the QDs which dominates the values of current density.

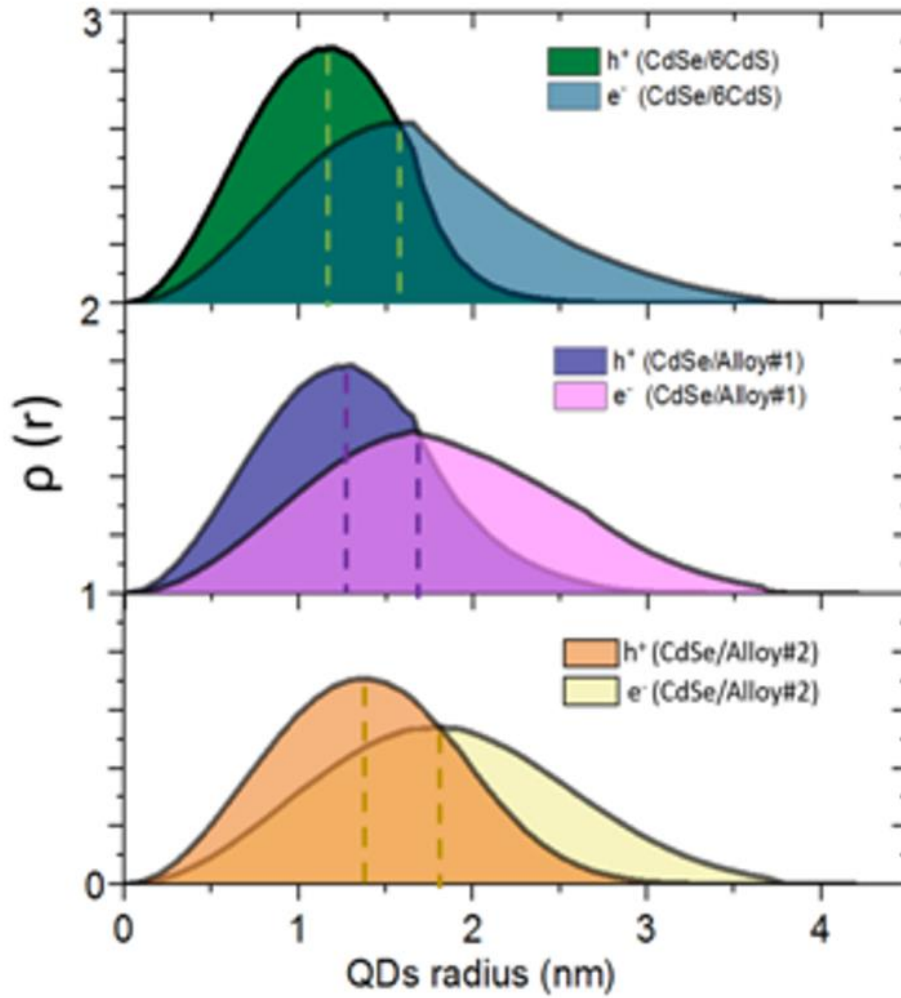


Figure 4.9 Spatial probability distribution value $p(r)$ of the electron and hole as a function of QD radius (nm) for CdSe/6CdS, CdSe/Alloy#1 and CdSe/Alloy#2 QDs (dashed lines show the positions of the peaks).

Table 4.5 The radius of core, thickness of shell and e-h spatial overlapping values for CdSe/6CdS, CdSe/Alloy#1 and CdSe/Alloy#2 QDs.

Core/Shell QDs structure	Radius (nm)	Thickness (nm)	e-h overlapping area (10^{-10} $\text{cm}^2 \%$)
CdSe/6CdS	1.65	1.96	64
CdSe/Alloy#1	1.65	2.07	67
CdSe/ Alloy#2	1.65	2.50	70

4.4 PEC and stability performance

Figure 4.10 showed the band structure and carrier transition of CdSe/Alloy#2 QDs based photoanode. In general, upon solar illumination, photogenerated excitons will dissociate into electron/hole pairs at the QDs/TiO₂ interface. The electrons will leak from the CdSe core to the shell region and will then be injected into the TiO₂ layer due to electronic band bending, subsequently collected by the FTO electrode. Finally, electrons are transported through an external circuit to the Pt counter electrode for water reduction. Since the conduction band level of CdS is higher than that of CdSe, the gradient band structure serves as a shortcut for electrons to overcome the original high energy barrier, thereby improving the likelihood for electrons to leak from the core to the shell. Meanwhile, the holes are extracted from the Na₂S/Na₂SO₃ electrolyte (pH ~ 13) which serves as hole scavenger. Benefiting from the gradient band structure of the CdSe/Alloy#2 QDs, the carriers are more likely to transfer from the core to shell then out of QDs with a lower probability for recombination inside the QDs. Similar to the CdSe/Alloy#2 QDs, the CdSe/Alloy#1 QDs provide an intermediate layer between the CdSe core and CdS shell which exhibits better charge transfer efficiency compared to CdSe/6CdS QDs. The relatively energy level for CdSe, CdS and TiO₂ are obtained from literatures while the energy level for CdSe_xS_{1-x} alloyed shell are estimated according to the ratio of Se and

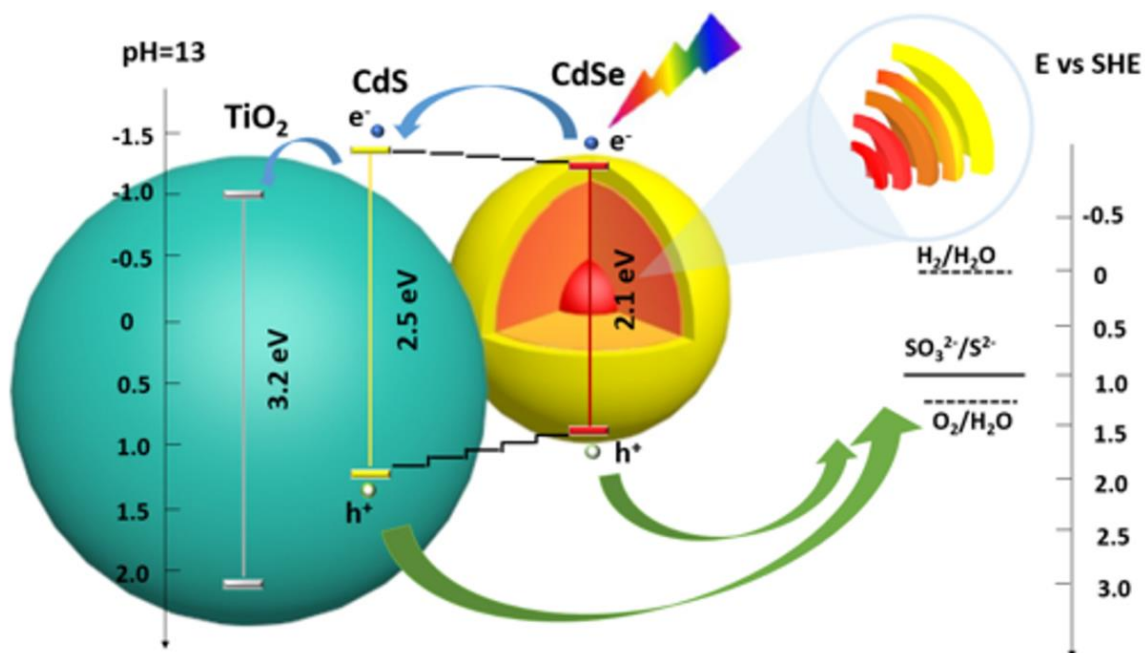


Figure 4.10 Schematic diagram of band structure and carrier transition of CdSe/Alloy#2 QDs based photoanode. Approximate energy levels of TiO₂ and QDs, together with related characteristic redox potentials. The arrows show the electron and hole transfer processes.

For preparing the QDs/TiO₂ photoanode, EPD process was carried out to deposit QDs in mesoporous TiO₂ film with 200 V for 2 hours. Afterwards, the photoanode was applied to the ligand exchange and ZnS passivation layer protection via SILAR method. According to the Figure 4.11, the cross-sectional SEM image and EDS mapping spectrum were shown to prove the existence of element Cd, Se, S, Ti and O. The thickness of the TiO₂ film was measured around 21.5 μm .

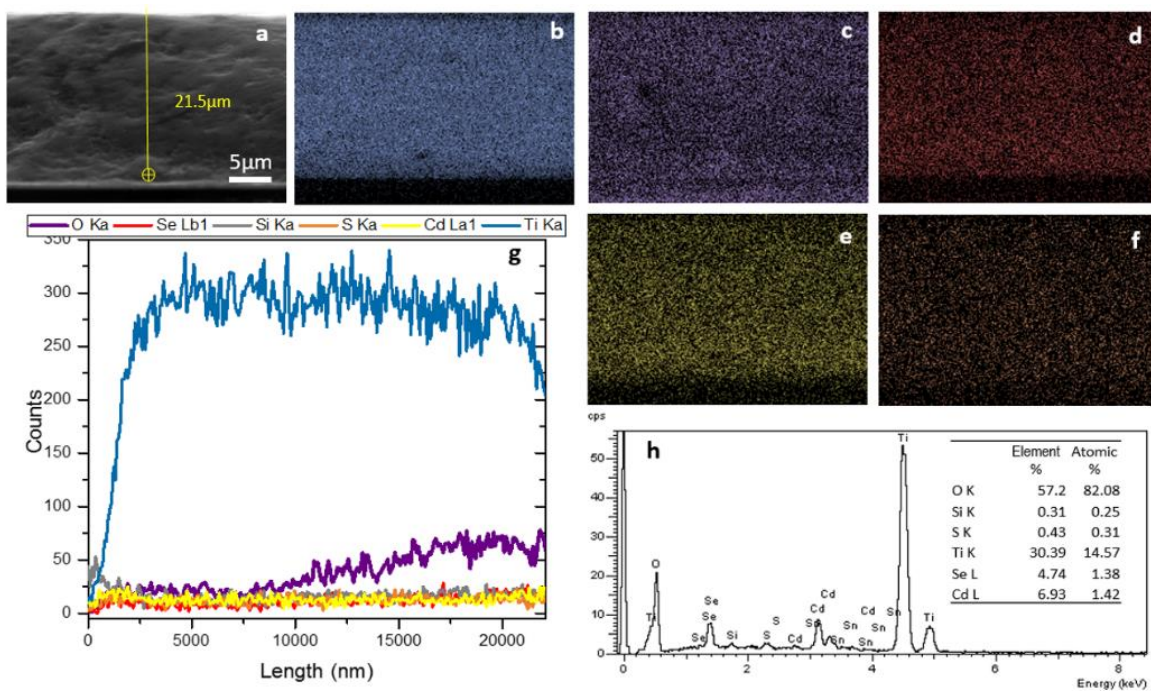


Figure 4.11 (a) Cross-sectional SEM image of CdSe/CdS QD-sensitized photoanode. EDS mapping analysis of all the elements including (b) Ti, (c) O, (d) Se (e) Cd and (f) S. (g) EDS line mapping of the highlighted path in the SEM image and (h) EDS spectrum. The yellow line indicates 21.5 μm of the film thickness.

As proof-of-concept, the as-prepared QDs (CdSe/6CdS, CdSe/Alloy#1, and CdSe/Alloyd #2 QDs) were used as photosensitizer for solar-driven hydrogen generation. The PEC performance is shown in Figure 4.12 (a)-(c). The PEC cells are measured in dark, under continuous and chopped illumination (AM 1.5G, 100 mW/cm^2) by using a typical three electrode configuration with working electrode (QDs based photoanode), Ag/AgCl (saturated with KCl solution) reference electrode and Pt counter electrode. The photocurrent density gradually increases when increasing the applied voltage until the saturated current density is obtained, as shown in Figure 4.12 (a)-(c). A saturated photocurrent density of 6.2 mA/cm^2 is obtained in CdSe/6CdS QDs based photoanode system under one sun illumination. The PEC device based on CdSe/Alloy#1 QDs shows an enhanced saturated photocurrent density of $\sim 15.1 \text{ mA/cm}^2$ which is 2.4 times higher than that of the PEC device based on CdSe/6CdS QDs. In addition, CdSe/Alloy#2 QDs with the gradient alloyed shells exhibit a photocurrent density up to 17.5 mA/cm^2 which is 2.8 times higher than that of the PEC device based on CdSe/6CdS QDs. Here, our PEC cell with

photoanode based on alloyed QDs exhibits a photocurrent density of 17.5 mA/cm² under one sun illumination (AM 1.5 G, 100 mW/cm²). The higher current density can be attributed to several synergistic effects: (i) With the addition of elemental Se in the alloyed QDs, the absorption range is extended towards longer wavelengths, which in turn enhances efficient transfer from photons to excitons. (ii) Benefiting from the gradient band structure of the TiO₂/shell/core, large numbers of both electrons and holes can be extracted from QDs into TiO₂, thereby contributing to the current density. Due to the efficient hole transfer, hole accumulation and oxidation were largely suppressed. (iii) According to charge dynamics analysis, the electrons and holes' spatial separation increases, limiting opportunities for recombination.

Then I calculated the H₂ evolution rate based on the measured saturated photocurrent density, finding 135 mL/cm² per day and 156 mL/cm² per day for CdSe/Alloy#1 QDs and CdSe/Alloy#2 QDs samples, respectively.

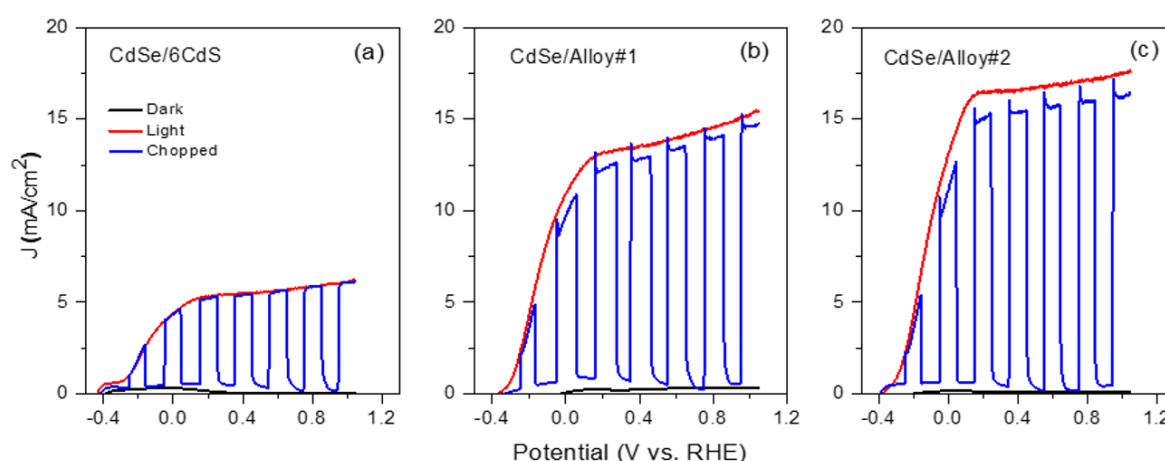


Figure 4.12 Photocurrent density-potential dependence of TiO₂ sensitized by (a) CdSe/6CdS QDs; (b) CdSe/Alloy#1 QDs; (c) CdSe/Alloy#2 QDs in the dark (black curve), under continuous (red curve) and chopped (blue curve) illumination (AM 1.5 G, 100 mW/cm²).

To further investigate the thickness effect of the protective ZnS layers, three and four cycles of SILAR were applied as post-treatment of the photoanodes. The PEC performance was then measured for three and four layers of ZnS coating based on the TiO₂/CdSe/Alloy#2 photoanode, which exhibits a decrease of the photocurrent density with the increase of thickness of ZnS

layers (Figure 4.13). According to the PEC results, too thick ZnS layers will reduce the efficiency of charge transfer which in turn increases the probability of recombination.

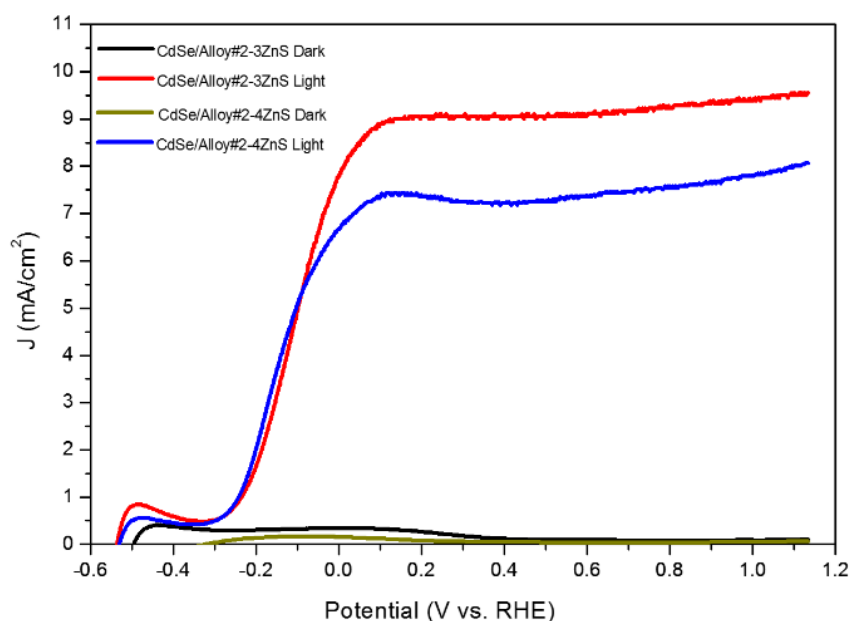


Figure 4.13 Photocurrent density versus bias potential (versus RHE) for $\text{TiO}_2/\text{CdSe}/\text{Alloy}\#2$ with 3 and 4 cycles of ZnS photoanodes in the dark and under continuous illumination (AM 1.5 G, $100 \text{ mW}/\text{cm}^2$).

The stability of the PEC device is also an essential factor for long-term H_2 generation. Stability measurements were conducted under continuous one sun illumination under the bias of 0.6 V vs RHE. Due to the surface traps and instability of QDs inside the alkaline electrolyte during long-term exposure under illumination, the photoanode $\text{CdSe}/\text{Alloy}\#2$ QDs- TiO_2 with two layers of ZnS coating showed a sharp decrease of the current density at the beginning of the stability measurement and maintains only 70 % of the initial photocurrent value of current density after 2 hours measurement (Figure 4.14).

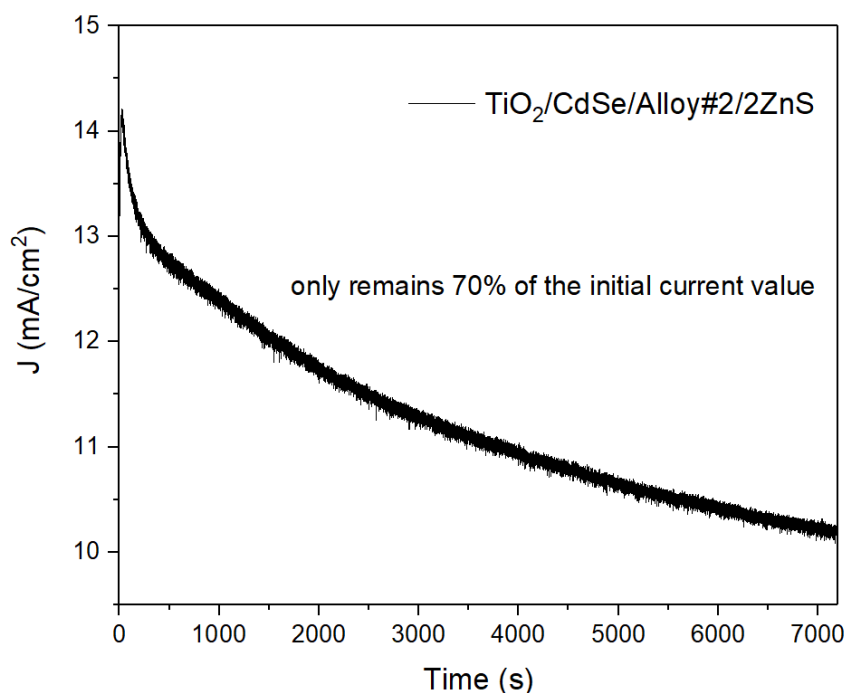


Figure 4.14 Stability spectra of the photoanode based on CdSe/Alloy#2 QDs with 2 cycles of ZnS coating for 2 hours under 0.6 V vs RHE with continuous one sun power.

Multiple approaches were used to optimize the stability performance. Vacuum annealing¹⁰⁷, thicker ZnS shells and SiO₂ coating¹⁰⁸ were observed to improve the stability performance. From Figure 4.15 (a), by comparing 3ZnS samples with and without annealing treatment, the initial photocurrent of the annealed one increased and was found to be more stable over a two-hour measurement period. This observation indicates that annealing is a promising approach to optimize stability. Cycles of two, three and four layers of ZnS coating were conducted to assess the effect of different ZnS thickness. Although the initial current density will decrease with the increase of ZnS cycles (8.8 mA/cm² for the sample with 3 cycles of ZnS coating and 7.2 mA/cm² for the sample with 4 cycles of ZnS coating), similar stability performance shown in the normalized stability spectra (Figure 4.15 (b)) for the thicker ZnS sample was displayed in 2 hours measurement (86 % and 82 % of the initial current density maintained for the samples with 3 and 4 cycles of ZnS coating, respectively). The lower current density values maintained after 2 hours measurement for the sample with 4 cycles of ZnS compared to the one with 3 cycles was attributed to the lower carrier transfer efficiency brought by the thicker shell.

However, the spectra of normalized stability performance (Figure 4.15 (b)) showed a better stability trend for longer-time measurement (more than 2 hours). Afterwards, silica coating was further coated outside the ZnS layers. The sample QDs-TiO₂-2ZnS-SiO₂ showed promising results which simultaneously improved the current density and stability. However, the sample QDs-TiO₂-0ZnS-SiO₂ showed ultra-low current density ($\sim 2 \text{ mA/cm}^2$) which emphasizes the importance of the ZnS coating and shows that direct SiO₂ coating may destroy the QDs because of the strong base (0.01 M ethanolic solution of tetraethylorthosilicate) during the silica coating process. As the three methods for optimizing the stability measurement all showed an enhancement, the sample with the best conditions (annealing, 3 cycles of ZnS coating and SiO₂ coating) was conducted to evaluate the lifetime of the device. As shown in Figure 4.15 (c), after over 39 hours, the device can still work at 50 % of the initial current density value while the sample without SiO₂ coating can operate only for 34 hours at over 50 % of its initial value. Due to the wide bandgap of SiO₂ ($\sim 9 \text{ eV}$)¹⁰⁹, the electrons are largely blocked inside the QDs while the holes can still be extracted by the strong driving force (alkaline electrolyte) where the charge separation can proceed faster. While our PEC cell can maintain 50 % of its initial value as long as 39 hours, indicating it can be a promising candidate for efficient and durable PEC device. In the future, we will continue working on the optimization of stability performance by tailing the thickness of ZnS and SiO₂ shell as well as reducing the hole accumulation.

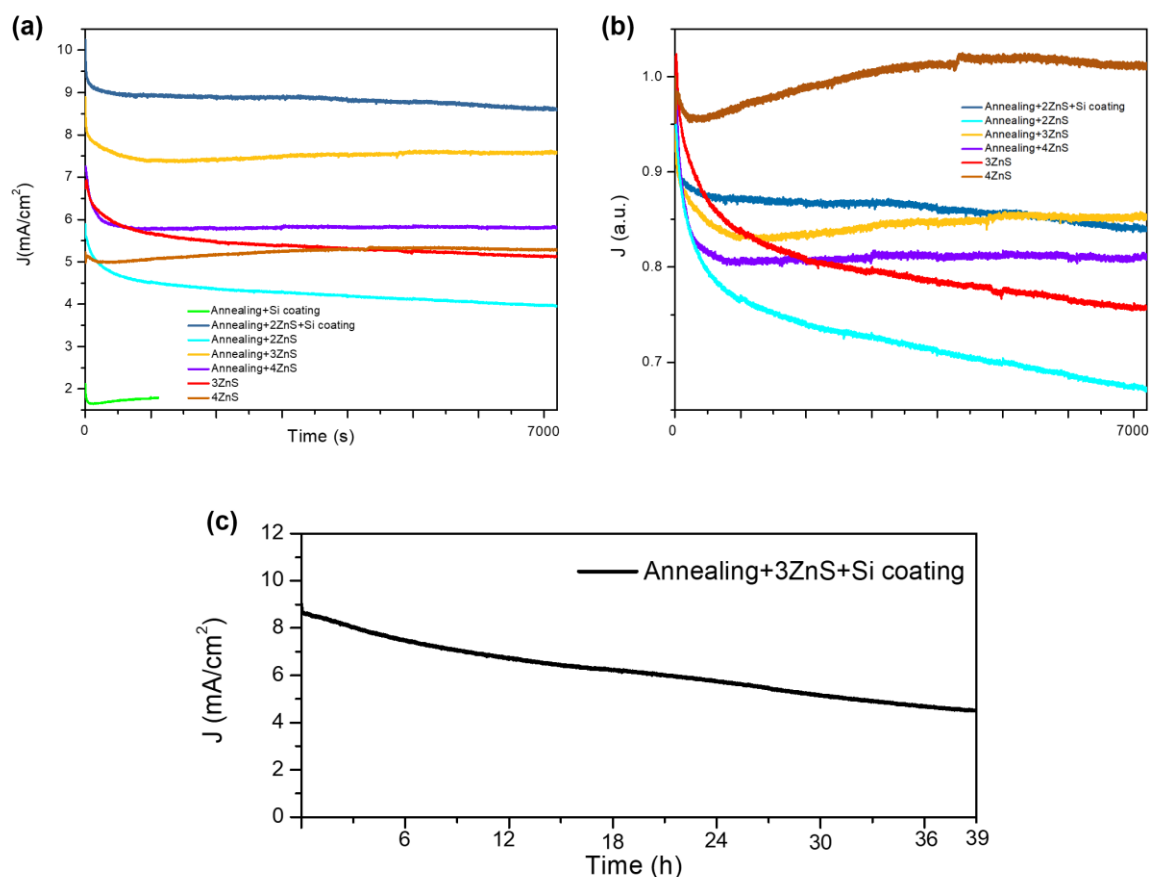


Figure 4.15 Stability measurements (photocurrent density as a function of time) of CdSe/Alloy#2 QDs based photoanode at 0.6 V versus RHE under AM 1.5 G illumination (100 mW/cm²) (a) with different treatment (Annealing, different cycles of ZnS coating and SiO₂ coating) and (b) normalized stability spectra of the sample CdSe/Alloy#2 with different treatment (annealing, different cycles of ZnS coating and SiO₂ coating) (c) with annealing-3ZnS-SiO₂ treatment.

In Table 4.6 and Figure 4.16, with the increasing thickness of ZnS shell, the electron lifetime with ZrO₂ and lifetime with electrolyte are both prolonged due to the thicker ZnS layers. As a result, the hole transfer rate calculated by the previous two values are decreased as the increasing thickness of ZnS layers.

In Figure 4.16, for CdSe/6CdS QDs, the peak position and intensity in PL spectra are almost the same with the different cycles of ZnS, except 0ZnS with electrolyte which may contribute to none protection of ZnS, leading to quenching to QDs of strong alkaline electrolyte. While

for two types of alloyed QDs, the PL peak position will shift obviously as function of different ZnS cycles compared to CdSe/6CdS QDs. This is because the favorable band alignment will increase the mobility of carriers.

Basically, with the increasing of ZnS cycles, or addition of electrolyte, the PL peak will shift to longer wavelength due to more leakage of electrons into shell regions which is consistent with the results in Table 4.6.

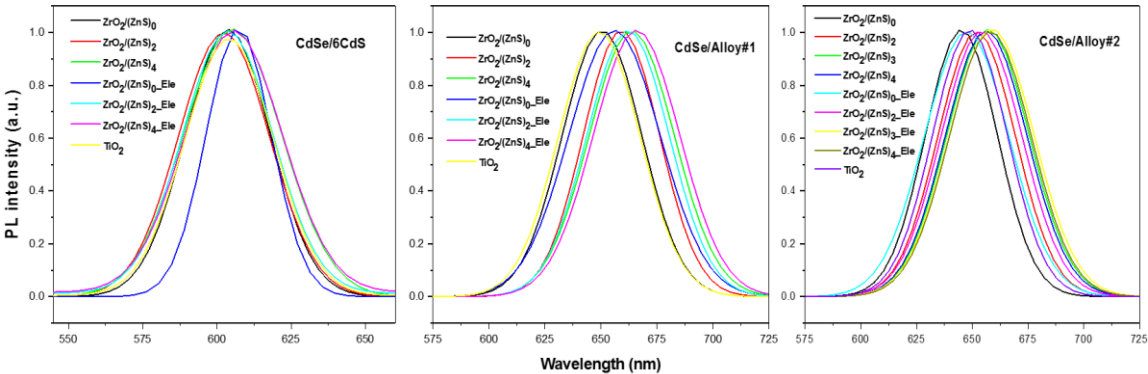


Figure 4.16 PL spectra of CdSe/6CdS, CdSe/Alloy#1 and CdSe/Alloy#2 QDs as function of different cycles of ZnS.

Table 4.6 Lifetime in ZrO₂ with and without electrolyte and corresponding hole transfer rate for CdSe/6CdS, CdSe/Alloy#1 and CdSe/Alloy#2 QDs with different cycles of ZnS coating.

Sample	Lifetime with ZrO ₂ (ns)	Lifetime with electrolyte (ns)	Hole transfer rate K_{ht} (10 ⁷ /s)
CdSe/6CdS-0ZnS	25	8	8.5
CdSe/6CdS-2ZnS	24	10	5.8
CdSe/6CdS-4ZnS	30	10	6.7
CdSe/Alloy#1-0ZnS	22	7	9.7
CdSe/Alloy#1-2ZnS	21	8	7.7
CdSe/Alloy#1-4ZnS	24	10	5.8
CdSe/Alloy#2-0ZnS	23	8	8.2
CdSe/Alloy#2-2ZnS	15	8	5.8
CdSe/Alloy#2-3ZnS	21	11	4.3
CdSe/Alloy#2-4ZnS	20	10	5.0

4.5 Summary

In this chapter, I designed and synthesized two types of alloyed QDs and applied them with TiO₂ as photoanode for PEC hydrogen generation. By engineering the composition of the CdS shell, I obtained a gradient band architecture of core/shell QDs which leads to an improved charge transfer efficiency. As a result, charge recombination is largely suppressed and the photocurrent density of the alloyed QDs based photoanode was largely enhanced (up to 17.5 mA/cm² under one sun power). In addition, extra-long stability was observed for CdSe/Alloy#2 QDs which can maintain 50 % of the initial photocurrent density value for over 39 hours under continuous illumination with multiple post-treatments, indicating a stable, efficient and low-cost photoelectrode for PEC H₂ generation and comparable to the best stability of PEC devices based on colloidal QDs.

Chapter 5 CdSe/CdS/ZnS core/multiple shell QDs for PEC H₂ generation

According to the results in last two chapters, CdSe/CdS and CdSe/CdSe_xS_{1-x}/CdS alloyed QDs could be promising candidates for efficient solar-driven PEC H₂ generation. However, the stability performance of the QDs based photoanodes is not achieving the qualification for large-scale production. Thus, new types of QDs are necessary to be developed for advanced optoelectronic devices with high efficiency and durability.⁶³ To address the issue of poor stability, a general approach is using wide bandgap semiconductors as shells (e.g. ZnS, ZnSe). Such wide bandgap semiconductors can reduce the trap states via passivating the QDs' surface and play a physical barrier for prohibiting the electrons leaking to electrolyte or back into the QDs.^{44,50,51} However, if the shell is too thick (more than 2 nm), such architectures will decrease the carrier transfer efficiency due to unfavorable band alignment. Based on these considerations, core/shell/shell QDs also known as core/multiple-shell QDs have been developed, in which a more efficient carrier transfer can be realized due to a cascade band alignment.^{46,48} Also, core/multiple shell QDs are quite popular due to its adjustable optical properties and high QY. With multiple-shell coating, the QDs surface can be passivated thoroughly, leading to higher fluorescence QY and less non-radiative recombination. Thus, in this chapter, I designed two types of core/multiple shell QDs which in the forms of CdSe/CdS/ZnS QDs (namely CCZ-1 QDs) and CdSe/CdSeS/CdS/ZnCdS/ZnS (namely CCZ-2 QDs) for efficient and stable PEC cell.

5.1 Characterization of QDs

5.1.1 Structure of QDs

Firstly, I used TEM to characterize the as-synthesized QDs. Figure 5.1 (a)-(c) showed the TEM images of the CdSe/6CdS QDs, CCZ-1 QDs and CCZ-2 QDs, respectively. The average size of CdSe/6CdS is 7.35 ± 0.7 nm while the average sizes of CCZ-1 and CCZ-2 QDs are 7.31 ± 0.8 nm and 6.48 ± 0.8 nm, respectively. Due to the same SILAR cycles grown for CdSe/6CdS and CCZ-1 QDs, the overall size of two types of QDs (CdSe/6CdS and CCZ-1 QDs) is similar. The

size of CCZ-2 QDS is smaller than the sizes of both CCZ-1 QDs and CdSe/6CdS QDs, which could be mainly due to cation exchange process occurred during the growth of the CdSe_xS_{1-x} and Cd₇Zn_{1-y}S alloyed shells, leading to the shrink of the CdSe core size. In the insets of Figure 5.1 (a)-(c), the HR-TEM images indicated the (100) crystal plane ($d = 3.74 \text{ \AA}$) of WZ structure of CdSe and (220) plane ($d = 2.06 \text{ \AA}$) of ZB CdS for CdSe/6CdS QDs. The boundary between CdSe core and CdS shell was clearly observed. For CCZ-1 and CCZ-2 QDs, the HR-TEM images revealed that the lattice spacing is 3.36 \AA , corresponding to (111) plane of ZB crystal structure of CdS. The reason for the non-visible boundary between layers for CCZ-1 and CCZ-2 QDs is due to the small lattice mismatch between the gradient layers that our TEM instrument is not able to discern.

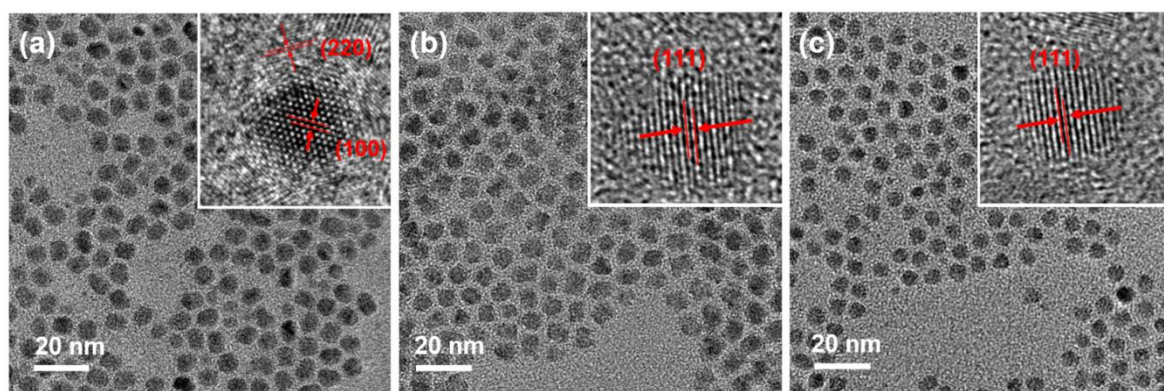


Figure 5.1 TEM images of (a) CdSe/6CdS QDs, (b) CCZ-1 QDs and (c) CCZ-2 QDs where the right corner insets showed the HR-TEM images of corresponding QDs.

Table 5.1 Size parameters of CdSe/6CdS, CCZ-1 and CCZ-2 QDs.

QDs	Diameter of core (nm)	Overall size (nm)
CdSe	3.4	3.4
CdSe/6CdS	3.4	7.35 ± 0.7
CCZ-1	3.4	7.31 ± 0.8
CCZ-2	3.4	6.48 ± 0.8

The SAED images of CCZ-1 and CCZ-2 QDs were exhibited in Figure 5.2, which indicates (002), (110) planes of WZ CdSe, (220) plane of ZB ZnS and (311) plane of ZB CdS.

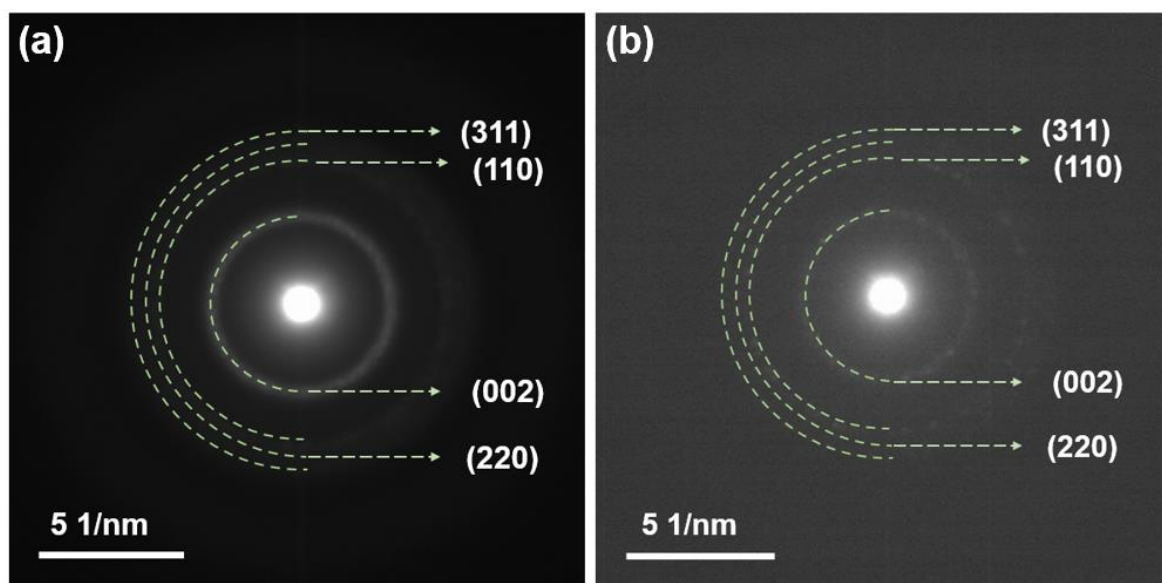


Figure 5.2 SAED pattern of CCZ-1 and CCZ-2 QDs.

To further confirm the crystal structure of as-synthesized QDs, XRD was carried out and the XRD patterns were shown in Figure 5.3. The XRD pattern revealed that the CdSe core has the WZ crystal structure. While for CdSe/6CdS QDs, CdSe ascribes to the WZ crystal structure and CdS refers to ZB crystal structure. For CCZ-1 and CCZ-2 QDs, the CdSe core and CdS shell also attribute to the WZ and ZB crystal structure, respectively, while the ZnS shell refers to ZB crystal structure. The XRD results were consistent with the HR-TEM and SAED results, proving the crystal structure of three types of QDs.

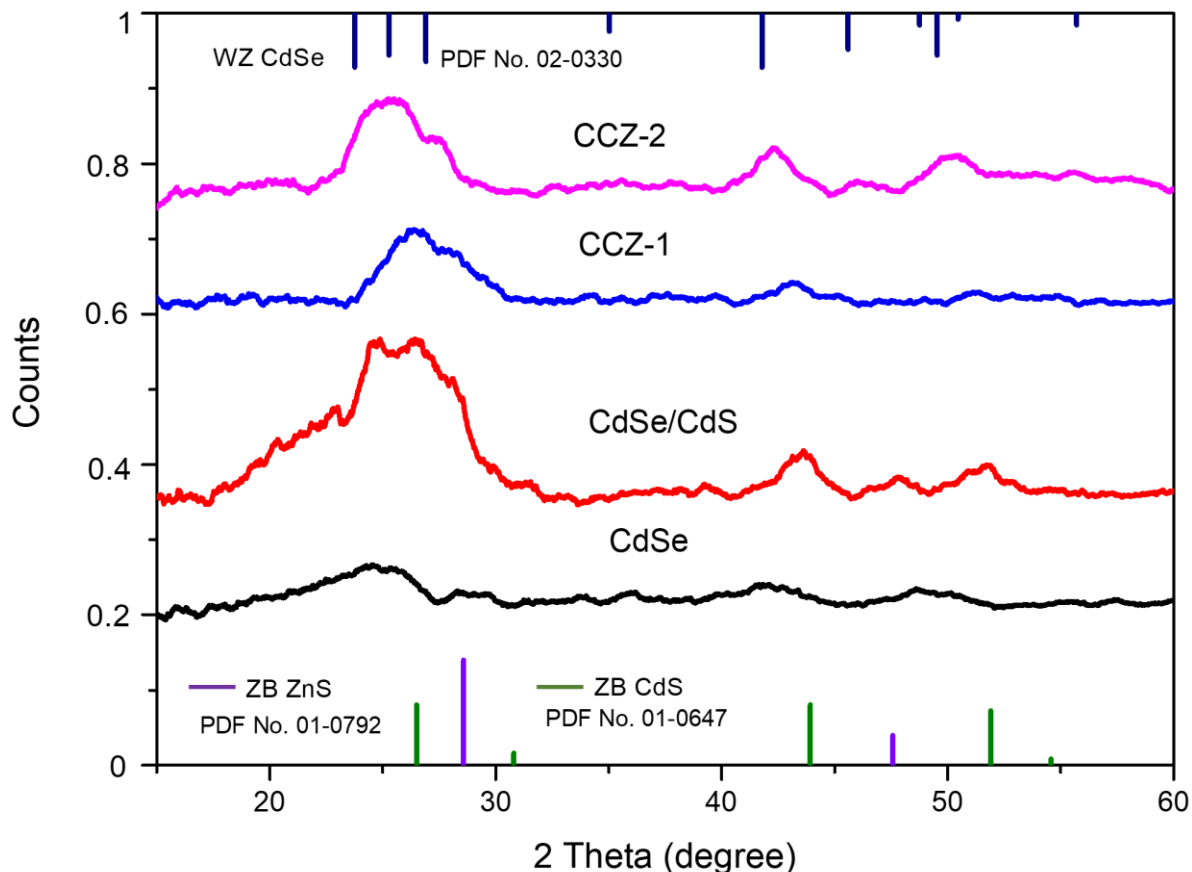


Figure 5.3 XRD pattern of CdSe, CdSe/CdS, CCZ-1 and CCZ-2 QDs. JCPDS card (PDF No. 02-0330, PDF No. 01-0647, PFD No. 01-0792) of WZ CdSe, ZB CdS and ZB ZnS are used for identification.

The high-resolution XPS (Figure 5.4) of small energy regions around the expected peak positions of each element. The binding energies recorded in the XPS analysis were calibrated by referencing the C 1s peak to 284.8 eV. The XPS was carried out to confirm the QDs' composition. In Figure 5.4, the peaks around 403 eV and 411 eV indicated the Cd 3d_{5/2} Cd3d_{3/2}, respectively. The peaks located at 53 eV were assigned to Se3_d while the peaks between 160 eV - 161 eV correspond to S2_p. The peaks located at 1020 eV and 1043 eV were corresponding to Zn 2p_{2/3} and Zn 2p_{1/2}, respectively. In summary, these results demonstrated the existence of element Cd, Se, S, Zn in CCZ-1 QDs

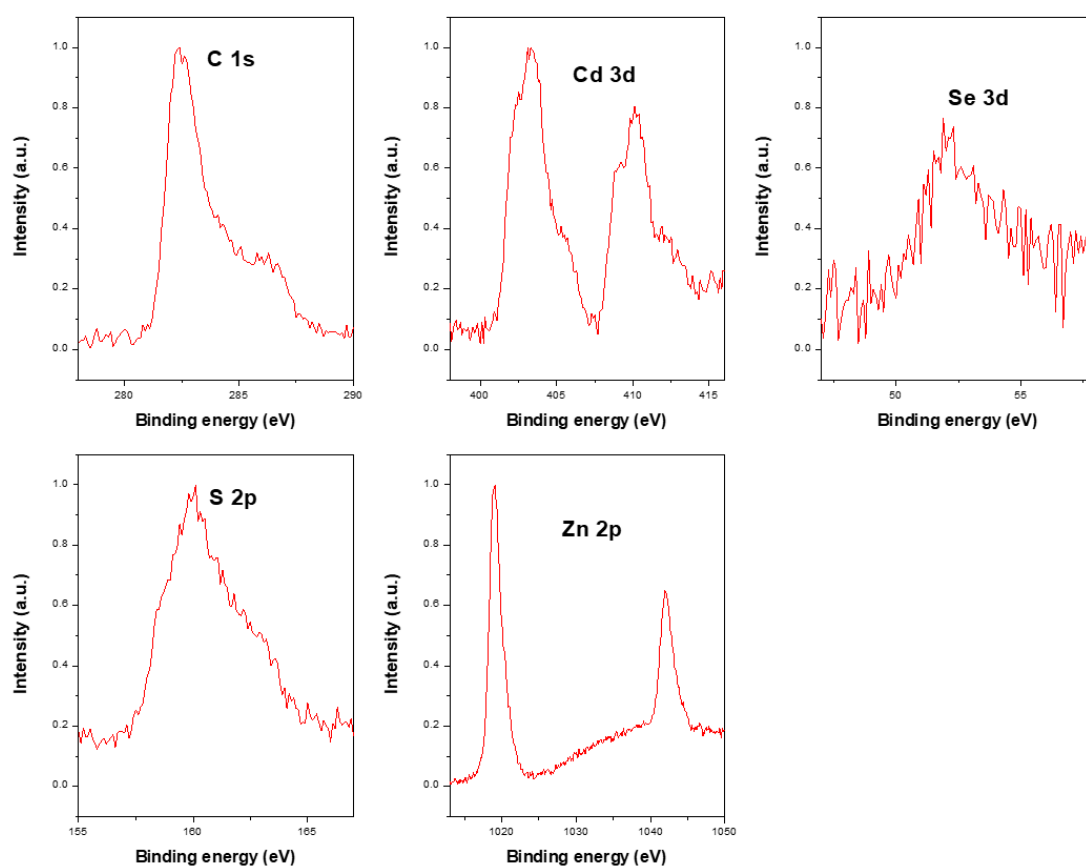


Figure 5.4 High-resolution XPS spectra of Cd 3d, Se 3d, S 2p and Zn 2p in as-prepared CCZ-1 QDs.

5.1.2 Optical properties of QDs

The as-synthesized QDs were investigated by UV-vis absorption and photoluminescence (PL) spectroscopy. As shown in Figure 5.5, the first-excitonic absorption peak was located at 607 nm for CdSe/6CdS QDs. For core/shell/shell QDs, the first-excitonic absorption peaks were located at 616 nm for CCZ-1 QDs and 618 nm for CCZ-2 QDs, respectively. Similarly, the PL spectra also showed the same red-shift phenomenon attributed to the successfully epitaxy growth of CdS and ZnS (or alloyed layers) shells (Figure 5.6).^{110,111}

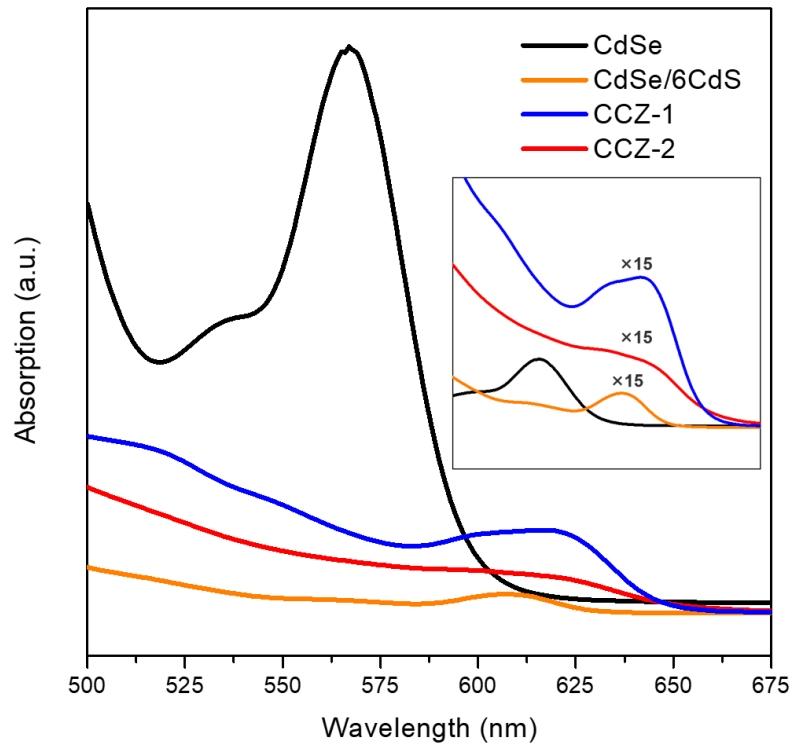


Figure 5.5 The UV-vis absorbance spectrum of CdSe, CdSe/6CdS, CCZ-1 and CCZ-2 QDs (the inset shows the enlarged image of the peaks with the multiple of 15).

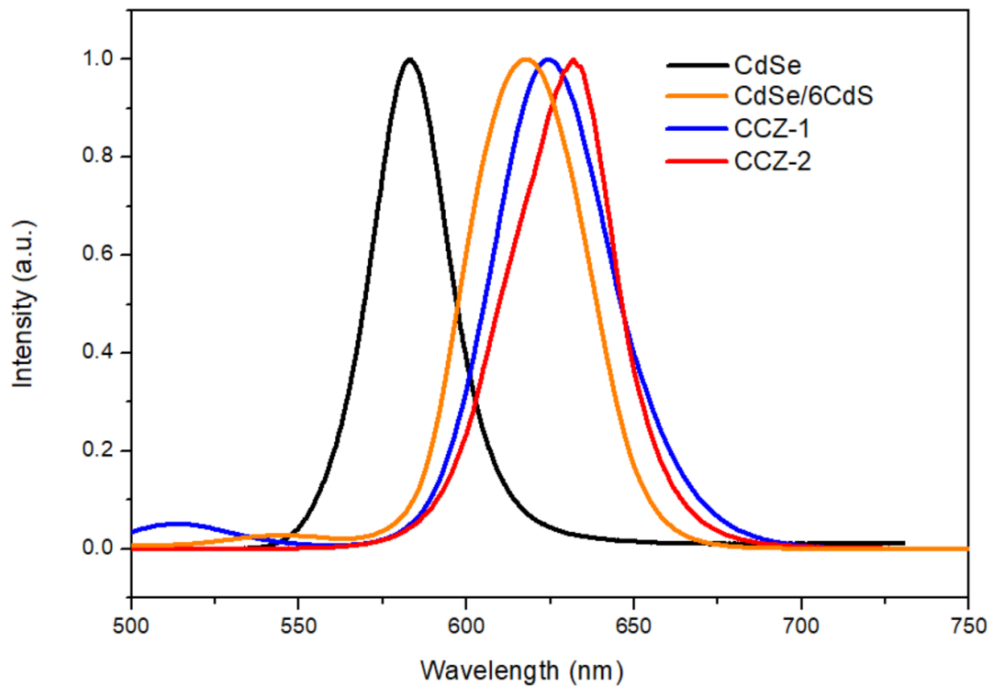


Figure 5.6 PL spectra of CdSe, CdSe/6CdS, CCZ-1 and CCZ-2 QDs.

Table 5.2 Optoelectronic parameters of CdSe/6CdS, CCZ-1 and CCZ-2 QDs.

QDs	Abs peak (nm)	PL peak (nm)
CdSe	567	583
CdSe/6CdS	607	618
CCZ-1	616	625
CCZ-2	618	632

5.2 Carrier dynamics

To further investigate the carrier dynamics of three types of QDs, the QDs with TiO₂ and ZrO₂ mesoporous films with and without electrolyte were carried out to measure the average PL lifetime and accordingly calculated carrier transfer rate. Due to the band alignment between ZrO₂ and QDs, ZrO₂ is used as the benchmark, where the charge injection does not occur and PL degradation can only be attributed to the carrier recombination. The average lifetime τ can be calculated by using the following equation:

$$\langle \tau \rangle = \frac{a_1\tau_1^2 + a_2\tau_2^2 + a_3\tau_3^2}{a_1\tau_1 + a_2\tau_2 + a_3\tau_3} \quad (5.1)$$

The electron/hole transfer rate was calculated based on the average lifetime of QDs on different substrates by referring to the following equations:

$$K(et)/K(ht) = \frac{1}{\langle \tau \rangle_{QDs-TiO_2/ZrO_2} (electrolyte)} - \frac{1}{\langle \tau \rangle_{QDs-ZrO_2}} \quad (5.2)$$

Where K_{et} and K_{ht} are referring to the electron transfer rate and hole transfer rate, respectively. And $\langle \tau \rangle_{QDs-TiO_2}$ and $\langle \tau \rangle_{QDs-ZrO_2}$ are the average lifetime of QDs on the substrates of TiO₂ and ZrO₂ while the $\langle \tau \rangle_{QDs-ZrO_2} (electrolyte)$ represents the average lifetime of QDs-ZrO₂ immersed in the electrolyte. The values of lifetimes and carrier transfer rates are listed in Table 5.3.

Typically, the average PL lifetime of QDs-TiO₂ and QDs-ZrO₂ of CCZ-1 QDs were 14.34 ns and 15.21 ns, respectively, both larger compared to that of the CdSe/6CdS QDs. This result indicated that the ZnS shells serve as the carrier transfer barrier where the electrons and holes were both confined in the CdSe core or CdS shell regions. And the calculated K_{et} and K_{ht} are both decreased compared to that of the CdSe/6CdS QDs which verify the confinement effect provided by the wide-bandgap ZnS shells. For alloyed CCZ-2 QDs, the K_{et} is 9 times larger than that of CCZ-1 QDs while the K_{ht} value is 9.3 times larger than that of CCZ-1 QDs, respectively. This phenomenon indicated that band alignment was optimized by the intermediate alloyed layers which built a favorable band structure for the carriers to separate and transfer, leading to fewer charge recombination.^{42,103}

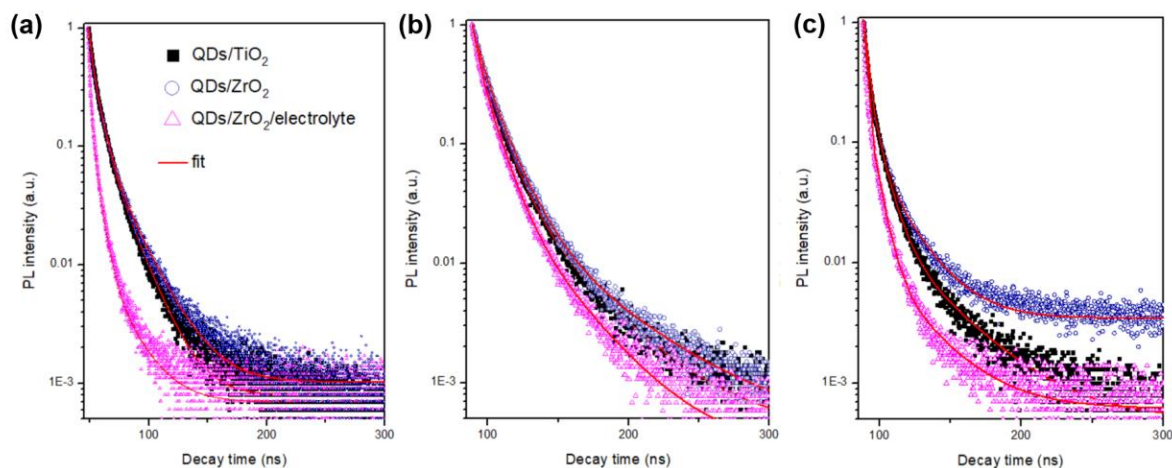


Figure 5.7 PL decay spectra of CdSe/6CdS, CCZ-1 and CCZ-2 QDs after deposited into TiO₂ films, ZrO₂ films and ZrO₂ films in the presence of an electrolyte.

Table 5.3 Lifetime with different substrates and charge transfer rate.

QDs	Lifetime with TiO ₂ (ns)	Lifetime with ZrO ₂ (ns)	Lifetime with ZrO ₂ in electrolyte (ns)	Electron transfer rate (10 ⁷ s ⁻¹)	Hole transfer rate (10 ⁷ s ⁻¹)
CdSe/6CdS	9.94	10.8	4.24	0.8	14.3
CCZ-1	14.34	15.21	11.43	0.4	2.2
CCZ-2	7.03	9.45	3.23	3.6	20.4

5.3 Theoretical calculation

To further verify the process of the carrier dissociation, we calculated the theoretical electron-hole wave functions by solving stationary Schrödinger equation in spherical geometry. The calculated spatial probability distribution [$\rho(r)$] of electron wave function $\psi_e(r)$ and hole wave function $\psi_h(r)$ as a function of QDs radius (nm) were shown in Figure 5.8. The dashed lines indicated the peak position of functions. When compared to CdSe/6CdS core/shell QDs, both $\psi_e(r)$ and $\psi_h(r)$ of CCZ-1 QDs showed a fewer carrier leakage according to the left-shift of the dashed lines. This result was consistent with the former demonstration that the confinement effect brought by the ZnS shells. For alloyed CCZ-2 QDs, $\psi_e(r)$ and $\psi_h(r)$ show that enhanced carrier leakage due to the right-shift of the dashed lines when compared to CdSe/6CdS and CCZ-1 QDs. This phenomenon also provided the evidence that the band alignment was optimized via band engineering through adding alloyed layers. The e-h overlapping area increased from 62 % for CdSe/6CdS QDs to 67 % for CCZ-1 QDs due to the enhancement of confinement. And the e-h overlapping area value of CCZ-2 QDs further increased up to 70 % because the electron and hole transfer efficiency were improved so both electrons and holes have more probability to leak to the shell regions.

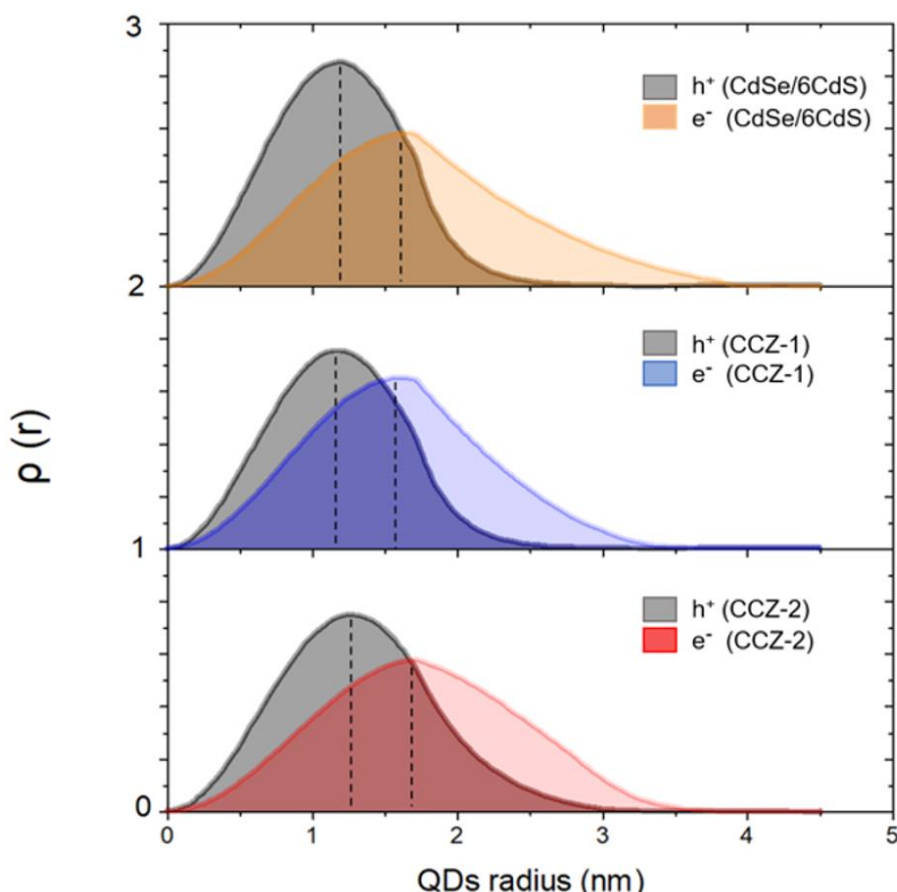


Figure 5.8 Spatial probability distribution value $\rho(r)$ of electrons and holes as a function of QD radius (nm) for CdSe/6CdS, CCZ-1 and CCZ-2 QDs (dashed lines show the positions of the peaks).

5.4 PEC and stability performance

Generally, upon the solar irradiation, the electron and hole pairs will generate from photo excitons and dissociate at the QDs/TiO₂ interfaces. The electrons will transfer from the CdSe core to CdS shell for CdSe/6CdS core/shell QDs while the electrons will further leak out into ZnS shell region for CCZ-1 and CCZ-2 QDs. Afterwards, the electrons will be injected into TiO₂ due to electronic band bending and then be transferred to counter-electrode (Pt) through the FTO and outside circuit to produce H₂. Meanwhile, the holes will be extracted from QDs to the Na₂S/Na₂SO₃ electrolyte (pH ~ 13) which serves as the hole scavengers. Figure 5.9 (a) showed the schematic diagram of CCZ-1 QDs/TiO₂ based photoanode, indicating the band gap and band position of CdSe, CdS and ZnS.^{32,106,112} According to the previous reports, the

CdSe/6CdS forms the band alignment of Quasi-Type II core/shell architecture where the electrons can leak from CdSe core to CdS shell. However, due to large conduction band offset between CdS and ZnS, the electrons will be confined in the CdSe core and CdS shell regions. While the holes still can be extracted to the electrolyte due to strong driving force provided by the alkaline electrolyte (pH \sim 13) which means that the carrier spatial separation is more efficient. The Figure 5.9 (b) showed the schematic diagram of CCZ-2 QDs based photoanode for PEC H₂ generation. The difference between the CCZ-2 and CCZ-1 QDs is the additional intermediate layers CdSe_xS_{1-x} between CdSe and CdS for CCZ-2 and Cd_yZn_{1-y}S between CdS and ZnS for CCZ-1. Such intermediate layers can increase the carrier transfer efficiency by not only reducing the energy barriers (band offset) between two semiconductor materials, but also reducing the lattice mismatch at the interfaces. Thus, the recombination can be reduced due to more efficient carrier separation as well as fewer defects at the interfaces. Moreover, such structure also has the advantage of passivating the QDs surface via coating of wide bandgap semiconductors, leading to fewer non-radiative recombination centers on the surface of QDs.

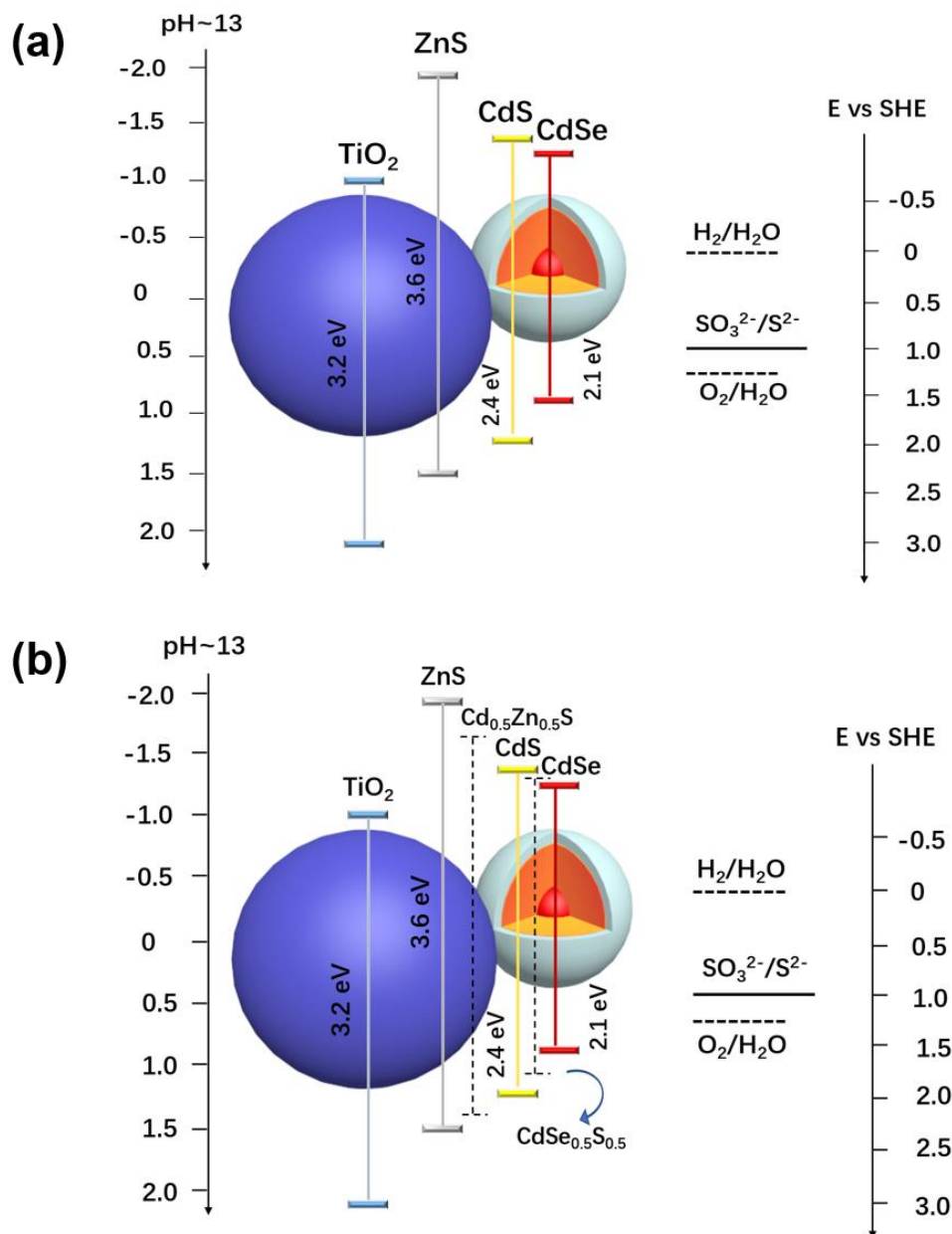


Figure 5.9 Schematic diagram of the band structure and carrier transition of (a) the CCZ-1 (b) CCZ-2 QDs based photoanode. Approximate energy levels of TiO₂ and QDs, together with related characteristic redox potentials.

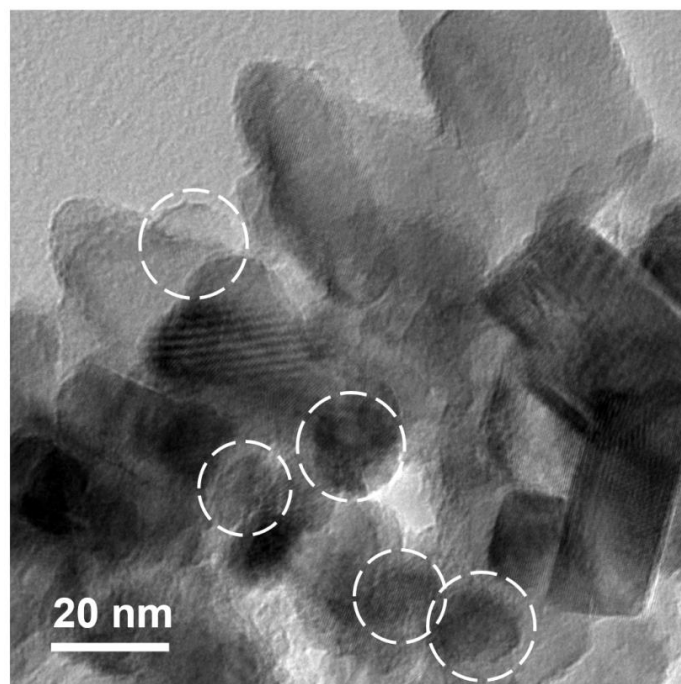


Figure 5.10 TEM image of CCZ-2 QDs in the mesoporous TiO₂ film (white circles indicate the position of QDs).

As shown on Figure 5.10, the CCZ-2 QDs were deposited on the surface of TiO₂ in the TEM image. The white circles indicated the position of as-synthesized QDs. The morphology of QDs is spherical which is consistent with QDs before EPD process which reveals that the EPD will not change the QDs by high voltage (200 V). Figure 5.11 showed the SEM image of QDs/TiO₂ photoanode in a cross-sectional view and the accordingly EDS mapping was shown of certain area. The SEM image showed that the thickness of the film is around 20 μm. Also, the signal of element Ti, O, Cd, Zn, Se, and S were captured in the as-prepared QDs/TiO₂ photoanode.

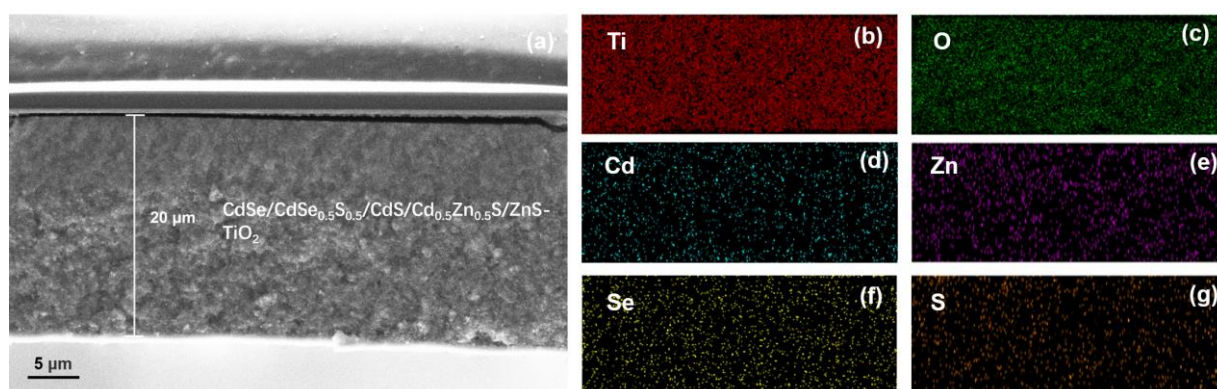


Figure 5.11 (a) Cross-sectional SEM image of CdSe/CdSe_{0.5}S_{0.5}/CdS/Cd_{0.5}Zn_{0.5}S/ZnS QD-sensitized photoanode and relevant EDS 2D mapping of all the elements including b) Ti, c) O, d) Cd, e) Zn, f) Se, g) S. And the white line indicates the thickness is 20 μm of the film.

As a proof of concept, the as-prepared three types of the QDs as the light harvesters were applied for PEC H₂ generation. Firstly, the QDs were deposited onto mesoporous TiO₂ films through EPD for 2 hours under the voltage of 200 V. Afterwards, 2 SILAR cycles of ligand exchange and 2 cycles of passivation ZnS capping were conducted prior to the PEC measurement. The PEC activity of the QDs/TiO₂ photoanode system towards the H₂ generation reaction was evaluated in a three-electrode configuration with 0.25 M Na₂S and 0.35 M Na₂SO₃ as hole scavengers. All the PEC and stability measurement were carried out under a simulated sun irradiation (AM 1.5 G 100 mW cm⁻²). Pt sheet was used as the counter electrode and Ag/AgCl electrode was used as the reference electrode. A set of linear-sweep voltammograms was conducted by using different photoanodes in the dark and under continuous solar illumination. With the increasing voltage, the saturated current density was obtained for three types of QDs based photoanodes. Figure 5.12 showed the photocurrent density-potential dependence of TiO₂ sensitized with CdSe/6CdS QDs CCZ-1 QDs and CCZ-2 QDs in the dark and under continuous illumination (AM 1.5 G, 100 mW cm⁻²). The CdSe/6CdS based photoanode displayed a saturated photocurrent density of 12.6 mA/cm². For CCZ-1 QDs, the photoanode can achieve the saturated photocurrent density of 14.2 mA/cm². The increased photocurrent density compared to CdSe/6CdS based photoanode can be mainly due to the enhancement of the absorption as well as the surface passivation effect provided by the ZnS shells. As a result, the surface traps are largely suppressed and fewer non-radiative recombination happened on the QDs surface. Furthermore, the photocurrent density of the photoanode based on the alloyed CCZ-2 QDs reaches as high as 20.5 mA/cm² which is significant improved compared to other two types of QDs. Thanks to the alloyed shells, the energy barrier between the different semiconductor materials (CdSe, CdS and ZnS) was significantly reduced, leading to more efficient carrier transfer. At the same time, the alloyed shells also have the passivation effect that the surface defects can be suppressed accordingly.

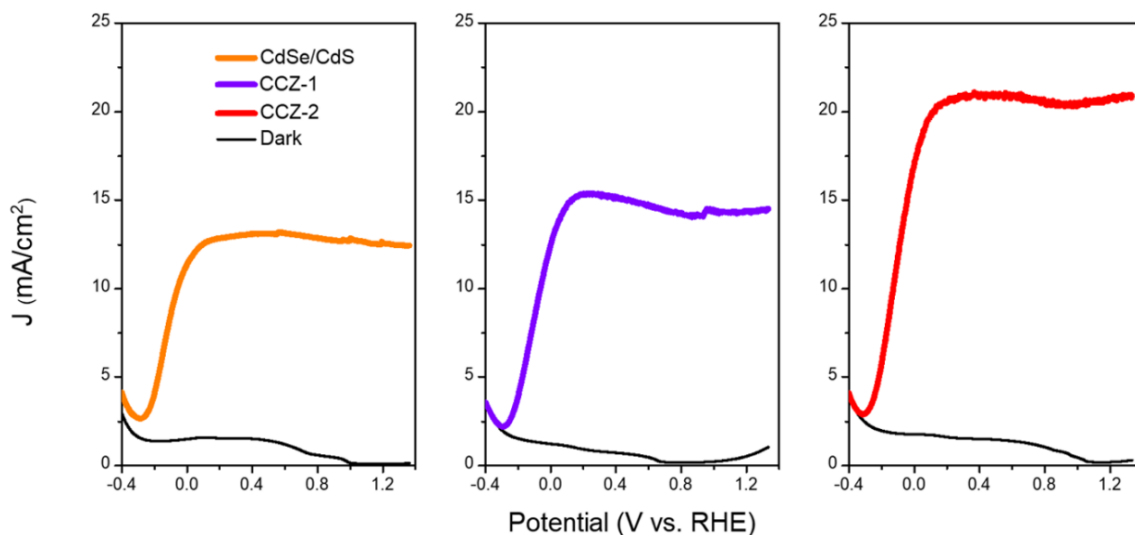


Figure 5.12 Photocurrent density-potential dependence of TiO₂ sensitized with CdSe/6CdS QDs, CCZ-1 QDs and CCZ-2 QDs in the dark (black curve), and under continuous (chromatic curve) illumination (AM 1.5 G, 100 mW cm⁻²).

The long-term stability performance is another critical factor for application of the PEC H₂ evolution. Typically, the stability was investigated under continuous one sun illumination at 0.6 V vs. RHE. Figure 5.13 showed that the photocurrent density for CdSe/6CdS QDs, CdSe/4CdS/2ZnS QDs and CdSe/(CdSe_xS_{1-x})₃/CdS/Cd_yZn_{1-y}S/ZnS QDs under continuous one sun illumination for 2 hours. According to the Figure 5.13, ~55 % of the initial photocurrent density value was maintained for CdSe/6CdS QDs based photoanode. For two types of core/multiple-shell QDs, ~84 % of the initial photocurrent density value was observed for CCZ-1 QDs based photoanode after 2 hours illumination while an unprecedented stability performance was achieved for alloyed CCZ-2 QDs based photoanode, with retention of ~93.4 % of the initial photocurrent value after 2-hour continuous illumination (100 mW/cm²). The outstanding stability performance can be mainly because the alloyed intermediate layers act as fast pathways for carrier transfer. As a result, the hole accumulation is largely reduced in the valence band, leading to fewer photo-oxidation of the photoanodes. Moreover, the ZnS (or alloyed layers) also play an important role of passivating the QDs surface. Thus, the recombination caused by the surface traps and defects can be dramatically suppressed.

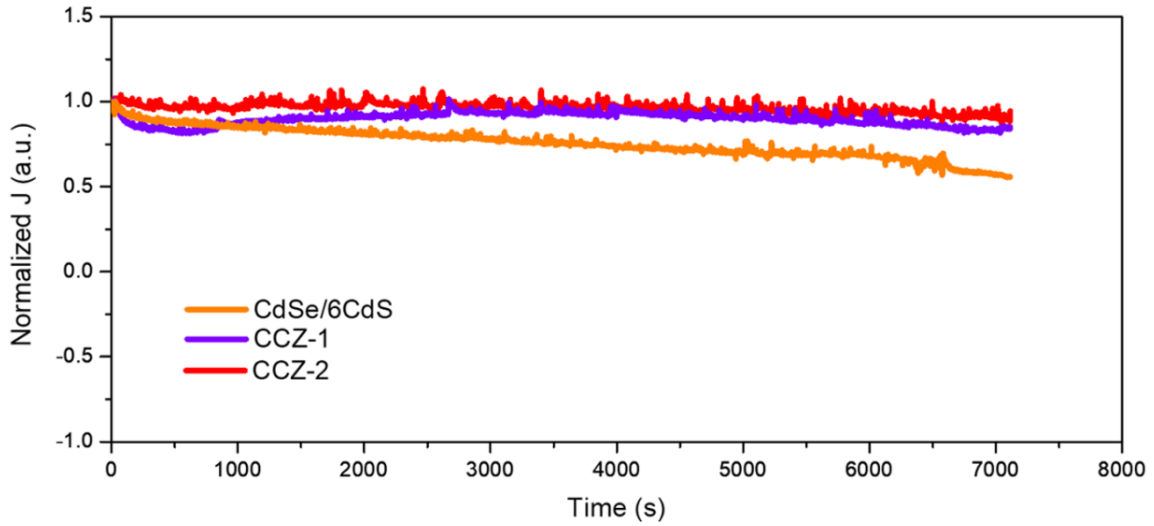


Figure 5.13 Stability measurements (photocurrent density as a function of time) of the CdSe/6CdS QDs, CCZ-1 QDs and CCZ-2 QDs based photoanode at 0.6 V versus RHE under AM 1.5 G illumination (100 mW cm^{-2}) with 2 ZnS coating.

Finally, to estimate the evolved H_2 volume in real condition based on as-synthesized QDs, a gas chromatograph system was further carried out together with J - t curves to compare the produced H_2 with calculated H_2 volume. As shown in Fig. 5.14, the calculated H_2 volume and measured H_2 volume are shown. Then the Faradaic efficiency (FE) can be roughly calculated according to the equation below where $\sim 80\%$ of the η_{FE} was obtained within 60 min PEC operation.

$$\text{Faradaic efficiency } (\eta_{\text{FE}}) = \frac{V_{\text{measured gas}}}{V_{\text{calculated gas}}} \quad (5.3)$$

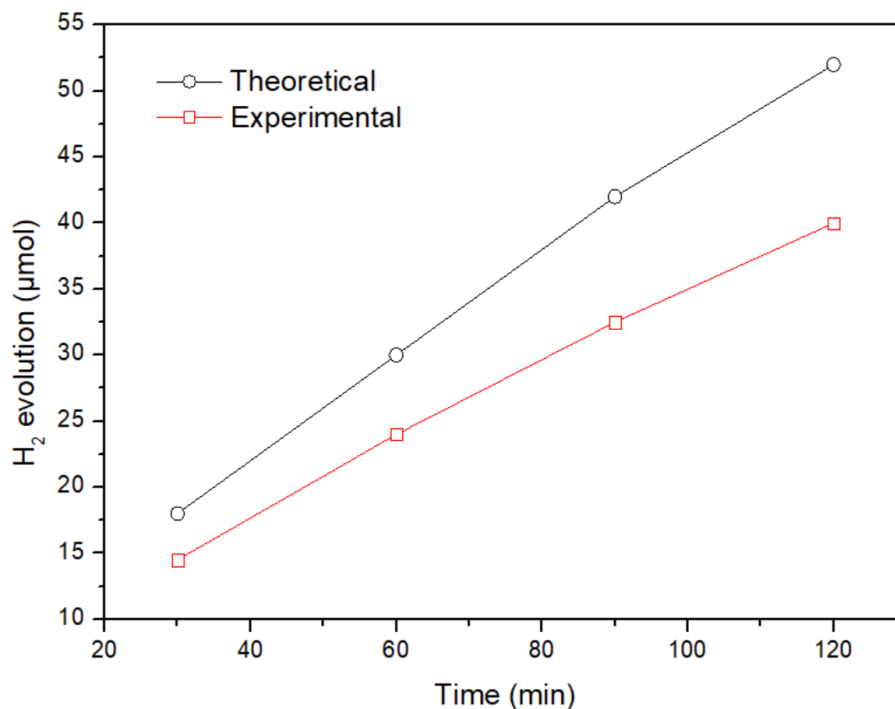


Figure 5.14 Theoretical and experimental H₂ evolution of CCZ-2 QDs/TiO₂ photoanodes during 120 min under one sun illumination (AM 1.5 G, 100 mW/cm²) with a bias of 0.6 V vs RHE.

5.5 The thickness impact of ZnS shell

I further investigated the thickness effect of ZnS shells on overall core/multiple shell QDs for PEC performance. As known, on one hand, wide bandgap semiconductors such as ZnS can reduce the trap states and defects on the QDs' surface, improving the optoelectronic properties. On the other hand, the wide bandgap shells also act as a barrier inhibiting the electron injection to the metal oxide. Thus, it is critical to investigate the ZnS shell thickness effect on PEC devices for which can not only passivate the surface, but also facilitate the electron injection.¹¹³ For this reason, CdSe/4CdS QDs capped with different ZnS thickness (1-3 monolayer) were designed and synthesized via a SILAR method.

According to Figure 5.15, TEM images showed that the size of QDs increased with thicker ZnS shells. Typically, the diameter of QDs with different ZnS shell thickness was 7.02 ± 0.9 nm for CdSe/4CdS/ZnS QDs, 7.31 ± 0.8 nm for CdSe/4CdS/2ZnS QDs and 7.74 ± 1 nm for

CdSe/4CdS/3ZnS QDs, respectively. These values of QDs size indicated that the ZnS shells were successfully grown on the CdS surface through SILAR method. Figure 5.16 showed the absorption spectra of CdSe/4CdS/ZnS QDs, CdSe/4CdS/2ZnS QDs and CdSe/4CdS/3ZnS QDs which the first-excitonic absorption peaks were located at 591 nm, 601 nm and 603 nm, respectively. These results revealed that a minor red-shift brought by thicker ZnS shells which was consistent with the former results.

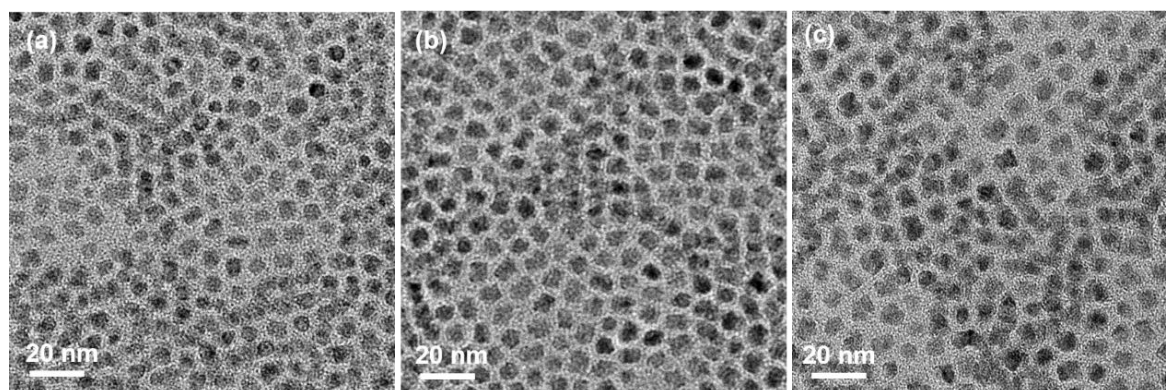


Figure 5.15 TEM images of CdSe/4CdS/ZnS, CdSe/4CdS/2ZnS and CdSe/4CdS/3ZnS QDs with different thickness of ZnS shells.

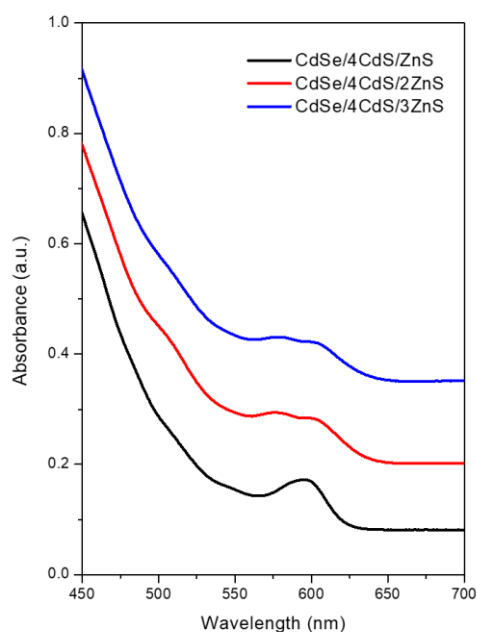


Figure 5.16 Absorption spectra of CdSe/4CdS/ZnS, CdSe/4CdS/2ZnS and CdSe/4CdS/3ZnS QDs.

Then I further investigated the carrier dynamic behavior of three types of QDs. Figure 5.17 showed the average PL lifetime of three QDs in toluene where the average lifetime was prolonged from 22.04 ns for CdSe/4CdS/ZnS QDs to 24.77 ns for CdSe/4CdS/2ZnS QDs, then further increasing to 25 ns for CdSe/4CdS/3ZnS QDs. The prolonged lifetime results demonstrated that a stronger confinement effect occurred with thicker ZnS shells. Figure 5.18 was the PL spectra of three QDs after deposited onto TiO₂, ZrO₂ and ZrO₂ with the presence of electrolyte. According to the Figure 5.18 and the Table 5.5, the average electron lifetime with ZrO₂ increased from 19.79 ns for CdSe/4CdS/ZnS QDs to 27.91 ns for CdSe/4CdS/2ZnS QDs and 26.31 ns for CdSe/4CdS/3ZnS QD, respectively. These results shown in Table 5.4 verified the stronger confinement of electrons with thicker ZnS shells. For the calculated electron and hole transfer rate, K_{et} were both $1.56 \times 10^7 \text{ s}^{-1}$ for the CdSe/4CdS/2ZnS QDs and CdSe/4CdS/3ZnS QDs, which was faster than the K_{et} of CdSe/4CdS/ZnS QDs. The similar phenomenon was observed for the hole transfer rate. The K_{ht} were both $2.64 \times 10^7 \text{ s}^{-1}$ for CdSe/4CdS/2ZnS QDs and CdSe/4CdS/3ZnS QDs, higher than that of CdSe/4CdS/ZnS QDs.

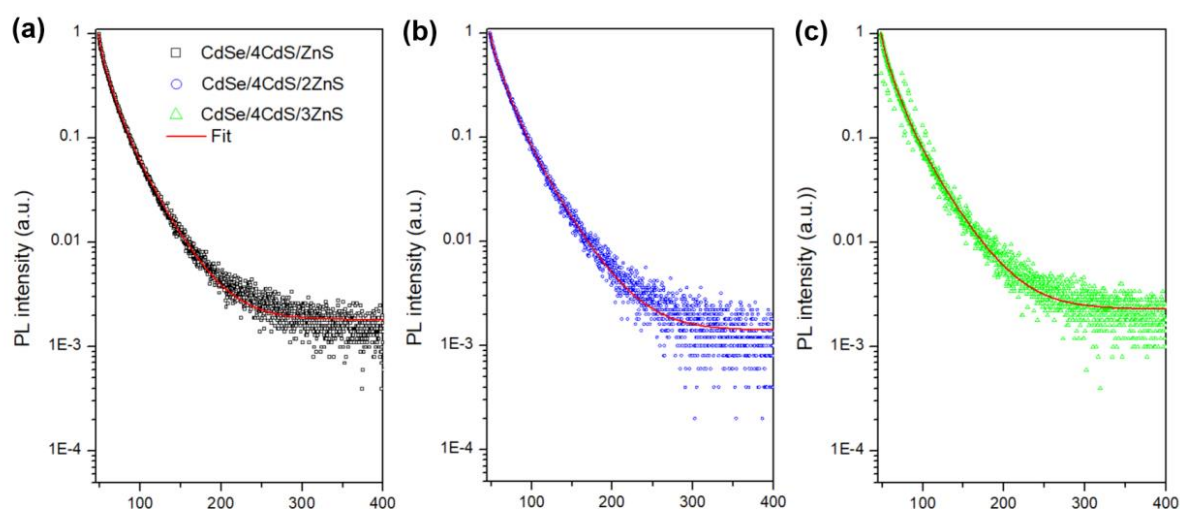


Figure 5.17 PL decay spectra of CdSe/4CdS/ZnS QDs, CdSe/4CdS/2ZnS QDs and CdSe/4CdS/3ZnS QDs in the toluene. The dots are measured data and red lines represent fitting curves.

Table 5.4 Lifetime in toluene of CdSe/4CdS/ZnS, CdSe/4CdS/2ZnS and CdSe/4CdS/3ZnS QDs.

QDs	Lifetime in Toluene (ns)
CdSe/4CdS/ZnS	22.04
CdSe/4CdS/2ZnS	24.77
CdSe/4CdS/3ZnS	25.00

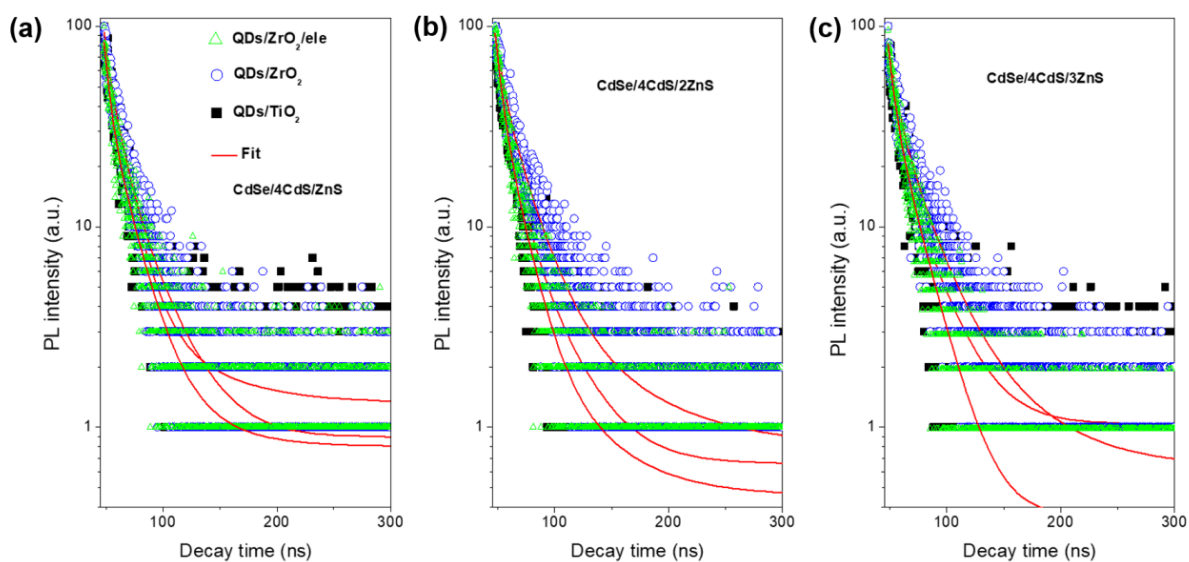


Figure 5.18 PL spectra of CdSe/4CdS/ZnS QDs, CdSe/4CdS/2ZnS QDs and CdSe/4CdS/3ZnS QDs after deposited into TiO₂ films, ZrO₂ films and ZrO₂ films in the presence of an electrolyte. The dots are measured data and red lines represent fitting curves.

Table 5.5 Lifetime with different substrates and charge transfer rate.

QDs	Lifetime with TiO ₂ (ns)	Lifetime with ZrO ₂ (ns)	Lifetime with ZrO ₂ in electrolyte (ns)	Electron transfer rate (10 ⁷ s ⁻¹)	Hole transfer rate (10 ⁷ s ⁻¹)
CdSe/4CdS/ ZnS	19.60	19.79	16.68	0.1	1
CdSe/4CdS/ 2ZnS	18.88	27.91	16.70	1.56	2.64
CdSe/4CdS/ 3ZnS	18.64	26.31	15.54	1.56	2.64

Finally, I applied three types of QDs with mesoporous TiO₂ for the PEC measurement. According to Figure 5.19, the saturated photocurrent density of three QDs were 12.5 mA/cm² for CdSe/4CdS/ZnS QDs, 14.2 mA/cm² for CdSe/4CdS/2ZnS QDs and 8.6 mA/cm² for CdSe/4CdS/3ZnS QDs, respectively. The PEC measurement results indicated that the 2 SILAR cycles of ZnS shells was the optimized shell thickness for both surface passivation effect and facilitating the carrier transfer. In other words, 1 monolayer of ZnS shell was too thin for passivating the surface while 3 monolayers of ZnS shell were too thick for the electron/hole injection from QDs to TiO₂ which the “over-confinement” occurs. As a result, more unfavorable non-recombination will happen in the region of ZnS shells. Thus, 2 ZnS monolayers were proved to be the optimized shell thickness for PEC device, leading to a higher saturated photocurrent density of 14.2 mA/cm².

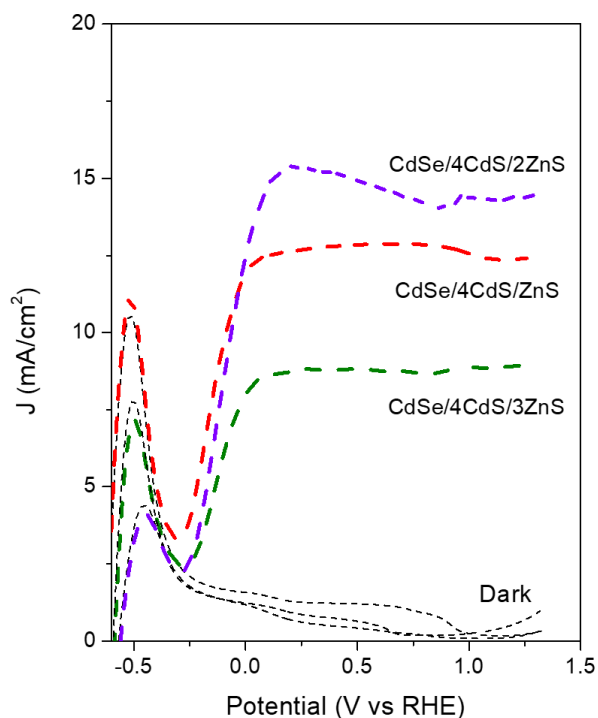


Figure 5.19 Photocurrent density-potential dependence of TiO₂ sensitized with (a) CdSe/4CdS/ZnS QDs, CdSe/4CdS/2ZnS QDs; and CdSe/4CdS/3ZnS QDs in the dark (black dashed curves), and under continuous illumination (AM 1.5 G, 100 mW cm⁻²).

Then I compared the saturated photocurrent density as well as the stability performance based on CCZ-2 QDs with pioneer works. In the literatures, several works reported colloidal QDs based photoanodes for PEC H₂ generation. Some typical results were listed in Table 5.6 for comparison. In this work, I focused on improving the photocurrent density as well as long-term stability performance. To the best of our knowledge, the highest photocurrent density based on colloidal QDs was 17.5 mA/cm² while 22.1 mA/cm² based on in-situ QDs^{114,115}. Here, the CCZ-2 alloyed QDs based photoanode can achieve a J_{ph} as high as 20.5 mA/cm² under one illumination. More importantly, there are few works focusing on improving the stability performance of colloidal QDs based anode which is crucial for developing a robust technology for H₂ evolution from water. In Table 5.6, the 2-hour value was used as reference as it is the most common value reported for stability performance. So far, few studies reported over 90 % of the initial value of the photocurrent density. Basu⁸⁰ reported an unprecedented stability performance of 96 % after 2-hour measurement, but with a low photocurrent density of 4.7

mA/cm². Similarly, Adhikari⁴³ reported a photoanode of CdSe/CdS/Pb_xCd_{1-x}S/CdS/TiO₂ with retention of 94.9 % of the initial photocurrent value of 8 mA/cm² after 2 hours. To summarize, the alloyed CCZ-2 QDs based photoanode not only achieves an extremely high photocurrent density, but also maintains one of the best stability performances among all colloidal QDs based photoanodes.

Table 5.6 Previous work of colloidal QDs based photoanode for PEC H₂ generation.

QDs	Metal oxide	Electrolyte	Saturated photocurrent density (mA/cm ²)	Stability performance
PbS/CdS	TiO ₂	Na ₂ S/Na ₂ SO ₃	11.2	70 % after 2h
CdS/CdSe	TiO ₂	Na ₂ S/Na ₂ SO ₃	16	83 % after 4h
CdSe/Pb _x Cd _{1-x} S/CdS	TiO ₂	Na ₂ S/Na ₂ SO ₃	8	94.9 % after 2h
CdSe/CdSe _x S _{1-x} /CdS	TiO ₂	Na ₂ S/Na ₂ SO ₃	17.5	~70 % after 2h
CdSe/CdS	SnO ₂	Na ₂ S/Na ₂ SO ₃	4.7	96 % after 2h
CdSe/CdSe _x S _{1-x} /CdS/Cd _y Zn _{1-y} S/ZnS	TiO ₂	Na ₂ S/Na ₂ SO ₃	20.5	93.4 % after 2h

5.6 Summary

In summary, I reported two types of core/multiple-shell QDs, CCZ-1 and alloy CCZ-2 QDs for

efficient and stable PEC H₂ generation. Based on Quasi-type II CdSe/CdS core/shell QDs, wide bandgap semiconductor ZnS shell was coated to form the core/shell/shell architecture, providing a cascade Type I band alignment for surface passivation as well as efficient carrier transfer. As a result, the saturated photocurrent density based on CCZ-1 QDs can reach as high as 14.2 mA/cm². Based on CCZ-1 core/shell/shell QDs structure, an optimized gradient band alignment was built by adding intermediate alloyed layers. An unprecedented saturated photocurrent density of 20.5 mA/cm² was achieved based on alloyed CCZ-2 QDs under one sun illumination which is the record based on all colloidal QDs based photoanodes. More importantly, a promising stability performance of 93.4 % of the initial photocurrent density was maintained after 2-hour continuous illumination. The main reason for the significant improvement of the PEC and stability performance is the surface passivation provided by the wide bandgap ZnS shell. Furthermore, the alloyed layers provide a short pathway for carriers to transfer more efficiently so the unfavorable recombination events can be dramatically suppressed. These results indicated that the alloyed core/multiple-shell QDs can be a promising photoanode candidate for both highly efficient and stable H₂ generation devices. Future direction will be concentrated on optimizing the core size, alloyed shell thickness and composition for improvement of PEC devices.

Chapter 6 Conclusions and persp

6.1 Conclusions

Colloidal QDs have many superior properties for PEC H₂ generation. Colloidal CdSe QDs have attracted much attention due to their unique size-dependent photophysical properties that are distinctly different from corresponding bulk materials, in the UV and visible range. They are currently exploited for various applications, such as solar energy conversion, light emitting. In particular, in the field of solar energy conversion, the cost and absorption efficiency up-to-date make the QDs as promising light harvester candidates. The carrier separation and transfer efficiency are still one of the huge problems for improving the performance of optoelectronic devices. Moreover, the mechanism behind it still needs to be well understood. For the real application of QDs based optoelectronic devices, the stability performance is still the main obstacles to be addressed. In my thesis, I introduced some strategies for improving the PEC and stability performance via band engineering approaching, either optimized the shell thickness/composition or size of QDs.

In chapter 3, I described the synthesis of CdSe/CdS core/shell QDs with different core size from 2.8 nm to 4.8 nm and similar shell thickness. Moreover, the core/shell QDs were applied to sensitize mesoporous TiO₂ films for solar-driven H₂ generation. By controlling the reaction time from 2 min to 10 min under the growth temperature of 260 °C, the CdSe core QDs grew into different size which first-excitonic absorption peaks varied from 537 nm to 605 nm. After the synthesis of CdSe core QDs, SILAR method was further conducted to grow the CdS shell on the surface of CdSe core which first-excitonic absorption peak varied from 585 nm to 635 nm. When these four types of CdSe/CdS core/shell QDs were applied for PEC H₂ generation, the saturated photocurrent density first increases from 8.8 mA/cm² for CdSe (2.8 nm)/CdS QDs to 15.8 mA/cm² for CdSe (3.1 nm)/CdS QDs and 17.4 mA/cm² for CdSe (3.5 nm)/CdS QDs, then decreasing to 12.9 mA/cm² for CdSe (4.8 nm)/CdS QDs, respectively. Thus, the CdSe (3.5 nm)/CdS core/shell QDs is approved to be the optimized core size in CdSe/CdS core/shell architecture for PEC performance which is mainly because the QDs have the enhanced

absorption range compared to QDs with smaller core while its charge transfer efficiency is higher than QDs with larger core. Finally, based on the core size of CdSe (3.5 nm)/CdS QDs, alloyed CdSe/CdSeS/CdS QDs was designed to improve the PEC performance furthermore by optimizing the shell composition.

In chapter 4, I discussed the synthesis of two types CdSe/CdSe_xS_{1-x}/CdS alloyed QDs. Furthermore, CdSe/CdS core/shell QDs and two types of alloyed QDs were applied for PEC H₂ generation, the saturated photocurrent increased from 6.2 mA/cm² for CdSe/CdS QDs to 15.1 mA/cm² for CdSe/Alloy#1 QDs which is 2.4 times higher. When replaced with gradient composition in the shell, the saturated current density of CdSe/Alloy#2 QDs based photoanode can achieve as high as 17.5 mA/cm² which is 2.8 times higher than the CdSe/CdS QDs. In addition, long-term stable performance was found in the PEC devices based on CdSe/Alloy#2 QDs which can maintain 50 % of the initial photocurrent density value for over 39 hours under continuous illumination.

In chapter 5, I investigated synthesizing CdSe/CdS/ZnS and CdSe/CdSe_xS_{1-x}/Cd_yZn_{1-y}S core/multiple shell QDs and their application for PEC H₂ generation. The saturated photocurrent density can reach as high as 12.6 mA/cm² for CdSe/6CdS core/shell QDs without ZnS shell based photoanode. After the replacement of the two external layers of CdS shell with ZnS shell, the saturated photocurrent density increased up to 14.2 mA/cm² for CdSe/4CdS/2ZnS QDs based photoanode. Furthermore, with the addition of alloyed layers CdSe_xS_{1-x} and Cd_yZn_{1-y}S between the shells, the band alignment was further optimized for faster carrier transfer, leading to saturated photocurrent density of 20.5 mA/cm² for CdSe/(CdSe_xS_{1-x})₃/CdS/Cd_yZn_{1-y}S/ZnS QDs based photoanode. More importantly, a promising stability performance of 93.4 % of the initial photocurrent density was achieved after 2-hour continuous illumination.

6.2 Perspectives

This thesis gives a direction of band engineering approach between the core and shells via core size as well as shell composition optimization. Moreover, these core/shell or core/shell/shell

QDs can not only applied for PEC H₂ evolution, but also for other applications, such as QD-based light emitting diode, QD solar cell, luminescent solar concentrators, etc. In the future, toxicity is an important factor to be considered, in many cases, before QDs can be put into practical use. In particular, the most used QDs for H₂ generation or solar cell is still Pb-based or Cd-based QDs, such as CdSe, CdS, PbS. The toxicity of QDs is affected by many parameters such as chemical composition, size, shape, aggregation status, surface coating, and dose. Although some types of QDs can be presently prepared with tight size and shape control and various surface chemistries, to date systematic and thorough investigations of QD toxicity is still lacking, which largely limits the use of QDs in biomedicine. The promising strategy is to use heavy-metal free QDs as the replacement of Pb/Cd-based QDs. For example, there are some researchers started to use CuInSe, CuInS or even carbon QD as the alternatives which bring less environment problems. The promising future direction could be developing high efficiency heavy-metal free QDs for optoelectronic devices.

The second main issue of QDs based optoelectronic device is the stability performance. Generally, the efficiency of QDs based PEC cell is quite good compared to many metal oxide semiconductors, such as TiO₂, Fe₂O₃, SnO₂ and CuO. However, the stability of QDs based anode is main restriction for wider application of QDs in the optoelectronic devices. For example, after few hours, the efficiency of QDs based anode can drop to half of the initial current density and up to more than 10 hours, it is not work at all. Such deterioration is mainly due to photo-oxidation, photo-degradation and photo-corrosion. There should be more strategies to address the issue of instability. If the QDs based anode can work up to hundreds of hours, it can be a real promising candidate to transfer solar energy into green energy resources. There are many strategies can be used to improve the stability performance of QD-based devices. The morphology design can be a good method to suppress the photo-degradation. For example, the pyramid morphology can accelerate the carrier spatial dissociation, leading to less recombination inside the QDs. The surface of QDs is another critical part for the instability of QDs. Due to the instincts of QDs, the surface is sensitive to the outside environment changes which will dramatically impact the performance of QD-base optoelectronic devices. The surface engineering is a promising direction to improve the performance and stability.

Last but not least, the STH efficiency is still lower than the requirement of application. To further improve the PEC performance, some parameters are significant for the final performance. The absorption range of QDs means how many photons we can capture from solar irradiation. Subsequently, the band alignment decides the carrier transfer efficiency which means how many active electrons we lose in the transportation. Finally, the catalytic process means how many electrons can be transformed into H₂ on the surface of cathode. Every single part needs researchers to investigate for the improvement of final PEC performance.

BIBLIOGRAPHY

- 1 A. P. Alivisatos. Semiconductor clusters, nanocrystals, and quantum dots. *Science*, 271(5251), 933-937, 1996.
- 2 F. P. García de Arquer, D. V. Talapin, V. I. Klimov, Y. Arakawa, M. Bayer and E. H. Sargent. Semiconductor quantum dots: Technological progress and future challenges. *Science*, 373(6555), eaaz8541, 2021.
- 3 M. A. Boles, D. Ling, T. Hyeon and D. V. Talapin. Erratum: the surface science of nanocrystals. *Nature Materials*, 15(3), 364-364, 2016.
- 4 A. T. Fafarman, W. K. Koh, B. T. Diroll, D. K. Kim, D. K. Ko, S. J. Oh, X. Ye, V. Doan-Nguyen, M. R. Crump, D. C. Reifsnyder, C. B. Murray and C. R. Kagan. Thiocyanate-capped nanocrystal colloids: vibrational reporter of surface chemistry and solution-based route to enhanced coupling in nanocrystal solids. *Journal of the American Chemical Society*, 133(39), 15753-15761, 2011.
- 5 M. J. Currie, J. K. Mapel, T. D. Heidel, S. Goffri and M. A. Baldo. High-efficiency organic solar concentrators for photovoltaics. *Science*, 321(5886), 226-228, 2008.
- 6 P. V. Kamat. Quantum dot solar cells. Semiconductor nanocrystals as light harvesters. *The Journal of Physical Chemistry C*, 112(48), 18737-18753, 2008.
- 7 A. J. Nozik, M. C. Beard, J. M. Luther, M. Law, R. J. Ellingson and J. C. Johnson. Semiconductor quantum dots and quantum dot arrays and applications of multiple exciton generation to third-generation photovoltaic solar cells. *Chemical Reviews*, 110(11), 6873-6890, 2010.
- 8 D. V. Talapin, J. S. Lee, M. V. Kovalenko and E. V. Shevchenko. Prospects of colloidal nanocrystals for electronic and optoelectronic applications. *Chemical Reviews*, 110(1), 389-458, 2010.

- 9 L. R. Bradshaw, K. E. Knowles, S. McDowall and D. R. Gamelin. Nanocrystals for luminescent solar concentrators. *Nano Letters*, 15(2), 1315-1323, 2015.
- 10 G. H. Carey, A. L. Abdelhady, Z. Ning, S. M. Thon, O. M. Bakr and E. H. Sargent. Colloidal quantum dot solar cells. *Chemical Reviews*, 115(23), 12732-12763, 2015.
- 11 I. Moreels, K. Lambert, D. Smeets, D. De Muynck, T. Nollet, J. C. Martins, F. Vanhaecke, A. Vantomme, C. Delerue, G. Allan and Z. Hens. Size-dependent optical properties of colloidal PbS quantum dots. *ACS Nano*, 3(10), 3023-3030, 2009.
- 12 F. T. Rabouw and de C. Mello Donega. Photoactive Semiconductor Nanocrystal Quantum Dots: Fundamentals and Applications. *Springer*, 1-30, 2017.
- 13 P. Reiss, M. Protiere and L. Li. Core/shell semiconductor nanocrystals. *Small*, 5(2), 154-168, 2009.
- 14 H. Zhao and F. Rosei. Colloidal quantum dots for solar technologies. *Chem*, 3(2), 229-258, 2017.
- 15 B. O. Dabbousi, J. Rodriguez-Viejo, F. V. Mikulec, J. R. Heine, H. Mattoussi, R. Ober, K. F. Jensen and M. G. Bawendi. (CdSe) ZnS core-shell quantum dots: synthesis and characterization of a size series of highly luminescent nanocrystallites. *The Journal of Physical Chemistry B*, 101(46), 9463-9475, 1997.
- 16 S. Bisschop, P. Geiregat, T. Aubert and Z. Hens. The impact of core/shell sizes on the optical gain characteristics of CdSe/CdS quantum dots. *ACS Nano*, 12(9), 9011-9021, 2018.
- 17 H. Zhao, M. Chaker and D. Ma. Effect of CdS shell thickness on the optical properties of water-soluble, amphiphilic polymer-encapsulated PbS/CdS core/shell quantum dots. *Journal of Materials Chemistry*, 21(43), 17483-17491, 2011.
- 18 J. Li and L. W. Wang. First principle study of core/shell structure quantum dots. *Applied Physics Letters*, 84(18), 3648-3650, 2004.

- 19 Y. Chen, J. Vela, H. Htoon, J. L. Casson, D. J. Werder, D. A. Bussian, V. I. Klimov and J. A. Hollingsworth, "Giant" multishell CdSe nanocrystal quantum dots with suppressed blinking. *Journal of the American Chemical Society*, 130(15), 5026-5027, 2008.
- 20 J. Huang, K. L. Mulfort, P. Du and L. X. Chen. Photodriven charge separation dynamics in CdSe/ZnS core/shell quantum dot/cobaloxime hybrid for efficient hydrogen production. *Journal of the American Chemical Society*, 134(40), 16472-16475, 2012.
- 21 D. C. Neo, C. Cheng, S. D. Stranks, S. M. Fairclough, J. S. Kim, A. I. Kirkland, J. M. Smith, H. J. Snaith, H. E. Assender and A. A. Watt. Influence of shell thickness and surface passivation on PbS/CdS core/shell colloidal quantum dot solar cells. *Chemistry of Materials*, 26(13), 4004-4013, 2014.
- 22 Z. Pan, H. Zhang, K. Cheng, Y. Hou, J. Hua and X. Zhong. Highly efficient inverted type-I CdS/CdSe core/shell structure QD-sensitized solar cells. *ACS Nano*, 6(5), 3982-3991, 2012.
- 23 J. Wang, I. Mora-Seró, Z. Pan, K. Zhao, H. Zhang, Y. Feng, G. Yang, X. Zhong and J. Bisquert. Core/shell colloidal quantum dot exciplex states for the development of highly efficient quantum-dot-sensitized solar cells. *Journal of the American Chemical Society*, 135(42), 15913-15922, 2013.
- 24 S. Yu, X. B. Fan, X. Wang, J. Li, Q. Zhang, A. Xia, S. Wei, L. Wu, Y. Zhou and G. R. Patzke. Efficient photocatalytic hydrogen evolution with ligand engineered all-inorganic InP and InP/ZnS colloidal quantum dots. *Nature Communications*, 9(1), 1-10, 2018.
- 25 L. Etgar, D. Yanover, R. K. Čapek, R. Vaxenburg, Z. Xue, B. Liu, M. K. Nazeeruddin, E. Lifshitz and M. Grätzel. Core/shell PbSe/PbS QDs TiO₂ heterojunction solar cell. *Advanced Functional Materials*, 23(21), 2736-2741, 2013.
- 26 K. Zhao, Z. Pan and X. Zhong. Charge recombination control for high efficiency quantum dot sensitized solar cells. *The Journal of Physical Chemistry Letters*, 7(3), 406-417, 2016.

- 27 S. Kim, B. Fisher, H. J. Eisler and M. Bawendi. Type-II quantum dots: CdTe/CdSe (core/shell) and CdSe/ZnTe (core/shell) heterostructures. *Journal of the American Chemical Society*, 125(38), 11466-11467, 2003.
- 28 R. Xie, X. Zhong and T. Basché. Synthesis, characterization, and spectroscopy of type-II core/shell semiconductor nanocrystals with ZnTe cores. *Advanced Materials*, 17(22), 2741-2745, 2005.
- 29 B. De Geyter, Y. Justo, I. Moreels, K. Lambert, P. F. Smet, D. Van Thourhout, A. J. Houtepen, D. Grodzinska, C. de Mello Donega, A. Meijerink, D. Vanmaekelbergh and Z. Hens. The different nature of band edge absorption and emission in colloidal PbSe/CdSe core/shell quantum dots. *ACS Nano*, 5(1), 58-66, 2011.
- 30 Y. Jia, J. Chen, K. Wu, A. Kaledin, D. G. Musaev, Z. Xie and T. Lian. Enhancing photo-reduction quantum efficiency using quasi-type II core/shell quantum dots. *Chemical Science*, 7(7), 4125-4133, 2016.
- 31 A. I. Channa, X. Li, X. Tong and Z. M. Wang. Core/shell quantum-dot-based solar-driven photoelectrochemical cells. *Core/Shell Quantum Dots. Springer, Cham*. 257-286, (2020).
- 32 R. Adhikari, L. Jin, F. Navarro-Pardo, D. Benetti, B. AlOtaibi, S. Vanka, H. Zhao, Z. Mi, A. Vomiero and F. Rosei. High efficiency, Pt-free photoelectrochemical cells for solar hydrogen generation based on “giant” quantum dots. *Nano Energy*, 27, 265-274, 2016.
- 33 Y. Ghosh, B. D. Mangum, J. L. Casson, D. J. Williams, H. Htoon and J. A. Hollingsworth. New insights into the complexities of shell growth and the strong influence of particle volume in nonblinking “giant” core/shell nanocrystal quantum dots. *Journal of the American Chemical Society*, 134(23), 9634-9643, 2012.
- 34 L. Jin, G. Sirigu, X. Tong, A. Camellini, A. Parisini, G. Nicotra, C. Spinella, H. Zhao, S. Sun, V. Morandi, M. Zavelani-Rossi, F. Rosei and A. Vomiero. Engineering interfacial structure in “Giant” PbS/CdS quantum dots for photoelectrochemical solar energy conversion. *Nano*

Energy, 30, 531-541, 2016.

35 F. Navarro-Pardo, H. Zhao, Z. M. Wang and F. Rosei. Structure/property relations in “giant” semiconductor nanocrystals: opportunities in photonics and electronics. *Accounts of Chemical Research*, 51(3), 609-618, 2017.

36 G. S. Selopal, H. Zhao, X. Tong, D. Benetti, F. Navarro-Pardo, Y. Zhou, D. Barba, F. Vidal, Z. M. Wang and F. Rosei, Highly stable colloidal “giant” quantum dots sensitized solar cells. *Advanced Functional Materials*, 27(30), 1701468, 2017.

37 X. Tong, X. T. Kong, Y. Zhou, F. Navarro-Pardo, G. S. Selopal, S. Sun, A. O. Govorov, H. Zhao, Z. M. Wang and F. Rosei. Near-infrared, heavy metal-free colloidal “Giant” core/shell quantum dots. *Advanced Energy Materials*, 8(2), 1701432, 2018.

38 H. Zhao, D. Benetti, L. Jin, Y. Zhou, F. Rosei and A. Vomiero. Absorption enhancement in “Giant” core/alloyed-shell quantum dots for luminescent solar concentrator. *Small*, 12(38), 5354-5365, 2016.

39 X. Tong, X. T. Kong, C. Wang, Y. Zhou, F. Navarro-Pardo, D. Barba, D. Ma, S. Sun, A. O. Govorov, H. Zhao, Z. M. Wang and F. Rosei. Optoelectronic properties in near-infrared colloidal heterostructured pyramidal “Giant” core/shell quantum dots. *Advanced Science*, 5(8), 1800656, 2018.

40 R. E. Bailey and S. Nie. Alloyed semiconductor quantum dots: tuning the optical properties without changing the particle size. *Journal of the American Chemical Society*, 125(23), 7100-7106, 2003.

41 Z. Pan, K. Zhao, J. Wang, H. Zhang, Y. Feng and X. Zhong. Near infrared absorption of CdSe_xTe_{1-x} alloyed quantum dot sensitized solar cells with more than 6% efficiency and high stability. *ACS Nano*, 7(6), 5215-5222, 2013.

42 W. K. Bae, L. A. Padilha, Y. S. Park, H. McDaniel, I. Robel, J. M. Pietryga and V. I. Klimov.

Controlled alloying of the core-shell interface in CdSe/CdS quantum dots for suppression of Auger recombination. *ACS Nano*, 7(4), 3411-3419, 2013.

43 R. Adhikari, K. Basu, Y. Zhou, F. Vetrone, D. Ma, S. Sun, F. Vidal, H. Zhao and F. Rosei. Heterostructured quantum dot architectures for efficient and stable photoelectrochemical hydrogen production. *Journal of Materials Chemistry A*, 6(16), 6822-6829, 2018.

44 H. Zhu, N. Song and T. Lian. Controlling charge separation and recombination rates in CdSe/ZnS type I core-shell quantum dots by shell thicknesses. *Journal of the American Chemical Society*, 132(42), 15038-15045, 2010.

45 S. Jin and T. Lian. Electron transfer dynamics from single CdSe/ZnS quantum dots to TiO₂ nanoparticles. *Nano Letters*, 9(6), 2448-2454, 2009.

46 D. V. Talapin, I. Mekis, S. Götzinger, A. Kornowski, O. Benson and H. Weller. CdSe/CdS/ZnS and CdSe/ZnSe/ZnS core-shell-shell nanocrystals. *The Journal of Physical Chemistry B*, 108(49), 18826-18831, 2004.

47 S. Rosen, O. Schwartz and D. Oron. Transient fluorescence of the off state in blinking CdSe/CdS/ZnS semiconductor nanocrystals is not governed by Auger recombination. *Physical Review Letters*, 104(15), 157404, 2010.

48 Y. Wang, V. D. Ta, Y. Gao, T. C. He, R. Chen, E. Mutlugun, H. V. Demir and H. D. Sun. Stimulated emission and lasing from CdSe/CdS/ZnS core-multi-shell quantum dots by simultaneous three-photon absorption. *Advanced Materials*, 26(18), 2954-2961, 2014.

49 B. C. Fitzmorris, J. K. Cooper, J. Edberg, S. Gul, J. Guo and J. Z. Zhang. Synthesis and structural, optical, and dynamic properties of core/shell/shell CdSe/ZnSe/ZnS quantum dots. *The Journal of Physical Chemistry C*, 116(47), 25065-25073, 2012.

50 M. Kuno, J. K. Lee, B. O. Dabbousi, F. V. Mikulec and M. G. Bawendi. The band edge luminescence of surface modified CdSe nanocrystallites: Probing the luminescing state. *The*

Journal of Chemical Physics, 106(23), 9869-9882. 1997.

51 P. Reiss, S. Carayon, J. Bleuse and A. Pron. Low polydispersity core/shell nanocrystals of CdSe/ZnSe and CdSe/ZnSe/ZnS type: preparation and optical studies. *Synthetic Metals*, 139(3), 649-652, 2003.

52 H. Zhao, X. Li, M. Cai, C. Liu, Y. You, R. Wang, A. I. Channa, F. Lin, D. Huo, G. Xu, X. Tong and Z. M. Wang. Role of copper doping in heavy metal-free InP/ZnSe core/shell quantum dots for highly efficient and stable photoelectrochemical cell. *Advanced Energy Materials*, 11(31), 2101230, 2021.

53 A. L. Rogach, A. Eychmüller, S. G. Hickey and S. V. Kershaw. Infrared-emitting colloidal nanocrystals: synthesis, assembly, spectroscopy, and applications. *Small*, 3(4), 536-557, 2007.

54 Z. A. Peng and X. Peng. Formation of high-quality CdTe, CdSe, and CdS nanocrystals using CdO as precursor. *Journal of the American Chemical Society*, 123(1), 183-184, 2001.

55 M. A. Hines and G. D. Scholes. Colloidal PbS nanocrystals with size-tunable near-infrared emission: observation of post-synthesis self-narrowing of the particle size distribution. *Advanced Materials*, 15(21), 1844-1849, 2003.

56 H. Zhao, G. Sirigu, A. Parisini, A. Camellini, G. Nicotra, F. Rosei, V. Morandi, M. Zavelani-Rossi and A. Vomiero, Dual emission in asymmetric “giant” PbS/CdS/CdS core/shell/shell quantum dots. *Nanoscale*, 8(7), 4217-4226, 2016.

57 M. Brumer, A. Kigel, L. Amirav, A. Sashchiuk, O. Solomesch, N. Tessler and E. Lifshitz. PbSe/PbS and PbSe/PbSe_xS_{1-x} core/shell nanocrystals. *Advanced Functional Materials*, 15(7), 1111-1116, 2005.

58 S. Xu, J. Ziegler and T. Nann. Rapid synthesis of highly luminescent InP and InP/ZnS nanocrystals. *Journal of Materials Chemistry*, 18(23), 2653-2656, 2008.

59 R. Toufanian, X. Zhong, J. C. Kays, A. M. Saeboe and A. M. Dennis. Correlating ZnSe

quantum dot absorption with particle size and concentration. *Chemistry of Materials*, 33(18), 7527-7536, 2021.

60 C. Xia, W. Wu, T. Yu, X. Xie, C. Van Oversteeg, H. C. Gerritsen and C. de Mello Donega. Size-dependent band-gap and molar absorption coefficients of colloidal CuInS₂ quantum dots. *ACS Nano*, 12(8), 8350-8361, 2018.

61 M. Grätzel. Photoelectrochemical cells. *Nature*, 414, 338-344, 2001.

62 X. Chen, S. Shen, L. Guo and S. S. Mao. Semiconductor-based photocatalytic hydrogen generation. *Chemical Reviews*, 110(11), 6503-6570, 2010.

63 D. Bae, B. Seger, P. C. Vesborg, O. Hansen and I. Chorkendorff. Strategies for stable water splitting via protected photoelectrodes. *Chemical Society Reviews*, 46(7), 1933-1954, 2017.

64 A. Fujishima and K. Honda. Electrochemical photolysis of water at a semiconductor electrode. *Nature*, 238(5358), 37-38, 1972.

65 Q. Huang, F. Li, Y. Gong, J. Luo, S. Yang, Y. Luo, D. Li, X. Bai and Q. Meng. Recombination in SnO₂-based quantum dots sensitized solar cells: the role of surface states. *The Journal of Physical Chemistry C*, 117(21), 10965-10973, 2013.

66 H. McDaniel, N. Fuke, N. S. Makarov, J. M. Pietryga and V. I. Klimov. An integrated approach to realizing high-performance liquid-junction quantum dot sensitized solar cells. *Nature Communications*, 4(1), 1-10, 2013.

67 E. H. Sargent. Colloidal quantum dot solar cells. *Nature Photonics*, 6(3), 133-135, 2012.

68 R. Wang, Y. Shang, P. Kanjanaboos, W. Zhou, Z. Ning and E. H. Sargent. Colloidal quantum dot ligand engineering for high performance solar cells. *Energy & Environmental Science*, 9(4), 1130-1143, 2016.

69 R. Wang, X. Wu, K. Xu, W. Zhou, Y. Shang, H. Tang, H. Chen and Z. Ning. Highly efficient

inverted structural quantum dot solar cells. *Advanced Materials*, 30(7), 1704882, 2018.

70 Y. Zhou, D. Benetti, Z. Fan, H. Zhao, D. Ma, A. O. Govorov, A. Vomiero. and F. Rosei. Near infrared, highly efficient luminescent solar concentrators. *Advanced Energy Materials*, 6(11), 1501913, 2016.

71 Y. Zhou, H. Zhao, D. Ma and F. Rosei. Harnessing the properties of colloidal quantum dots in luminescent solar concentrators. *Chemical Society Reviews*, 47(15), 5866-5890, 2018.

72 H. Zhao, Y.Z hou, D. Benetti, D. Ma and F. Rosei. Perovskite quantum dots integrated in large-area luminescent solar concentrators. *Nano Energy*, 37, 214-223, 2017.

73 Y. Zhou, D. Benetti, X. Tong, L. Jin, Z. M. Wang, D. Ma, H. Zhao and F. Rosei. Colloidal carbon dots based highly stable luminescent solar concentrators. *Nano Energy*, 44, 378-387, 2018.

74 H. Zhao, D. Benetti, L. Jin, Y. Zhou, F. Rosei and A. Vomiero. Absorption enhancement in “Giant” core/alloyed-shell quantum dots for luminescent solar concentrator. *Small*, 12(38), 5354-5365, 2016.

75 H. Zhao, G. Liu, S. You, F. V. Camargo, M. Zavelani-Rossi, X. Wang, C. Sun, B. Liu, Y. Zhang, G. Han, A. Vomiero and X. Gong. Gram-scale synthesis of carbon quantum dots with a large Stokes shift for the fabrication of eco-friendly and high-efficiency luminescent solar concentrators. *Energy & Environmental Science*, 14(1), 396-406, 2021.

76 O. K. Varghese, D. Gong, M. Paulose, K. G. Ong, E. C. Dickey, and C. A. Grimes. Extreme changes in the electrical resistance of titania nanotubes with hydrogen exposure. *Advanced Materials*, 15(7-8), 624-627, 2003.

77 G. Liu, L. C. Yin, J. Wang, P. Niu, C. Zhen, Y. Xie and H. M. Cheng, A red anatase TiO₂ photocatalyst for solar energy conversion. *Energy & Environmental Science*, 5(11), 9603-9610, 2012.

- 78 G. Liu, Y. Zhao, C. Sun, F. Li, G. Q. Lu and H. M. Cheng. Synergistic effects of B/N doping on the visible-light photocatalytic activity of mesoporous TiO₂. *Angewandte Chemie International Edition*, 47(24), 4516-4520, 2008.
- 79 W. Wang, C. Jin and L. Qi. Hierarchical CdS nanorod@ SnO₂ nanobowl arrays for efficient and stable photoelectrochemical hydrogen generation. *Small*, 14(33), 1801352, 2018.
- 80 K. Basu, H. Zhang, H. Zhao, S. Bhattacharya, F. Navarro-Pardo, P. K. Datta, L. Jin, S. Sun F. Vetrone and F. Rosei. Highly stable photoelectrochemical cells for hydrogen production using a SnO₂-TiO₂/quantum dot heterostructured photoanode. *Nanoscale*, 10(32), 15273-15284, 2018.
- 81 Z. Zhang, C. Gao, Z. Wu, W. Han, Y. Wang, W. Fu, X. Li and E. Xie. Toward efficient photoelectrochemical water-splitting by using screw-like SnO₂ nanostructures as photoanode after being decorated with CdS quantum dots. *Nano Energy*, 19, 318-327, 2016.
- 82 G. Wang, Y. Ling, D. A. Wheeler, K. E. George, K. Horsley, C. Heske, J. Z. Zhang and Y. Li. Facile synthesis of highly photoactive α -Fe₂O₃-based films for water oxidation. *Nano Letters*, 11(8), 3503-3509, 2011.
- 83 H. M. Chen, C. K. Chen, Y. C. Chang, C. W. Tsai, R. S. Liu, S. F. Hu, W. S. Chang and K. H. Chen. Quantum dot monolayer sensitized ZnO nanowire-array photoelectrodes: true efficiency for water splitting. *Angewandte Chemie International Edition*, 122(34), 6102-6105, 2010.
- 84 J. Tian, Q. Zhang, L. Zhang, R. Gao, L. Shen, S. Zhang, X. Qu and G. Cao. ZnO/TiO₂ nanocable structured photoelectrodes for CdS/CdSe quantum dot co-sensitized solar cells. *Nanoscale*, 5(3), 936-943, 2013.
- 85 L. Jin, H. Zhao, Z. M. Wang and F. Rosei. Quantum dots-based photoelectrochemical hydrogen evolution from water splitting. *Advanced Energy Materials*, 11(12), 2003233, 2021.
- 86 L. Besra and M. Liu. A review on fundamentals and applications of electrophoretic

deposition (EPD). *Progress in Materials Science*, 52(1), 1-61, 2007.

87 L. Jin, H. Zhao, D. Ma, A. Vomiero and F. Rosei. Dynamics of semiconducting nanocrystal uptake into mesoporous TiO₂ thick films by electrophoretic deposition. *Journal of Materials Chemistry A*, 3(2), 847-856, 2015.

88 H. Zhao, G. Liu, F. Vidal, Y. Wang and A. Vomiero. Colloidal thick-shell pyramidal quantum dots for efficient hydrogen production. *Nano Energy*, 53, 116-124, 2018.

89 H. Zhang, L. V. Besteiro, J. Liu, C. Wang, G. S. Selopal, Z. Chen, D. Barba, Z. M. Wang, H. Zhao, G. P. Lopinski, S. Sun and F. Rosei. Efficient and stable photoelectrochemical hydrogen generation using optimized colloidal heterostructured quantum dots. *Nano Energy*, 79, 105416, 2021.

90 Y. L. Lee and Y. S. Lo. Highly efficient quantum-dot-sensitized solar cell based on co-sensitization of CdS/CdSe. *Advanced Functional Materials*, 19(4), 604-609, 2009.

91 L. Jin, , B. AlOtaibi, D. Benetti, S. Li, H. Zhao, Z. Mi, A. Vomiero and F. Rosei. Near-infrared colloidal quantum dots for efficient and durable photoelectrochemical solar-driven hydrogen production. *Advanced Science*, 3(3), 1500345, 2016.

92 J. Liu, H. Zhang, F. Navarro-Pardo, G. S. Selopal, S. Sun, Z. M. Wang, H. Zhao and F. Rosei. Hybrid surface passivation of PbS/CdS quantum dots for efficient photoelectrochemical hydrogen generation. *Applied Surface Science*, 530, 147252, 2020.

93 X. Tong, Y. Zhou, L. Jin, K. Basu, R. Adhikari, G. S. Selopal, X. Tong, H. Zhao, S. Sun, A. Vomiero, Z. M. Wang and F. Rosei. Heavy metal-free, near-infrared colloidal quantum dots for efficient photoelectrochemical hydrogen generation. *Nano Energy*, 31, 441-449, 2017.

94 B. Luo, J. Liu, H. Guo, X. Liu, R. Song, K. Shen, Z. M. Wang, D. Jing, G. S. Selopal and F. Rosei. High efficiency photoelectrochemical hydrogen generation using eco-friendly Cu doped Zn-In-Se colloidal quantum dots. *Nano Energy*, 88, 106220, 2021.

- 95 Z. Lin, A. Franceschetti and M. T. Lusk. Size dependence of the multiple exciton generation rate in CdSe quantum dots. *ACS Nano*, 5(4), 2503-2511, 2011.
- 96 D. J. Norris, A. L. Efros, M. Rosen and M. G. Bawendi.. Size dependence of exciton fine structure in CdSe quantum dots. *Physical Review B*, 53(24), 16347, 1996.
- 97 H. Zhao, Z. Fan, H. Liang, G. S. Selopal, B. A. Gonfa, L. Jin, A. Souidi, D. Cui, F. Enrichi, M. M. Natile, I. Concina, D. Ma, A. O. Govorov, F. Rosei and A. Vomiero.. Controlling photoinduced electron transfer from PbS@ CdS core@ shell quantum dots to metal oxide nanostructured thin films. *Nanoscale*, 6(12), 7004-7011, 2014.
- 98 D. R. Pernik, K. Tvrdy, E. J. Radich and P. V. Kamat. Tracking the adsorption and electron injection rates of CdSe quantum dots on TiO₂: linked versus direct attachment. *The Journal of Physical Chemistry C*, 115(27), 13511-13519, 2011.
- 99 F. Li, M. Zhang, D. Benetti, L. Shi, L. V. Besteiro, H. Zhang, J. Liu, G. S. Selopal, S. Sun, Z. Wang, Q. Wei and F. Rosei. “Green”, gradient multi-shell CuInSe₂/(CuInSe_xS_{1-x})₅/CuInS₂ quantum dots for photo-electrochemical hydrogen generation. *Applied Catalysis B: Environmental*, 280, 119402, 2021.
- 100 E. Lifshitz, M. Brumer, A. Kigel, A. Sashchiuk, M. Bashouti, M. Sirota, E. Galun, Z. Burshtein, A. Q. Le Quang, I. Ledoux-Rak, and J. Zyss. Air-stable PbSe/PbS and PbSe/PbSe_xS_{1-x} core-shell nanocrystal quantum dots and their applications. *The Journal of Physical Chemistry B*, 110(50), 25356-25365, 2006.
- 101 G. Liu, Z. Ling, Y. Wang and H. Zhao. Near-infrared CdSe_xTe_{1-x}@ CdS “giant” quantum dots for efficient photoelectrochemical hydrogen generation. *International Journal of Hydrogen Energy*, 43(49), 22064-22074, 2018.
- 102 H. McDaniel, N. Fuke, N. S. Makarov, J. M. Pietryga and V. I. Klimov. An integrated approach to realizing high-performance liquid-junction quantum dot sensitized solar cells. *Nature Communications*, 4(1), 1-10, 2013.

103 T. X. Ding, J. H. Olshansky, S. R. Leone and A. P. Alivisatos. Efficiency of hole transfer from photoexcited quantum dots to covalently linked molecular species. *Journal of the American Chemical Society*, 137(5), 2021-2029, 2015.

104 M. Cirillo, T. Aubert, R. Gomes, R., R. Van Deun, P. Emplit, A. Biermann, H. Lange, C. Thomsen, E. Brainis and Z. Hens. “flash” synthesis of cdse/cds core-shell quantum dots. *Chemistry of Materials*, 26(2), 1154-1160, 2014.

105 L. Dworak, V. V. Matylitsky, V. V. Breus, M. Braun, T. Basché and J. Wachtveitl. Ultrafast charge separation at the CdSe/CdS core/shell quantum dot/methylviologen interface: implications for nanocrystal solar cells. *The Journal of Physical Chemistry C*, 115(10), 3949-3955, 2011.

106 S. Brovelli, R. D. Schaller, S. A. Crooker, F. García-Santamaría, Y. Chen, R. Viswanatha, J. A. Hollingsworth, H. Htoon and V. I. Klimov. Nano-engineered electron-hole exchange interaction controls exciton dynamics in core-shell semiconductor nanocrystals. *Nature Communications*, 2(1), 1-8, 2011.

107 C. F. Chi, S. Y. Liao and Y. L. Lee. The heat annealing effect on the performance of CdS/CdSe-sensitized TiO₂ photoelectrodes in photochemical hydrogen generation. *Nanotechnology*, 21(2), 025202, 2009.

108 N. Wang, S. Koh, B. G. Jeong, D. Lee, W. D. Kim, K. Park, M. K. Nam, K. Lee, Y. Kim, B. H. Lee, K. Lee, W. K. Bae, D. C. Lee. Highly luminescent silica-coated CdS/CdSe/CdS nanoparticles with strong chemical robustness and excellent thermal stability. *Nanotechnology*, 28(18), 185603, 2017.

109 J. K. Yang, W. S. Kim and H. H. Park. Chemical bonding states and energy band gap of SiO₂-incorporated La₂O₃ films on n-GaAs (001). *Thin Solid Films*, 494(1-2), 311-314, 2006.

110 D. V. Talapin, I. Mekis, S. Götzinger, A. Kornowski, O. Benson and H. Weller CdSe/CdS/ZnS and CdSe/ZnSe/ZnS core-shell-shell nanocrystals. *The Journal of Physical*

Chemistry B, 108(49), 18826-18831, 2004.

111 Y. Wang, V. D. Ta, Y. Gao, T. C. He, R. Chen, E. Mutlugun, H. V. Demir and H. D. Sun. Stimulated emission and lasing from CdSe/CdS/ZnS core-multi-shell quantum dots by simultaneous three-photon absorption. *Advanced Materials*, 26(18), 2954-2961, 2014.

112 S. Nizamoglu and H. V. Demir. Onion-like (CdSe) ZnS/CdSe/ZnS quantum-dot-quantum-well heteronanocrystals for investigation of multi-color emission. *Optics Express*, 16(6), 3515-3526, 2008.

113 H. Zhu, N. Song and T. Lian. Controlling charge separation and recombination rates in CdSe/ZnS type I core-shell quantum dots by shell thicknesses. *Journal of the American Chemical Society*, 132(42), 15038-15045, 2010.

114 K. Wang, X. Tong, Y. Zhou, H. Zhang, F. Navarro-Pardo, G. S. Selopal, G. Liu, J. Tang, Y. Wang, S. Sun, D. Ma, Z. M. Wang, F. Vidal, H. Zhao, X. Sun, F. Rosei, Efficient solar-driven hydrogen generation using colloidal heterostructured quantum dots. *Journal of Material Chemistry A*, 7(23), 14079-14088, 2019.

115 J. Y. Kim, Y. J. Jang, J. Park, J. Kim, J. S. Kang, D. Y. Chung, Y. E. Sung, C. Lee, J. S. Lee, M. J. Ko, Highly loaded PbS/Mn-doped CdS quantum dots for dual application in solar-to-electrical and solar-to-chemical energy conversion, *Applied Catalysis B: Environmental*, 227, 409-417, 2018.

APPENDIX A ABBREVIATIONS

QDs	Quantum dots
PEC	Photoelectrochemical
STH	Solar to hydrogen
SILAR	Successive ionic adsorption and reaction
UV-vis	Ultraviolet-visible
TEM	Transmission electron spectroscopy
XRD	X-ray diffraction
WZ	Wurtzite
ZB	Zinc blende
Abs	Absorption
QY	Quantum yield
PCE	Photoconversion efficiency
H ₂	Hydrogen
TiO ₂	Titanium dioxide
Pt	Platinum
CdO	Cadmium oxide
ZnO	Zinc oxide
S	Sulfur
OA	Oleic acid
OLA	Oleylamine
ODE	1-Octadecene
TOPO	Trioctyl phosphine oxide
TOP	Trioctyl phosphine
Na ₂ S	Sodium sulfide
Na ₂ SO ₃	Sodium sulfite
ZrO ₂	Zirconium oxide
IPA	Isopropanol
FTO	Fluorine doped tin oxide

CTAB	Cetyl-trimethyl ammonium bromide
HRTEM	High-resolution transmission electron microscopy
SAED	Selected area electron diffraction
FE-SEM	Field emission scanning electron microscope
EDS	Energy-dispersive X-ray spectrometer
XPS	X-ray photoelectron spectroscopy
EPD	Electrophoretic deposition
J_{ph}	Saturated photocurrent density
AM	Air mass
IPCE	Incident photon-to-current efficiency
CB	Conduction band
VB	Valence band
RHE	Reversible hydrogen electrode
FE	Faradaic efficiency

APPENDIX B RÉSUMÉ

Production d'hydrogène photoélectrochimique à partir de points quantiques à noyau/coquille colloïdal

Introduction

Les points quantiques colloïdaux (QDs) sont des nanocristaux (NCs) semi-conducteurs dont la taille est généralement inférieure à 20 nm de diamètre. Typiquement, ils sont composés de QDs, un noyau inorganique, et de quelques centaines à quelques milliers d'atomes, entouré d'une couche organique externe de molécules de surfactant (ligands). Les semi-conducteurs qd présentent des effets de quantification spectaculaires, définis par une bande gap croissante accompagnée d'une quantification des niveaux d'énergie en valeurs discrètes, similaire aux niveaux d'énergie atomique. Dans la plupart des semi-conducteurs, une fois la taille réduite à quelques nanomètres, le confinement quantique se produit, conduisant à des propriétés optoélectroniques de QDs dépendant de la taille. Ces effets de taille nous permettent de concevoir et de synthétiser des QDs avec une taille, une forme et une composition chimique contrôlables pour ajuster précisément les transitions optiques et l'énergie des États d'énergie électronique discrets. Cet effet est communément appelé confinement quantique, et permet d'ajuster les spectres optiques des semi-conducteurs NCs à travers une large fenêtre spectrale en changeant simplement leur taille, tout en gardant leur composition constante.

Une étude récente révèle que la croissance d'une coquille à la surface du QDs du cœur peut améliorer La stabilité des propriétés photophysiques des QDs et le rendement quantique (QY). Ainsi, la structure cœur/coquille devient un matériau semi-conducteur plus attrayant pour les dispositifs optoélectroniques, tels que les cellules solaires et photoélectrochimiques (PEC). En particulier, le QDs cœur/coquille consiste en un QDs cœur d'un matériau semi-conducteur et une coquille d'un autre matériau semi-conducteur à la surface du cœur. Pour utiliser efficacement l'irradiation solaire, le CdSe/CdS est un candidat prometteur en tant que collecteur de lumière pour absorber les photons. De plus, en raison du décalage de bande du système

CdSe/CdS cœur-coquille, l'alignement de bande du CdSe/CdS cœur-coquille peut être ajusté pour un meilleur transfert de porteur. Enfin et surtout, peu d'inadéquation du réseau (~3.9 %) entre les deux semi-conducteurs, par ailleurs le CdSe et le CdS jouent également un rôle important dans l'efficacité de conversion élevée du solaire à l'électricité ou du solaire aux combustibles. En raison de ces propriétés favorables, l'architecture CdSe/CdS cœur-coquille reste l'une des architectures les plus efficaces pour les appareils optoélectroniques. La génération d'hydrogène (H₂) PEC est une approche efficace pour obtenir la ressource en énergie de H₂ d'une manière relativement peu perdante, efficace et verte. Par rapport au fractionnement de l'eau par électrolyse, une partie de l'énergie électrique peut être économisée en utilisant l'énergie solaire. Avec la comparaison du fractionnement photochimique de l'eau, le rendement est beaucoup plus élevé. Ainsi, la génération de PEC H₂ est une façon intermédiaire d'obtenir H₂. Depuis que Fujishima et Honda ont découvert pour la première fois une cellule PEC basée sur le TiO₂, les travaux de nombreux ont été étudiés dans différents matériaux semi-conducteurs comme les anodes PEC.

Les qd colloïdaux sont assez intéressants à jouer comme moissonneur pour la génération PEC H₂ entraînée par l'énergie solaire. Au cours des dernières décennies, les QDs sont utilisés comme sensibilisants de l'oxyde métallique pour la génération de PEC H₂, formant une hétérostructure QDs/oxyde métallique. De plus, l'hétérostructure QDs/oxyde métallique peut également fournir la possibilité de construire un alignement de bande favorable au transfert de porteur.

Objectifs de la thèse

- (1) Ces dernières années, beaucoup d'efforts ont donc été consacrés à l'ingénierie de l'épaisseur de la couche pour l'optimisation de l'alignement de la bande cœur-coquille et, par conséquent, l'efficacité finale de conversion basée sur le QDs CdSe/CdS cœur-coquille. Il y a peu de travaux se concentrant sur la taille de noyau du QDs et, par conséquent, l'alignement de la bande cœur-coquille du QDs. Ainsi, motivé par cela, La première partie du travail de cette thèse a synthétisé quatre types de QDs CdSe/CdS cœur-coquille avec des tailles de cœur différentes et la même épaisseur de coquille, puis a étudié les performances

du PEC ainsi que la structure de bande du QDs.

- (2) Le second objectif était de étudier la composition de la coquille du CdS et, par conséquent, les performances du PEC. Certains travaux rapportent l'optimisation de la composition des couches par une approche d'ingénierie de bande pour améliorer les propriétés optoélectroniques. Cependant, il n'y a personne pour signaler une telle architecture pour la génération PEC H₂. En outre, j'ai étudié la couche de gradient pour la génération de PEC H₂ qui est la première fois rapportée.
- (3) Enfin, on introduira dans une troisième partie le QDs cœur/couches multiples pour la génération de PEC H₂. En raison de la faible stabilité de la photoanode basée sur CdSe/CdS QDs. Par conséquent, la couche de passivation de la surface est recouverte de ZnS à large bande interdite. Dans ce travail, j'ai étudié l'épaisseur solidifiée des ZnS pour les performances des PEC. J'ai également ajouté CdSe_xS_{1-x} et Cd_yZn_{1-y}S coquillage allié pour faire un alignement de bande plus favorable pour un transfert de porteur plus efficace.

Résultats et discussions

CdSe/CdS QDs pour la génération PEC H₂

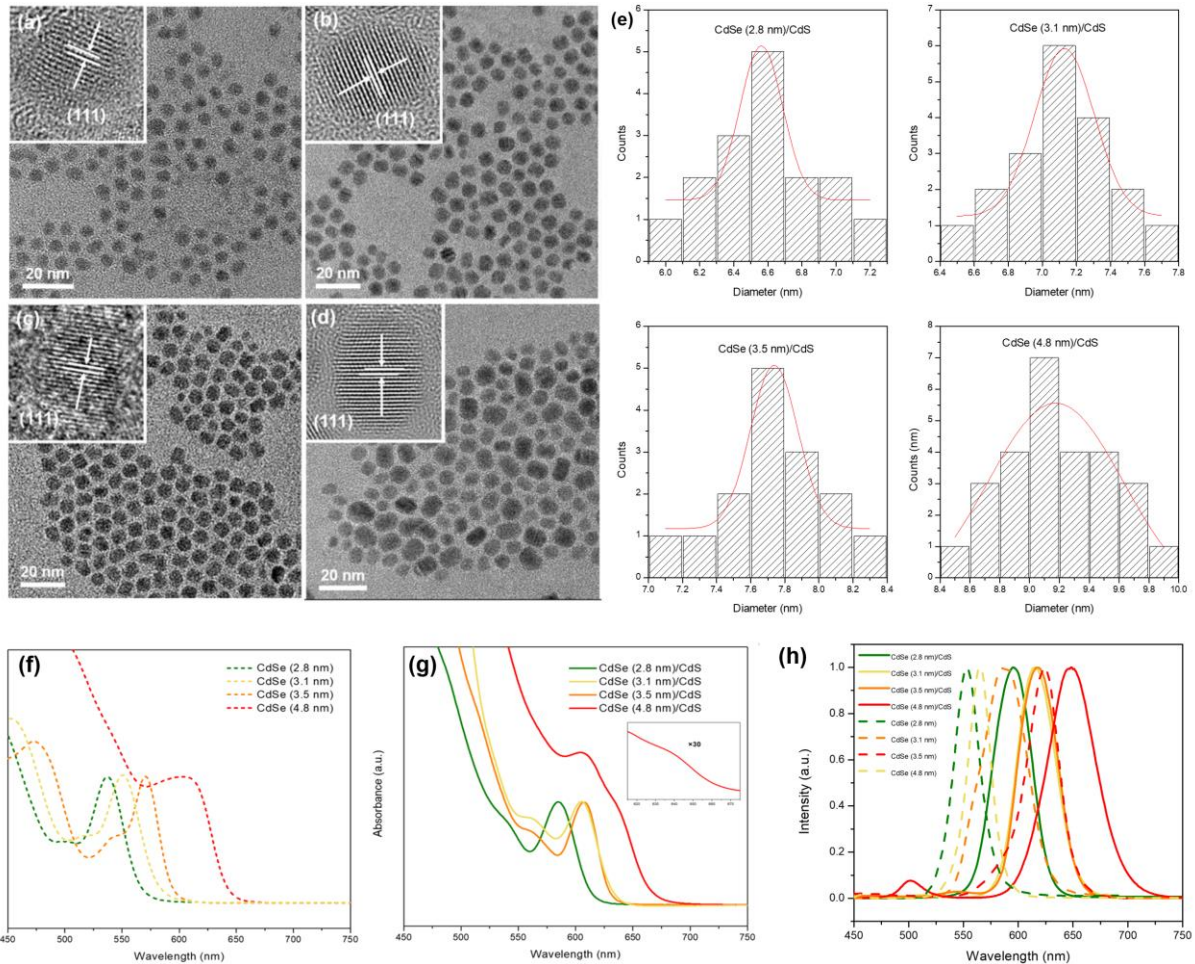


Figure R1 Images MET de (a) CdSe (2.8 nm)/CdS QDs, (b) CdSe (3.1 nm)/CdS QDs, (c) CdSe (3.5 nm)/CdS QDs, (d) CdSe (4.8 nm)/CdS QDs (Les encadrés montrent les images HR-MET des QDs correspondants); (e) Répartition par taille de quatre CdSe/CdS cœur-coquille QDs; Spectres d'absorption UV-vis de (f) quatre cœurs CdSe QDs (g) four CdSe/CdS cœur-coquille QDs; (h) PL spectre de quatre CdSe quatre QDs et quatre CdSe/CdS cœur-coquille.

La caractérisation morphologique a d'abord été montrée dans les images de microscopie électronique en transmission (MET). Dans les figures R1(a)-(d), les images montrent que les QDs ont été distribués uniformément pour quatre types de QDs CdSe/CdS cœur-coquille, tandis que la taille globale augmente avec la taille du QDs du cœur (La répartition par taille est

présentée à la Figure R1(e). Les figures R1(a)-(d) montrent que les QDs ont tous la forte cristallisation dans les images MET haute résolution (HR-MET) et les plans (111) sont représentés en quatre interstices qui correspondent à la structure cristalline blende zinc (BZ) des CdS. Les propriétés optiques des QDs tel qu'il a été préparé ont été étudiées par spectres d'absorption UV-vis et spectre de photoluminescence (PL). Tout d'abord, la taille du cœur CdSe QDs est déterminée par les fonctions mathématiques empiriques du premier pic excitonique des spectres d'absorption UV-vis. La Figure R1(f) montre que le pic d'absorption du premier exciton est situé à 537 nm, 550 nm, 571 nm et 605 nm, respectivement pour quatre cœur CdSe QDs. Après 6 cycles de couches CdS par la méthode d'adsorption et de réaction par couche d'ions (SRSCD), le pic d'absorption du premier exciton montré à la Figure R1(g) a été décalé vers le rouge à 585 nm, 605 nm, 608 nm et 635 nm, respectivement, ce qui indique la croissance épitaxiale réussie des Cd à la surface du CdSe. Selon la Figure R1(h), le spectre PL montre les mêmes phénomènes. Le pic PL de quatre qd CdSe est situé respectivement à 552 nm, 566 nm, 580 nm et 621 nm, , tandis que le pic PL de quatre qd cœur/coquille est passé à 595 nm, 615 nm, 618 nm et 648 nm, respectivement.

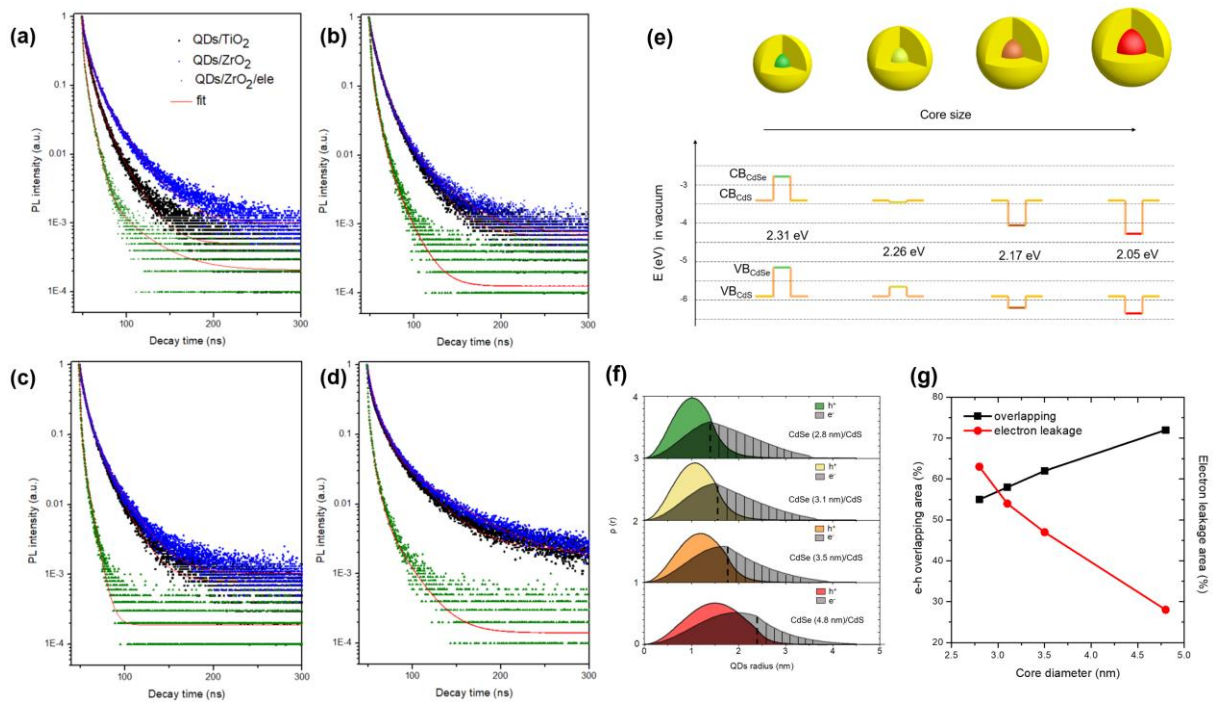


Figure R2 Spectres de (a) CdSe (2.8 nm)/CdS cœur-coquille QDs (b) CdSe (3.1 nm)/CdS cœur-coquille QDs (c) CdSe (3.5 nm)/CdS cœur-coquille QDs et (d) CdSe (4.8 nm)/CdS cœur-coquille QDs après dépôt dans des films de TiO₂, des films de ZrO₂ et des films de ZrO₂ en présence d'un électrolyte; (e) Schéma de quatre qd CdSe/CdS cœur-coquille et leur position dans la bande (bande de conduction/ valence) calculée; (f) Valeur de la distribution spatiale de probabilité $\rho(r)$ des électrons et des trous en fonction du rayon QD (nm) pour quatre QDs CdSe/CdS cœur/coquille (les lignes pointillées montrent la position du rayon et les zones d'ombre indiquent les électrons dans les régions de la couche); (g) La zone de chevauchement et la zone de fuite d'électrons en fonction du rayon du cœur.

Pour étudier le comportement en dynamique porteuse de quatre types de QDs cœur /shell, la durée de vie de PL a été mesurée sur la base de QDs avec différents substrats. Comme le montre la Figure R2(a)-(d), le spectre PL indique la durée de vie moyenne de QDs avec TiO₂ (courbe noire), ZrO₂ (courbe bleue) et ZrO₂ dans l'électrolyte (courbe verte). Le ZrO₂ a été utilisé comme point de référence où l'injection électronique de QDs vers ZrO₂ ne se produit pas en raison de l'alignement de bande défavorable. Ainsi, la dégradation PL peut toutes être attribuée à la recombinaison porteuse. Dans un tel système, le transfert d'énergie entre les QDs a été ignoré. Le CdSe (2.8 nm)/CdS QDs avec la plus petite taille de cœur a montré le taux de

transfert électronique le plus rapide de $3.8 \times 10^{-7} \text{ s}^{-1}$ où il est cohérent avec les premiers résultats que l'alignement de bande du cœur et de la couche pour ce QDs est le plus favorable pour le transfert de porteur. CdSe (3.1 nm)/CdS QDs et CdSe (3.5 nm)/CdS QDs ont montré des taux de transfert d'électrons similaires de $0.5 \times 10^{-7} \text{ s}^{-1}$ et $0.8 \times 10^{-7} \text{ s}^{-1}$, respectivement. Pour CdSe (4.8 nm)/CdS QDs avec la plus grande taille de cœur, le taux de transfert électronique ne peut pas être calculé selon l'équation parce que l'écart de bande du cœur CdSe devient plus étroit, ce qui conduit à un confinement plus fort de la couche CdS, ce qui indique que les électrons ont moins de probabilité de se transférer vers les régions de la couche. En résumé, avec l'augmentation de la taille du cœur CdSe, l'écart de bande du cœur CdSe se rétrécit, conduisant à une efficacité de transfert d'électrons plus faible du cœur vers la coquille. La Figure R2(e) montre également la structure CdSe/CdS cœur-coquille et la position correspondante de bande de quatre cœur-coquille QDs. Les niveaux de CdSe sont déterminés par les résultats de la spectroscopie ultraviolet photoélectron (SUP), tandis que les niveaux de CdS utilisent les niveaux de matériaux en vrac de CdS, suivant les littératures précédentes. Selon la Figure R2(e), il est évident que l'écart de bande du CdSe QDs se rétrécit avec la taille. Ainsi, l'alignement de bande cœur-coquille est passé du Type II au Quasi-Type II, ce qui est cohérent avec les anciens résultats de durée de vie PL.

Pour vérifier davantage le comportement de dissociation de porteur de quatre types de QDs CdSe/CdS cœur-coquille, les fonctions d'onde théoriques des trous d'électrons ont été calculées. Typiquement, les fonctions d'onde de l'électron [$\psi_e(r)$] et du trou [$\psi_h(r)$] pour les quatre types de QDs cœur/coquille ont été calculées en résolvant l'équation de Schrödinger stationnaire en géométrie sphérique. La Figure R2(f) montre la $\psi_h(r)$ et la $\psi_e(r)$ en fonction du rayon du cœur et les lignes pointillées indiquent la position du rayon du cœur pour chaque QDs cœur-coquille, et les zones d'ombre indiquent la probabilité de fuite de l'électron du cœur vers les régions de la couche. Ce résultat théorique a indiqué que quatre types de CdSe/CdS cœur-coquille appartiennent tous à une architecture Quasi-Type II cœur-coquille. La Figure R2(g) montre la zone de chevauchement d'électrons/de trous de quatre types de QDs et la zone de fuite d'électrons en fonction de la taille du cœur. La valeur de la zone de chevauchement augmente avec la plus grande taille du cœur, ce qui est cohérent avec les résultats précédents selon lesquels

les électrons ont plus de probabilité de confiner dans le cœur avec la taille croissante du cœur.

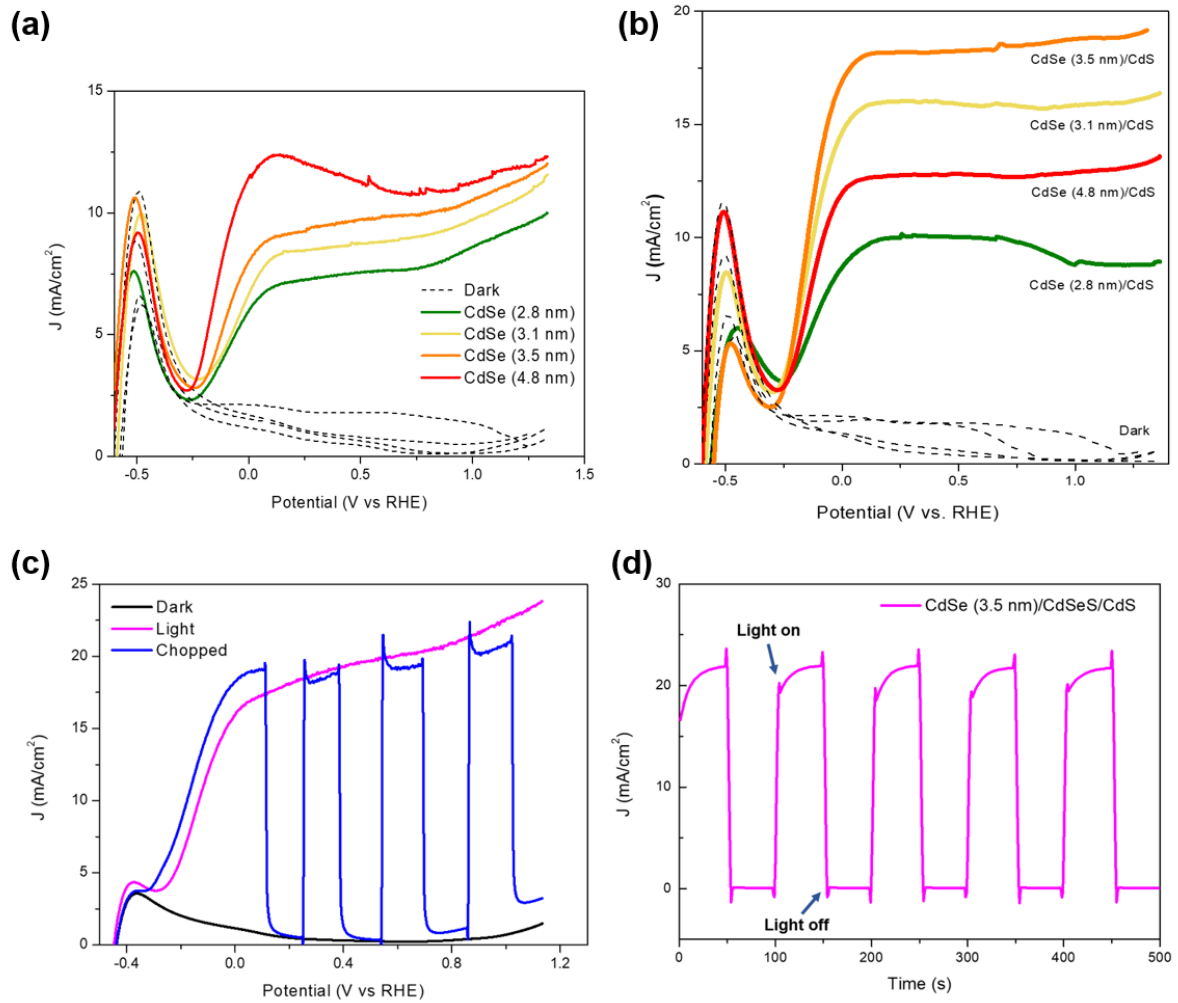


Figure R3 Dépendance entre la densité et le potentiel de photocourant de TiO₂ sensibilisé avec (a) quatre types de QD à noyau CdSe dans l'obscurité et sous un éclairage continu (b) quatre types de QD CdSe/CdS cœur-coquille dans l'obscurité et sous éclairage continu (c) avec alliages QD CdSe/CdSeS/CdS; (d) Photodensité de photocourant en fonction du temps des QD alliés.

Les performances de PEC basées sur le QDs du coeur CdSe sont indiquées à la Figure R3(a). Tout d'abord, on a effectué les courbes $J-V$ de quatre coeur CdSe QDs. La densité de photocourant saturée pour quatre core QDs est de 8.8 mA/cm² pour le CdSe (2.8 nm) QDs, 9.9 mA/cm² pour le CdSe (3.1 nm) QDs, 10.7 mA/cm² pour le CdSe (3.5 nm) QDs et 11.3 mA/cm² pour le CdSe (4.8 nm) QDs, respectivement. Les résultats des performances PEC de quatre CdSe QDs indiquent que la densité de photocourant augmente avec l'augmentation de la taille

du cœur de CdSe, ce qui est principalement dû à l'augmentation de la plage d'absorption apportée par le QDs plus grand. En d'autres termes, pour le CdSe nu QDs, le paramètre dominant pour la performance PEC est la plage d'absorption.

Pour quatre types de CdSe/CdS cœur-coquille QDs qui sont représentés sur la Figure R3(b), la densité de photocourant saturée de l'anode CdSe (2.8 nm)/CdS QDs peut atteindre 8.8 mA/cm² sous un sous l'illumination du soleil. Alors que la densité de photocourant saturée de la photoanode CdSe (3.1 nm)/CdS QDs a augmenté jusqu'à 15.8 mA/cm² ce qui est presque deux fois plus grand que la photoanode CdSe (2.8 nm)/CdS QDs. De plus, pour la photoanode CdSe (3.5 nm)/CdS QDs, la densité de photocourant peut atteindre 17.4 mA/cm², ce qui est presque la plus haute densité de photocourant, même comparée à la photoanode à base de photoanode QDs. Cependant, CdSe (4.8 nm)/CdS QDs qui a la plus grande taille de photoanode à base de photoanode n'a que 12.9 mA/cm² de densité de photocourant saturée, plus faible que CdSe (3.1 nm)/CdS et CdSe (3.5 nm)/CdS QDs. Les résultats de la PEC sont si intéressants que pour un cœur de CdSe relativement petit, l'absorption est le paramètre dominant pour la performance de PEC. Même le taux de transfert d'électrons est beaucoup plus élevé pour CdSe (2.8 nm)/CdS QDs que pour CdSe (3.1 nm)/CdS et CdSe (3.5 nm)/CdS QDs, la performance de PEC est encore beaucoup plus faible en raison de l'absorption plus faible. Mais, lorsque le cœur CdSe est assez grand, l'absorption n'est plus le facteur dominant pour la performance PEC où la densité de photocourant du CdSe (4.8 nm)/CdS QDs est beaucoup plus faible que celle du CdSe (3.1 nm)/CdS et du CdSe (3.5 nm)/CdS QDs. C'est principalement parce que l'efficacité du transfert du porteur commence à déterminer la performance ultime de la PEC plutôt que l'absorption. Même si l'absorption du CdSe (4.8 nm)/CdS QDs est plus élevée que celle du CdSe (3.1 nm)/CdS et du CdSe (3.5 nm)/CdS QDs, le taux de transfert d'électrons est beaucoup plus faible, ce qui conduit à davantage de recombinaison à l'intérieur du QDs. Ainsi, le CdSe (3.5 nm)/CdS QDs s'est avéré être la taille de cœur optimisée ainsi que l'alignement de bande de l'architecture CdSe/CdS.

Donc, pour améliorer encore les performances de PEC basées sur la taille du cœur optimisé de CdSe (3.5 nm)/CdS QDs, des couches d'alliage ont été appliquées pour remplacer les couches

cd pures, formant la structure de CdSe (3.5 nm)/(CdSe_xS_{1-x})₅/CdS QDs (x = 0.5) QDs. Ensuite, les QDs alliés ont également été appliqués avec des films de TiO₂ mésoporeux pour la mesure de *J-V*. Selon la Figure R3(c), il s'avère que la densité de photocourant de la photoanode à base de QDs allié peut atteindre 22 mA/cm² sans précédent sous un éclairage solaire. De plus, la Figure R3(d) montre la densité de photocourant de la photoanode à base de QDs alliés en fonction du temps avec la lumière allumée/éteinte. Il est évident qu'on observe la photo-réponse lorsque l'anode reçoit un éclairage solaire incident et que la densité de photocourant la plus élevée correspond aux résultats de la Figure R3(c). La performance très efficace du PEC d'un photoanode basé sur le QDs allié est due au fait que les alliés QDs cœur/coquille ont un alignement de bande optimisé qui équilibre les paramètres d'absorption ainsi que l'efficacité de transfert des porteurs. De plus, les couches d'alliages intermédiaires servent de courtes voies de transport, conduisant à une séparation et un transfert de transport plus efficaces. En conséquence, la recombinaison peut être largement supprimée. Comparée à la photoanode ayant la plus haute densité de photocourant à jour, la taille du cœur est optimisée par l'ingénierie des bandes.

CdSe/CdSe_xS_{1-x}/CdS alliés QDs pour la génération PEC H₂

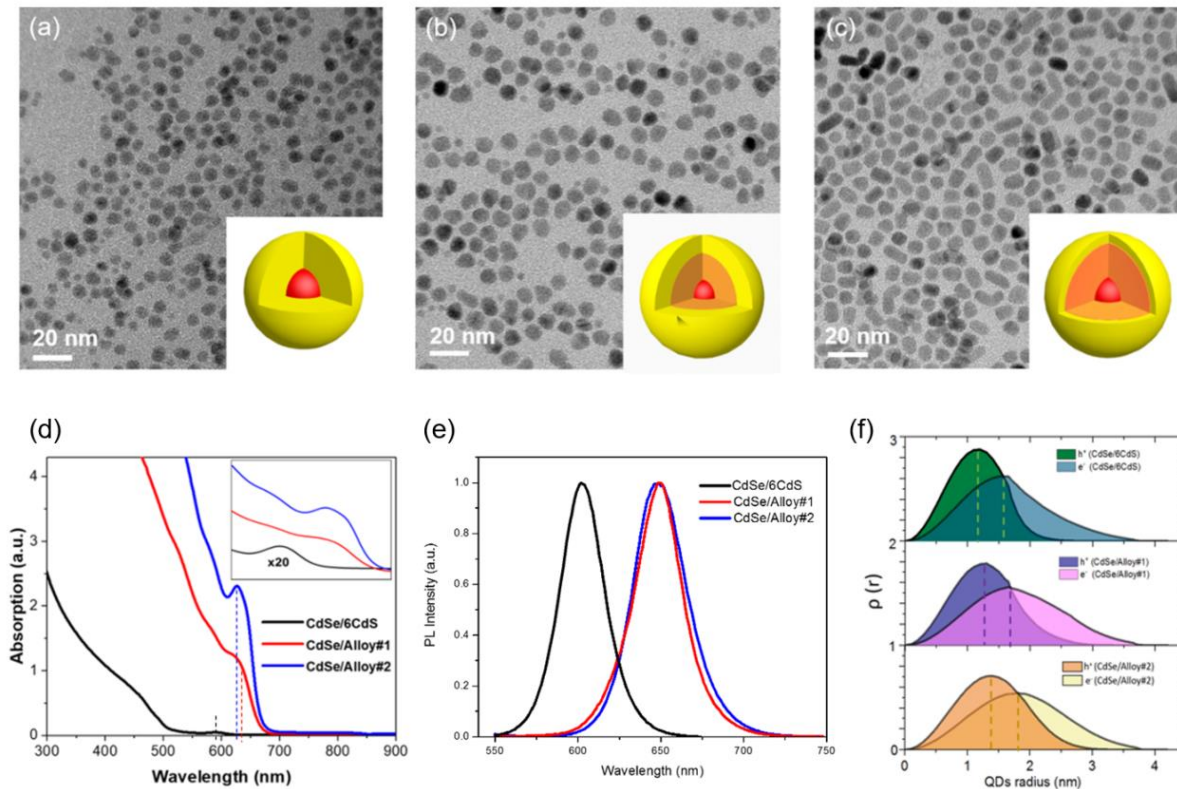


Figure R4 Images MET et structure QDs du (a) CdSe/6CdS; (b) CdSe/Alloy#1; (c) CdSe/Alloy#2; (d) Spectres d'absorption et de PL de trois types de QDs; (f) Valeur de distribution spatiale des $\rho(r)$ de l'électron et du trou en fonction du rayon QD (nm) pour CdSe/6CdS, CdSe/Alloy#1 et CdSe/Alloy#2 QDs (les lignes pointillées montrent les positions des pics).

Dans les images MET, il est évident que les tailles des trois types de QDs augmentent comme le montre la figure R4(a)-(c). Dans le CdSe/CdS QDs, six monocouches de cd ont été revêtues sur le cœur du CdSe (3.3 nm de diamètre) avec une épaisseur de couche de 1.96 nm, ce qui est cohérent avec les images MET. En réglant le rapport d'alimentation des précurseurs Se et S, on a obtenu des QDs CdSe/ CdSe/Alloy#1 et CdSe/Alloy#2 avec respectivement 2.07 nm et 2.50 nm d'épaisseur. La coquille plus épaisse pour CdSe/Alloy#1 et CdSe/Alloy#2 QDs géante par rapport à CdSe/6CdS est due à l'ajout de Se élémentaire dans la coquille. En bref, les diamètres globaux des QD alliés tels que synthétisés sont de 7.7 ± 0.8 nm pour les QD CdSe/Alloy#1 et

de 7.9 ± 0.9 nm pour les QD CdSe/Alloy#2, respectivement. Et pour les QD CdSe/6CdS, les diamètres finaux sont de 7.2 ± 0.5 nm.

La figure R4(d) affiche les pics d'absorption du premier excitonique pour trois types de QD dans le toluène observés à ~ 591 nm (CdSe/6CdS), 632 nm (CdSe/Alloy#1) et 626 nm (CdSe/Alloy#2), respectivement. Ces résultats sont cohérents avec les spectres PL présentés à la Figure R4(e). Avec la présence de couches d'alliage interfaciales, l'absorption des QD est décalée vers des longueurs d'onde plus longues en raison de la bande interdite étroite de CdSe par rapport à CdS et de l'effet de taille quantique lié à l'augmentation de la taille. Dans le même temps, on observe simultanément le pic PL se décaler vers le rouge en raison de la fuite d'électrons du noyau vers la région de la coque. La même position de pic PL dans les deux QD implique le même degré de fuite d'électrons.

Pour vérifier davantage le processus de dissociation des porteurs, nous avons calculé les fonctions d'onde théoriques électron-trou. La fonction d'onde de l'électron [$\psi_e(r)$] et du trou [$\psi_h(r)$] pour deux types de QD à noyau/coque/coque alliés et 6 cycles de QD à coque CdS a été calculée en résolvant l'équation de Schrödinger stationnaire en géométrie sphérique. La distribution de probabilité spatiale calculée [$\rho(r)$] de $\psi_e(r)$ et $\psi_h(r)$ en fonction du rayon QDs (nm) est illustrée à la figure R4(f). Avec l'ajout de couches alliées, à la fois $\psi_e(r)$ et $\psi_h(r)$ montrent une fuite croissante dans la région de la coque en conséquence d'un alignement favorable des bandes. Selon la figure R4(f) (selon les positions des lignes pointillées), les valeurs de chevauchement pour les électrons et les trous augmentent en raison de l'alignement amélioré des bandes. En conséquence, la recombinaison des porteurs pourrait être plus sévère dans les QD alliés. Cependant, en raison du taux de transfert différent des électrons et des trous, davantage de porteurs pourraient être transférés en dehors des QD qui dominent les valeurs de densité de courant.

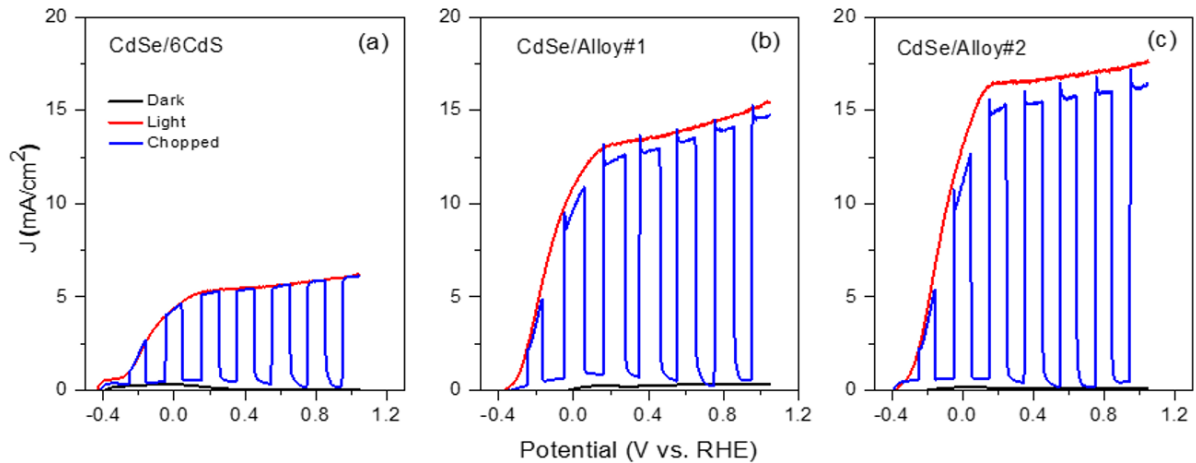


Figure R5 Dépendance photocourant densité-potential de TiO₂ sensibilisé par (a) CdSe/6CdS QDs; (b) QD CdSe/Alloy#1; (c) CdSe/Alloy#2 QDs dans l'obscurité (courbe noire), sous éclairage continu (courbe rouge) et haché (courbe bleue).

Les performances du PEC sont illustrées à la figure R5(a)-(c). Une densité de photocourant saturée de 6.2 mA/cm² est obtenue dans un système de photoanode à base de CdSe/6CdS QD sous un éclairage solaire. Le dispositif PEC basé sur les QD CdSe/Alloy#1 montre une densité de photocourant saturée améliorée d'environ 15.1 mA/cm² qui est 2.4 fois supérieure à celle du dispositif PEC basé sur les QD CdSe/6CdS. De plus, les QD CdSe/Alloy#2 avec les coques en alliage à gradient présentent une densité de photocourant jusqu'à 17.5 mA/cm², ce qui est 2.8 fois plus élevé que celui du dispositif PEC basé sur les QD CdSe/6CdS. Ici, notre cellule PEC avec photoanode basée sur des QD alliés présente une densité de photocourant de 17.5 mA/cm² sous un éclairage solaire. La densité de courant plus élevée peut être attribuée à plusieurs effets synergiques: (i) avec l'ajout de Se élémentaire dans les QD alliés, la plage d'absorption est étendue vers des longueurs d'onde plus longues, ce qui à son tour améliore le transfert efficace des photons aux excitons. (ii) Bénéficiant de la structure de bande de gradient du TiO₂/coquille/cœur, un grand nombre d'électrons et de trous peuvent être extraits des QD dans TiO₂, contribuant ainsi à la densité de courant. En raison du transfert efficace des trous, l'accumulation et l'oxydation des trous ont été largement supprimées. (iii) Selon l'analyse de la dynamique de charge, la séparation spatiale des électrons et des trous augmente, limitant les possibilités de recombinaison.

CdSe/CdS/ZnS core/multiplex shell pour génération PEC H₂

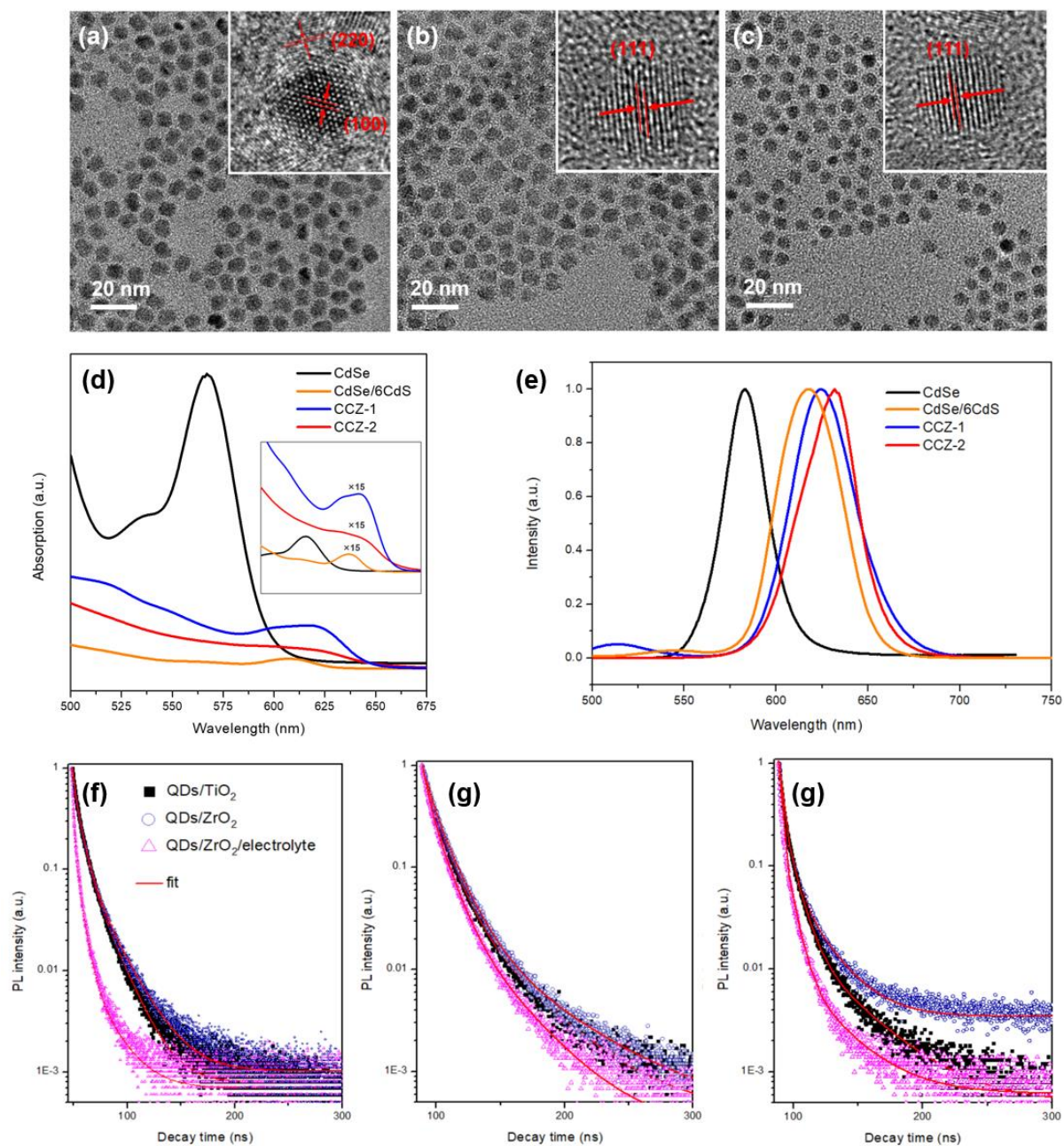


Figure R6 Images MET de (a) CdSe/6CdS QDs, (b) CCZ-1 QDs et (c) CCZ-2 QDs où les encarts du coin droit montraient les images HR-MET des QDs correspondants; Images MET de (a) CdSe/6CdS QDs, (b) CCZ-1 QDs et (c) CCZ-2 QDs où les encarts du coin droit montraient les images HR-TEM des QDs correspondants; (e) Spectre PL des QD CdSe, CdSe/6CdS, CCZ-1 et CCZ-2; (f)-(g) Spectres PL des QD CdSe/6CdS, CCZ-1 et CCZ-2 après dépôt dans des films de TiO₂, des films de ZrO₂ et des films de ZrO₂ en présence d'un électrolyte.

La figure R6(a)-(c) montre les images MET des QD CdSe / 6CdS, CCZ-1 QD et CCZ-2 QD, respectivement. La taille moyenne de CdSe/6CdS est de 7.35 ± 0.7 nm tandis que les tailles moyennes des QD CCZ-1 et CCZ-2 sont respectivement de 7.31 ± 0.8 nm et 6.48 ± 0.8 nm. En raison des mêmes cycles SRSCD développés pour les QD CdSe/6CdS et CCZ-1, la taille des deux types de QD est similaire. La taille de CCZ-2 QDS est plus petite que celle des QD CCZ-1 et CdSe/6CdS, ce qui pourrait être principalement dû au processus d'échange de cations qui s'est produit pendant la croissance des coquilles alliées CdSe_xS_{1-x} et Cd_yZn_{1-y}S, entraînant un rétrécissement de la taille du noyau CdSe. Dans les encarts de la figure R6(a)-(c), les images HR-MET indiquent le plan cristallin (100) ($d = 3.74$ Å) de la structure wurtzite (WZ) de CdSe et le plan (220) ($d = 2.06$ Å) de BZ CdS pour les QD CdSe/6CdS. La limite entre le noyau CdSe et la coque CdS a été clairement observée. Pour les QD CCZ-1 et CCZ-2, les images HR-MET révèlent que l'espacement du réseau de 3.36 Å, ce qui correspond au plan (111) de la structure cristalline BZ de CdS.

Les QD tels que synthétisés ont été étudiés par spectroscopie d'absorption et PL. Comme le montre la figure R6(d), le pic d'absorption du premier excitonique est situé à 607 nm pour les QD CdSe/6CdS. Pour les QD cœur-coquille/coquille, le pic d'absorption du premier excitonique est situé respectivement à 616 nm pour les QD CCZ-1 et à 618 nm pour les QD CCZ-2. De même, le spectre PL montre également le même décalage vers le rouge attribué à la croissance épitaxiale réussie des coques CdS et ZnS (ou couches alliées) [Figure R6(e)]. En règle générale, la durée de vie des QDs-TiO₂ et QDs-ZrO₂ des QD CCZ-1 est de 14.34 ns et 15.21 ns, toutes deux supérieures à celle des QD CdSe/6CdS. Ce résultat indique que les coquilles ZnS servent de barrière de transfert de porteurs où les électrons et les trous sont confinés dans les régions du noyau CdSe et de la coquille CdS. Et les K_{et} et K_{ht} calculés sont tous les deux diminués par rapport à celui des QD CdSe/6CdS qui vérifient l'effet de confinement apporté par les coquilles ZnS. Pour les QD CCZ-2 alliés, le K_{et} est 9 fois supérieur à celui des QD CCZ-1 tandis que la valeur K_{ht} est 9.3 fois supérieure à celle des QD CCZ-1. Ce phénomène indique que l'alignement des bandes a été optimisé par les couches alliées intermédiaires qui ont construit une structure de bande favorable pour que les porteurs se séparent et se transfèrent, entraînant moins de recombinaison de charge.

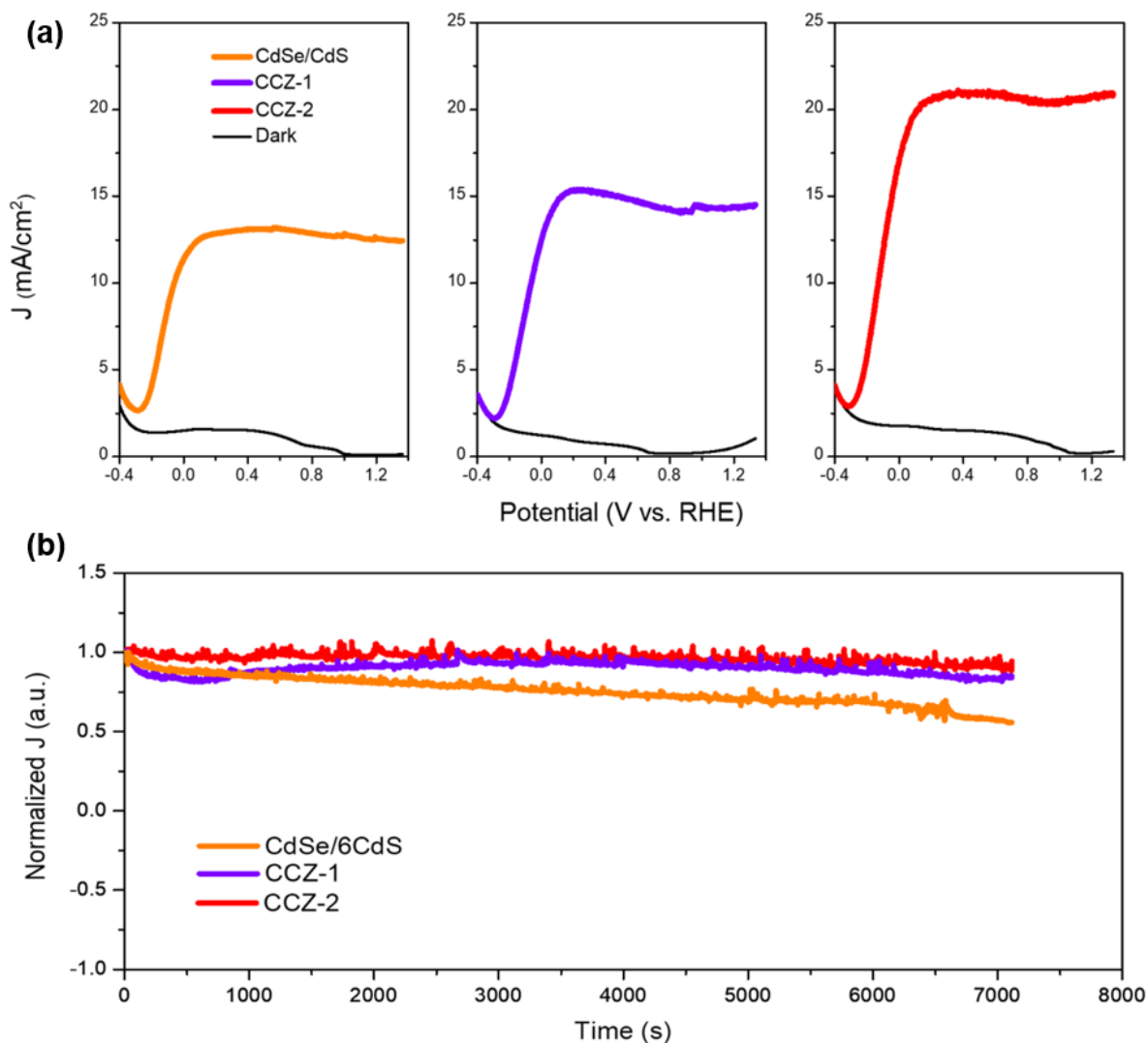


Figure R7 (a) Dépendance entre la densité et le potentiel du photocourant de TiO₂ sensibilisé avec des QD CdSe/6CdS, des QD CCZ-1 et des QD CCZ-2 dans l'obscurité (courbe noire) et sous un éclairage continu (courbe chromatique); (b) Mesures de stabilité (densité de photocourant en fonction du temps) des photoanodes à base de CdSe/6CdS QD, CCZ-1 QD et CCZ-2 QD à 0.6 V vs RHE avec revêtement 2 ZnS.

La figure R7(a) montre la dépendance entre la densité et le potentiel de photocourant de TiO₂ sensibilisé avec des QD CdSe/6CdS CCZ-1 QD et CCZ-2 QD dans l'obscurité et sous un éclairage continu. La photoanode à base de CdSe/6CdS affiche une densité de photocourant saturé de 12.6 mA/cm². Pour les QD CCZ-1, la photoanode peut atteindre la densité de photocourant saturé de 14.2 mA/cm². L'augmentation de la densité de photocourant par rapport

à la photoanode à base de CdSe/6CdS est principalement due à l'amélioration de l'absorption ainsi qu'à l'effet de passivation de surface fourni par les coques en ZnS. En conséquence, les pièges de surface sont largement supprimés et moins de recombinaisons non radiatives se sont produites à la surface des QD. De plus, la densité de photocourant de la photoanode basée sur les QD CCZ-2 alliés atteint 20.5 mA/cm^2 , ce qui est une amélioration considérable par rapport aux deux autres types de QD. Grâce aux coques alliées, la barrière énergétique entre les différents matériaux semi-conducteurs (CdSe, CdS et ZnS) est considérablement réduite, ce qui conduit à un transfert de porteurs plus efficace. Dans le même temps, les coquilles alliées ont également l'effet de passivation que les défauts de surface peuvent être supprimé en conséquence.

La stabilité à long terme est un autre facteur critique pour l'application de l'évolution du PEC H_2 . En règle générale, la stabilité a été étudiée sous une illumination continue d'un soleil à 0.6 V vs RHE. La figure R7(b) montre que la densité de photocourant pour les QD CdSe/6CdS, les QD CdSe/4CdS/2ZnS et les QD CdSe/ $(\text{CdSe}_x\text{S}_{1-x})_3/\text{CdS}/\text{Cd}_y\text{Zn}_{1-y}\text{S}/\text{ZnS}$ sous un éclairage solaire continu pendant 2 heures. Selon la figure R7(d), environ 55 % de la valeur de densité de photocourant initiale a été maintenue pour la photoanode à base de CdSe/6CdS QD. Pour deux types de QD à noyau/coque multiple, environ 84% de la valeur de densité de photocourant initiale a été observée pour la photoanode à base de QD CCZ-1 après 2 heures d'éclairage, tandis qu'une performance de stabilité sans précédent a été obtenue pour la photoanode à base de QD CCZ-2 alliés, avec rétention d'environ 93.4 % de la valeur initiale du photocourant après un éclairage continu de 2 heures. Les performances de stabilité exceptionnelles sont principalement dues au fait que les couches intermédiaires alliées agissent comme des voies rapides pour le transfert des porteurs. En conclusion, l'accumulation de trous est largement réduite dans la bande de valence, conduisant à moins de photo-oxydation des photoanodes. De plus, le ZnS (ou les couches alliées) joue également un rôle important de passivation de la surface des QD. Ainsi, la recombinaison provoquée par les pièges et les défauts de surface peut être considérablement supprimée.